Ab Initio MODELLING OF QUASI-ONE-DIMENSIONAL BOSE GAS EXPERIMENTS VIA THE STOCHASTIC GROSS-PITAEVSKII EQUATION

DONATELLO GALLUCCI

Thesis submitted for the degree of
Doctor of Philosophy

School of Mathematics & Statistics
Newcastle University
Newcastle upon Tyne
United Kingdom

February 2013

To Nonno Ciccio

Acknowledgements

First of all, I would like to thank my supervisor, Nick Proukakis, for his constant help, availability for questions, and careful supervision throughout my entire PhD. I am grateful to Stuart Cockburn for his partial co-supervision and collaboration, and also general support and advice. I want to thank Carlo Barenghi for useful discussions (thanks to these I did not forget my italian), and Mariella Loffredo and Emilio D'Emilio, as without them I would have not started this project. I want to extend my gratitude to Isabelle Bouchoule, Aaldert van Amerongen, Klaasjan van Druten for providing their experimental data for use in our comparisons; moreover I want to acknowledge the group of Alain Aspect (in particular Jocelyn Retter for providing their experimental data), Mathilde Hugbart, Fabrice Gerbier, Joseph Thywissen and Mike Garrett for discussions. Further to this I would like to thank EPSRC for funding this project.

Within the school, I would like to thank all my PhD colleagues, as each of them has helped to make my PhD an enjoyable experience. In particular I want to say a big thank you to Tim Yeomans, Joy Allen, Fred Gent, Anisah Mohamed, Stuart Cockburn and Nathan Barker, with whom I shared the best moments.

Outside of university I would like to say a huge thank you to my parents, for being my best and special friends, and to Marianna, for her endless patience and love.

Abstract

In this thesis we use the stochastic Gross-Pitaevskii equation (SGPE), a finite temperature model for weakly interacting ultracold Bose gases which fully incorporates density and phase fluctuations, to demonstrate *ab initio* quantitative agreement with a number of quasi-one-dimensional experiments. To achieve this, we propose and numerically solve a quasi-one-dimensional form of the SGPE, supported by a self-consistent treatment of radially-excited thermal modes.

The quasi-one-dimensional stochastic Gross-Pitaevskii equation provides an accurate finite temperature description of the dynamical equilibrium of the low-energy axial modes of a Bose gas, assumed to be highly populated and thus treated within the 'classical field' approximation. This treatment allows to self-consistently account for transverse, quasi-one-dimensional effects, which makes it a valid model in the regime where the chemical potential, μ, is approximately equal to a few times the transverse excitation energy, $\hbar\omega_\perp$. In the regime where the thermal energy, k_BT, is also comparable to or larger than $\hbar\omega_\perp$, the transverse excited states play an increasingly important role, and are treated here as one-dimensional independent Bose gases at static equilibrium.

Firstly, we demonstrate that this is an excellent model for *ab initio* investigation of equilibrium properties, such as density profiles and density fluctuations. This is shown by accurately reproducing the *in situ* density profiles recently obtained in the experiments of Trebbia *et al.* [Phys. Rev. Lett. **97**, 250403 (2006)] and van Amerongen *et al.* [Phys. Rev. Lett. **100**, 090402 (2008)], and the density fluctuation data reported by Armijo *et al.* [Phys. Rev. Lett. **105**, 230402 (2010)].

Moreover, we perform an *ab initio* analysis of the temperature dependence of the phase coherence of finite temperature, quasi-one-dimensional Bose gases measured in the experiments of Richard *et al*. [Phys. Rev. Lett. **91**, 010405 (2003)] and Hugbart *et al.* [Eur. Phys. J. D **35**, 155 (2005)]. We find very good agreement across the entire observed temperature range in both experiments, and improve upon previous theoretical modelling of the latter.

Contents

Part I

Introduction

Part I of this thesis is divided in two chapters entitled 'Ultracold quantum Bose gases' and 'Theoretical background'.

In the first chapter we discuss the essential theoretical and experimental background to the study of Bose-Einstein condensation in both uniform and trapped Bose gases. We then turn to a description of the low-dimensional counterpart, highlighting the main differences with respect to the three-dimensional case. We mainly focus on systems whose dynamics is effectively one-dimensional, characterizing the interesting physics that emerges in such systems. Finally we offer a broad comparative introduction to the results presented in this thesis, also highlighting the parameter regime of the various experiments modelled in Part III in an appropriate graph and table.

In the second chapter we outline some of the theoretical approaches for modeling weakly interacting Bose gases. Firstly we discuss the lowest order mean-field description, the Gross-Pitaevskii equation, strictly valid at $T=0$ *K. We then turn to a description of finite-temperature mean-field models, in the static case: while the Hartree-Fock and Hartree-Fock-Bogoliubov theories are symmetry-breaking approaches, the alternative modified Popov theory additionally explicitly includes fluctuations in the phase. For the dynamical case, we review the important aspects of the Zaremba-Nikuni-Griffin (ZNG) approach, describing the coupled dynamics of the condensate and the thermal cloud; we then introduce the number-conserving method, where the violation of atom number conservation, due to a broken-symmetry procedure, is carefully handled. Finally we conclude this review of the theoretical methods with a very broad discussion of classical field (c-field) methods, focussing on a particular implementation, the so-called Stochastic Projected Gross-Pitaevskii equation (SPGPE), given its close analogy to the theory used in this thesis, which is in turn discussed in Part II.*

Chapter 1

Ultracold quantum Bose gases

The theoretical prediction of Bose-Einstein condensation (BEC) dates back to 1924, when an Indian scientist, named Satyendra Nath Bose, derived through statistical arguments the formula of black-body radiation (previously obtained by Planck in a heuristic manner), by treating the photons as a gas of identical particles. The scientific community was initially sceptical and did not accept these results. However, Albert Einstein recognised the value of Bose's work and not only helped him to publish it [1], but he also applied the same arguments to a gas of non-interacting, massive particles [2]. The outcome of this work was the Bose-Einstein statistics:

$$f(\epsilon_i) = \frac{1}{e^{(\epsilon_i - \mu)/k_\mathrm{B}T} - 1}, \tag{1.1}$$

where $f(\epsilon_i)$ determines the statistical distribution of non-interacting bosons over the energy states ϵ_i at temperature T, k_B is the Boltzmann constant and μ is the chemical potential of the system.

The interesting aspect about Bose-Einstein statistics is that Eq. (1.1) predicts at low enough temperatures a macroscopic occupation of the lowest quantum energy level, leading to the formation of a Bose-Einstein condensate.

1.1 Bose-Einstein condensation

Let us consider a three-dimensional (3D) gas of non-interacting massive particles: there are two relevant length scales in such a system which are the mean interparticle distance and the thermal wavelength of each particle.

- The mean interparticle distance is the average distance between the particles in the gas and is given by $n^{-1/3}$, where n is the number density for a 3D system.

- The thermal wavelength, λ_{T}, associated to every particle, is the de Broglie wavelength at a specific temperature T. Loosely speaking λ_{T} represents the uncertainty in the position of the particle, and is conventionally defined by:

  $$\lambda_{\mathrm{T}} = \sqrt{\frac{2\pi\hbar^2}{mk_BT}}, \tag{1.2}$$

  where m is the mass of the particle and $\hbar = h/2\pi$ is the reduced Planck's constant.

As we can see, λ_{T} is inversely proportional to the square root of T; depending on the value of the temperature and consequently on the relative size of the two length scales mentioned above, we can distinguish two regimes:

- At high temperatures, such that the thermal de Broglie wavelength is much smaller than the mean interparticle distance (i.e. $\lambda_{\mathrm{T}} \ll n^{-1/3}$), the classical, particle-like behaviour dominates and one can potentially follow the trajectory of each individual particle.
- At low temperatures, the quantum mechanical behavior of the particles comes into play when the particle wavelength becomes comparable with, or smaller than the average distance between the particles (i.e. $\lambda_{\mathrm{T}} \lesssim n^{-1/3}$). In this so-called quantum degenerate regime, the indistinguishability of particles becomes important and the notion of a particle trajectory no longer makes sense.

Quantum mechanics accounts for the wave-like properties of the particles, and classifies them into two distinct categories: fermions and bosons. This classification is based on the value of the spin of the particles and consequently on their statistics. Fermions have a half integer value of spin, and are characterised by Fermi-Dirac statistics, while bosons have an integer value of spin and are governed by Bose-Einstein statistics. Fermions follow the Pauli exclusion principle, which precludes any pair of fermions to occupy the same quantum state simultaneously. Conversely, Bose-Einstein statistics allows any number of bosons to be in the same energy level, and this is the essence of BEC.

At high temperatures, the effects of quantum statistics can be neglected, and the distinction between fermions and bosons is not relevant: the mean occupation number in each quantum energy level is in fact much less than one, and the particles behave according to the classical Boltzmann distribution. However, when the temperature is lowered to a critical value (which depends on the thermodynamic parameters of the system), the wavelengths become comparable to the interatomic distance, and begin to overlap. When this occurs, the particles become indistinguishable (roughly speaking they lose their 'identity'), and exhibit a wave-like behaviour. In a bosonic gas this leads to the onset of a macroscopic occupation of a single quantum state, i.e. a number of particles, N_0, shares the same (lowest) energy level with decreasing temperature, with $N_0 \to N$ (the total particle number in the system) in the limit $T \to 0\,\mathrm{K}$. We should emphasise that this process (BEC), can also occur in an *ideal* bosonic gas: it is not caused by interparticle interactions, but it is only a consequence of the specific quantum statistics (i.e. the Bose-Einstein distribution) governing the particles. The BEC is a phenomenon occurring in momentum space, when a finite fraction of the particles occupy the zero momentum state ($\mathbf{p} = 0$). The criterion for the onset of BEC in a 3D non-interacting uniform system, can be cast into the following form:

$$n\lambda_{\mathrm{T}}^3 \geq \zeta(3/2). \tag{1.3}$$

In the above equation $\zeta(3/2) \approx 2.612$ is the Riemann zeta function, calculated at the value $3/2$. The parameter $n\lambda_{\mathrm{T}}^3$ is called the *phase-space density*, and gives the number of particles contained in a volume equal to the cube of the thermal de Broglie wavelength. Related to the above condition, one can derive the corresponding critical temperature, T_{c}, for a homogeneous gas, at which the Bose-Einstein phase transition occurs:

$$T_{\mathrm{c}} = \frac{2\pi\hbar^2}{mk_{\mathrm{B}}}\left(\frac{n}{\zeta(3/2)}\right)^{2/3}. \tag{1.4}$$

This is the highest temperature at which a finite fraction of the particles exists in the zero momentum state ($\mathbf{p} = 0$): for temperature higher than the critical one, there is no energy state macroscopically occupied. The occupancy of the lowest energy level, for a 3D uniform system, can then be cast as a function of temperature via the expression:

$$\frac{N_0}{N} = 1 - \left(\frac{T}{T_{\mathrm{c}}}\right)^{3/2}. \tag{1.5}$$

In typical experiments with ultracold bosonic gases, the system is instead confined in a trap, which to a good approximation can be considered harmonic:

$$V(\mathbf{r}) = \frac{1}{2}m(\omega_x^2 x^2 + \omega_y^2 y^2 + \omega_z^2 z^2), \tag{1.6}$$

where $\omega_{\{x,y,z\}}$ are the harmonic oscillator frequencies in the x, y, z direction respectively. The confinement makes the system non-uniform, and the critical temperature, as well as the condensate occupancy have different expressions. For an ideal harmonically trapped 3D Bose gas, the critical temperature is given by:

$$T_\mathrm{c} = \frac{\hbar\bar{\omega}}{k_\mathrm{B}}\left(\frac{N}{\zeta(3)}\right) \approx 0.94\hbar\bar{\omega}N^{1/3}, \tag{1.7}$$

where $\bar{\omega} = (\omega_x\omega_y\omega_z)^{1/3}$ is the geometric mean of the oscillator frequencies.

The condensate occupancy for an ideal harmonically trapped 3D Bose gas is characterised by the following expression:

$$\frac{N_0}{N} = 1 - \left(\frac{T}{T_\mathrm{c}}\right)^3. \tag{1.8}$$

Typical values for the critical temperature in a bosonic atomic gas are of the order of $10^{-6}\ K$: at such temperatures the thermodynamical stable phase would be the solid state [3]. However, in order to observe Bose-Einstein condensation, it is necessary to maintain the system in the gaseous phase. This is achieved by making the gas extremely dilute: densities of the order of $10^{13} - 10^{15}\ \mathrm{cm}^{-3}$ are required to prevent the formation of clusters (e.g. 3-body recombination) on the time-scale of the experiment. For comparison, density of air at room temperature is $\sim 10^{19}\ \mathrm{cm}^{-3}$. In typical experiments the above conditions can be maintained for a short time only (i.e. up to few minutes).

In these dilute systems, the atoms are on average far from each other, As a result we are only interested in the long-range effect of the interatomic potential, and the exact details of it at short distances are unimportant. Moreover the rate of two-body recombination is much higher than the three-body recombination, i.e. the probability that three or more particles interact simultaneously is very low. The very low temperatures associated with such systems guarantee that the high energy scattering channels (i.e. d-wave etc...) can be typically discarded in the description of interactions: scattering only occurs via the s-wave channel (corresponding to the angular momentum $l = 0$). According to standard scattering theory, the interactions in such conditions can be described by a single parameter, the binary s-wave scattering length, here denoted by a_s. The value of the scattering length depends on the internal structure of the particular atomic species; moreover, its sign determines whether the interactions are attractive (-)

or repulsive (+). The condition of diluteness in a 3D system can then be cast as:

$$a_{\mathrm{s}} \ll n^{-1/3}. \tag{1.9}$$

This condition also implies that the gas is weakly-interacting, which however does not mean that interactions do not have a significant effect.

1.2 Experimental realisation

In the decade following the publications by Bose and Einstein, there was large scepticism on the validity of the prediction for BEC. However in 1938, Fritz London suggested that the phenomenon of superfluidity in ^{4}He was intimately related with Bose-Einstein condensation [4]. The superfluidity of ^{4}He had been discovered by Kapitza [5], Allen and Misener [6]: it was found that at the critical temperature $T_{\mathrm{c}} = 2.17\,\mathrm{K}$, the liquid ^{4}He undergoes a phase transition to a superfluid state characterised by the absence of viscosity. It was actually suggested, that superfluid ^{4}He was the first experimental realisation of Bose-Einstein condensation, although interactions in this system are very strong, and the system is a liquid rather than a gas. In fact, Einstein first predicted the formation of BEC for a non-interacting gas; in superfluid ^{4}He however, the condensed fraction (i.e. occupancy of the lowest energy state) is reduced by the strong interactions, and approximately 10% of the system is condensed. In the following years this led to the quest for a weakly-interacting gas, for which interparticle collisions are so rare, that the system would remain in the gaseous phase even at very low temperatures. For such systems, the condensed fraction would be much higher than in superfluid ^{4}He, and therefore more easily observed.

In 1959, Hecht suggested [7] that spin-polarised hydrogen could be the ideal candidate for the first experimental realisation of BEC, since the characteristic interactions were estimated to be weak, even at very low temperatures. This idea was later confirmed by Stwalley and Nosanow in 1976 [8], stimulating numerous experiments (e.g. by Silvera and Walraven [9]) to cool down spin-polarised hydrogen. Such experiments came quite close to the required degeneracy early on, but the final step proved rather challenging. Following such work, several other experiments were initiated with the more heavy alkali gases, for which it was estimated that their three-body recombination rate would be lower than in spin-polarised hydrogen. In 1995 BEC was first realised in a dilute vapour of rubidium (^{87}Rb) by the group of E. A. Cornell and C. E. Wieman at NIST [10], and subsequently in sodium (^{23}Na) by the group of W. Ketterle at the Massachusetts Institute of Technology (MIT) [11]: for this achievement, they were jointly awarded the Nobel prize in 2001. This was soon followed by litium (^{7}Li) in the group of R. G. Hulet [12, 13], with the experimental realisation of BEC in spin-polarised hydrogen realised a few years later in 1998 by the group of T. J. Greytak and D. Kleppner at MIT [14].

The early pioneering work on spin-polarised hydrogen resulted in major advances in experimental techniques which are currently used in the experiments with ultracold quantum gases. The experimental route to the realisation of BEC in a weakly-interacting gas consists of different cooling stages, largely based on the powerful methods of laser cooling developed since the 1970s, alongside magnetic trapping. A brief description of this procedure follows. Initially a beam of atoms at a temperature of the order of hundreds of Kelvin is cooled down by a so-called Zeeman slower, i.e. a laser propagating in the opposite direction of the atomic beam which reduces the temperature by around two orders of magnitude. The effect produced by the counter-propagating laser is to exert a radiative force on the atoms due to the absorption of photons; since the subsequent photon emission is randomly directed, on average the net effect is a transfer of momentum in the direction opposite to the beam. To take into account the Doppler effect, the frequency of the laser has to be lower than the atomic resonance; however, to compensate for the fact that the velocity of the atoms is gradually reducing, the frequency has to be increased in time accordingly.

At temperatures as low as $T \sim 1\,\mathrm{K}$, the vapour can be loaded into a magneto-optical trap (MOT), that combines the use of laser cooling and magnetic trapping. A typical scheme for a MOT is as follows: a pair of counter-propagating lasers is arranged in each perpendicular direction, creating a so-called optical molasses, in which the atoms are subjected to a viscous-like force; in addition, a magnetic gradient is applied, such that it is zero at the centre of the trap and increases towards the edges. Each of the six counter-propagating lasers is ‘red’ detuned (i.e. the frequency is smaller than the atomic resonance) to account for the Doppler effect; in this way the probability of absorbing a photon in the direction opposite to the propagation of the atomic beam will always be greater than the one of absorbing a photon in the same direction. The magnetic field confines the atoms in a very small region (typically $\sim \mu\mathrm{m}$), by exploiting the interaction energy between the field and the magnetic moment of the atoms. The use of alkali atoms is very convenient for magnetic trapping, since their orbital configuration contains one unpaired electron in the outer shell which makes their magnetic moment relatively big. In a MOT, there is a lower limit (called Doppler limit) on the attainable temperature, which is of the order of $\sim m\mathrm{K}$; this occurs when the cooling rate balances the heating rate due to absorption and random emission of photons within the atomic vapour. However, temperatures below the Doppler limit can be realised via a process called Sisyphus cooling: this exploits the degeneracy nature of the energetic levels in an alkali atom, as well as the fact that the radiation field created by counterpropagating lasers is inhomogeneous. Roughly speaking the atoms tend to move up the potential 'hill' created by the lasers, and by doing so they lose kinetic energy; this process is repeated several times, by continuously optically pumping the atoms into a state where they are at the bottom of the potential. The so-called *recoil limit* characteristic of this technique corresponds to temperatures several orders of magnitude smaller than the Doppler limit, and is given by the kinetic energy that an atom acquires by absorbing a photon.

The temperature ($\sim \mu$K) and phase-space density ($\sim 10^{-5}$) attained through the use of a MOT are still not enough to reach the conditions for BEC, for which the phase space density should be of order 1. Therefore, a final cooling stage is typically applied, known as *evaporative cooling*: roughly speaking this consists of the selective removal of the high energy atoms from the trap, so that the remaining atoms rethermalise at a lower temperature (provided elastic collisions dominate). This is done by using a radio frequency pulse which flips the spin of high energy atoms so that they enter high-field seeking states, and are expelled from the trap. This process must be performed slowly enough in order not to lose too many atoms; in fact, there must remain a sufficient number of atoms in the trap, to reach the density necessary for BEC to occur. This process is applied until temperatures of the order of nano-Kelvin are reached; in general, BEC occurs at temperatures of $< 10^{-6}$ K, and densities of $\sim 10^{13}\ \mathrm{cm}^{-3}$. In addition to $^{87}\mathrm{Rb}$ [10], $^{23}\mathrm{Na}$ [11] and $^{7}\mathrm{Li}$ [12, 13], several atomic species have been shown to undergo Bose-Einstein condensation, such as $^{85}\mathrm{Rb}$ [15], $^{41}\mathrm{K}$ [16], $^{4}\mathrm{He}$ [17], $^{174}\mathrm{Yb}$ [18], $^{133}\mathrm{Cs}$ [19], $^{52}\mathrm{Cr}$ [20], $^{84}\mathrm{Sr}$ [21, 22], $^{86}\mathrm{Sr}$ [23], $^{88}\mathrm{Sr}$ [24], $^{40}\mathrm{Ca}$ [25], $^{164}\mathrm{Dy}$ [26].

1.3 Low-dimensional geometry

In the previous sections we have seen that an ideal uniform bosonic gas undergoes a phase transition at a specific critical temperature, whereby a large fraction of the atoms condense in the lowest energy state. This was explicitly discussed for a three-dimensional Bose gas; the situation changes drastically for two- and one-dimensional systems. For a homogeneous system in two dimensions, the phenomenon of BEC only occurs at $T = 0\,\mathrm{K}$ (i.e. there is no macroscopic occupation at non-zero temperature), while for a one-dimensional weakly-interacting system, BEC does not take place at any temperature. This is because long-wavelength excitations are more pronounced in lower dimensions, and tend to destroy the coherence in the system: this is essentially the content of the Mermin-Wagner-Hohenberg theorem [27, 28], which states that no spontaneous symmetry breaking occurs for finite temperature systems in dimensions smaller or equal than two. However the theorem is strictly valid in the thermodynamic limit, i.e. $N \to \infty$, $V \to \infty$, and $N/V \to constant$, where V is the volume of the gas.

In a low-dimensional inhomogeneous (e.g. harmonically trapped) weakly interacting Bose gas instead, a condensate can exist provided the external trapping sufficiently restricts the size of the system [29–32]. A magneto-optical trap can be modelled, to a good approximation, with a harmonic potential of the form of Eq. (1.1). The ability to manipulate the frequencies of the harmonic potential offers the possibility to change the spatial extent of the system in each direction separately, thus rendering it anisotropic, and consequently new interesting physics emerges. The dimensionality in fact plays a crucial role in such systems in determining the properties of these gases.

In three-dimensional harmonic traps, as discussed before, the system undergoes a phase transition[1] which leads to the appearance of coherence across the entire sample, as experimentally demonstrated in [34–37]. By setting the trap frequency in one direction much larger than the others, the effective dynamics of the system is reduced to two dimensions [38–41], with many interesting phenomena occurring, such as the Berezinskii-Kosterlitz-Thouless transition [42–49]. Increasing the trap frequency in a further direction allows to realise highly elongated traps, where the interesting physics occurs in the axial direction, and the system is effectively one-dimensional (1D) [31, 32, 38, 50–80].

In a 1D set-up, one may obtain [31] either a weakly-interacting system, or, for rather low densities[2], a strongly-interacting Tonks-Girardeau gas [55–57, 81]. The interactions can be parametrised by the Lieb-Liniger coupling constant (essentially giving the ratio of interaction energy to kinetic energy [82]), which in one

---

[1] Strictly speaking a phase transition only occurs in the thermodynamical limit, which for a 3D harmonic trap is defined as $N \to \infty$, $\omega \to 0$, and $N\omega^3 \to \mathrm{constant}$ [33].

[2] such that $nl_{\mathrm{cor}} \ll 1$, where $1/n$ is the interparticle distance and $l_{\mathrm{cor}} = \hbar/\sqrt{mg_{1\mathrm{d}}n}$ is the correlation length [31].

dimension takes the form [31, 83]:

$$\gamma_{\text{int}} = \frac{mg_{1\text{d}}}{\hbar^2 n}, \tag{1.10}$$

where n is the density of the gas in 1D. We notice that the strongly interacting regime, $\gamma_{\text{int}} \gg 1$, occurs, rather counterintuitively, for low densities. In this thesis however, we deal with weakly-interacting Bose gases, characterised by the condition[3] $\gamma_{\text{int}} \ll 1$ (typical values of γ_{int} evaluated at the trap centre are $\gamma_{\text{int}} \sim (10^{-5} - 10^{-2})$, see Table 1.1 for more details).

Provided $a_{\text{s}} \ll l_{\perp}$, where $l_{\perp} = \sqrt{\hbar/m\omega_{\perp}}$ is the radial harmonic oscillator length, the scattering, parametrised by a_{s}, is still considered three-dimensional, and the effective interaction coupling constant $g_{1\text{d}}$ reduces to [84, 85]:

$$g_{1\text{d}} = \frac{2\hbar^2 a_s}{ml_{\perp}^2}. \tag{1.11}$$

The above interaction parameter can also be derived by integrating the 3D effective interaction, $g_{3\text{d}} = 4\pi\hbar^2 a_{\text{s}}/m$, over the radial density profile which is assumed to be Gaussian. The finite temperature phase diagram of a *weakly interacting* 1D Bose gas [31, 62, 86] is more complex than that of a 3D gas, due to a separation in the temperatures for the onset of density and phase fluctuations. Density fluctuations are typically suppressed at higher temperatures than phase fluctuations, allowing for the formation of a so-called quasi-condensate [87]. In such systems, two characteristic temperatures become relevant, associated with the onset of phase (T_ϕ) and density (T_{d}) fluctuations [31].

The degeneracy temperature, T_{d}, for a harmonically confined interacting gas in 1D, takes the form [31]:

$$T_{\text{d}} = \frac{N\hbar\omega_z}{k_{\text{B}}}. \tag{1.12}$$

For $T > T_{\text{d}}$ we have a classical gas where density fluctuations are pronounced (as will become apparent from Eq. (1.13), phase fluctuations are also pronounced in this regime).

For temperatures $T_\phi < T < T_{\text{d}}$ instead, density fluctuations are relatively suppressed with respect to phase fluctuations and the system reduces to a condensate with fluctuating phase known as a quasi-condensate [87]. In 1D, T_ϕ is given by

---

[3] Notice that for a inhomogeneous Bose gas $\gamma_{\text{int}} \equiv \gamma_{\text{int}}(z)$, i.e. it varies with the position z in the trap.

the expression[4] [31]:

$$T_\phi = \frac{N(\hbar\omega_z)^2}{k_\mathrm{B}\mu}. \tag{1.13}$$

Loosely speaking, T_ϕ corresponds to the temperature where the off-diagonal one-body density matrix (first-order correlation function) $g^{(1)}(z, z')$, decays to zero at the edge of the quasi-condensate [32, 86, 88].

Thus, for $T < T_\phi$, and clearly $T_\phi \ll T_\mathrm{d}$ in relevant systems, both density and phase fluctuations are suppressed and the gas becomes in some sense a 'true' condensate [31]. Notice that the expression of Eq. (1.13) for T_ϕ will be revisited and further analysed in Chapters 5 and 6, to closely follow related definitions used in the experiments where phase fluctuations are investigated (see also Appendix B).

In practice T_d is a rather high temperature, and in order to determine where the crossover to quasi-condensation occurs it is more convenient to use another characteristic temperature, which we here denote as T_qc [89]:

$$T_\mathrm{qc} = \frac{\hbar\omega_z}{k_\mathrm{B}}\frac{N}{\ln(2N)}. \tag{1.14}$$

In the work by Ketterle and van Druten [89] it was found that, at such temperature, a macroscopic ground state occupation occurs for a trapped 1D ideal gas. The dependence of the crossover temperature T_qc on the interactions was also studied in the work by Al Khawaja *et al.* [90], in which it was found that T_qc increases with interactions.

1.3.1 Weakly-interacting quasi-one-dimensional Bose gases

The pure one-dimensional limit discussed in the previous section is characterised by the condition that both the chemical potential of the gas μ, and the thermal energy $k_\mathrm{B}T$, are much smaller than the transverse excitation energy $\hbar\omega_\perp$ (while still focusing here on the limit of a weakly-interacting gas in the sense of $\gamma_\mathrm{int} \ll 1$). This means that the transverse motion is reduced to a zero-point oscillation, as the energy is not sufficient to populate the excited transverse modes of the gas. Although experiments can nowadays be engineered to produce gases which are both weakly interacting and practically 1D [55, 59–61, 63, 65, 68, 72, 91, 92], the early experiments performed did not satisfy these conditions so well, and the system was instead in the 1D-3D crossover regime [32, 51–54, 58, 64, 93–95], henceforth referred to in this thesis as 'quasi-1D'.

---

[4] Corresponding expression for highly elongated 3D systems [32] is given in Appendix B.

In such quasi-1D systems, characterised by $\mu, k_{\mathrm{B}}T \sim \hbar\omega_{\perp}$, low-energy thermal excitations of the axial modes play a crucial role, as they tend to destroy the coherence in the sample [31, 64, 86–88, 90, 96–102]. Such excitations may have wavelengths greater than the transverse extent of the system, therefore acquiring a one-dimensional (1D) character [51–54, 58–61, 63–65, 68, 72, 91, 93–95].

Given the central role played by fluctuations in a finite temperature quasi-1D Bose gas, it is crucial to include these effects in order to give an accurate theoretical description of the entire weakly-interacting regime.

1.3.2 Early experiments

A number of experiments have probed the physics of highly-elongated finite temperature weakly-interacting Bose gases at equilibrium. In 2001 Görlitz *et al.* [38] realised BECs of sodium atoms ^{23}Na, which were brought to transition from the 3D Thomas-Fermi regime (see Section 2.1.1) into the 2D and 1D regime, by reducing the number of atoms in the system, through interaction with a thermal beam. In a separate experiment, Greiner *et al.* [103] created 1D Bose gases of ^{87}Rb stored in thousands of individual tubes formed with a 2D optical lattice; the phase coherence properties of this quantum system were also studied by releasing the atoms and observing the interference pattern.

Fluctuations of the phase in highly elongated BECs were first experimentally observed in 2001, in the experiment by Dettmer *et al.* [51]; it was found that after the ballistic expansion, phase fluctuations, expected to exist in the trapped system, transformed into density ripples. A different technique was used by Hellweg *et al.* [53], who investigated the phase correlation properties by measuring the spatial correlation function of very elongated 3D ^{87}Rb BEC. This was achieved by observation of the interference pattern generated by two displaced copies of the initial condensate (see also Ref. [58]). The physics of these systems has also been studied by means of Bragg spectroscopy, for the purpose of investigating the momentum distribution; in Richard *et al.* [54] it was found that phase fluctuations lead to a broadening of the momentum distribution. While in the fully coherent case, the momentum distribution tends to a Gaussian-like behaviour [104], in the phase-fluctuating regime this tends to a Lorentzian-like shape [64]. In 2005, Hugbart *et al.* [95] used a similar technique to the one adopted in the earlier work by Hellweg *et al.* [53], to probe highly elongated 3D BECs, in a regime of lower T/T_{ϕ} such that the effect of phase fluctuations is somewhat reduced compared to the earlier experiment by Richard *et al.* [54]. Notice that the experiments by Richard *et al.* [54] and Hugbart *et al.* [95] (in the group of A. Aspect) are investigated in

Part III of this thesis. Further experiments have also analysed the coherence properties of nonequilibrium BECs, by means of a condensate-focusing technique (see Shvarchuck *et al.* [52]).

Direct observation of density fluctuations was performed in 2006 in the experiment by Estève *et al.* [63], via *in situ* meaurements of highly elongated Bose gases confined in atom chips; subsequently in 2010, Armijo *et al.* [61] carried out a similar experiment, and density fluctuations were found to saturate in the presence of a quasi-condensate — see Section 3.7.1. First realised in 2001 [76, 77], atom chips are microfabricated circuits, particularly suitable for realising highly confining potentials to achieve one-dimensional systems [80]. The technology of atom chips was also used to realise atom interferometers, as achieved in the experiment by Schumm *et al.* [68], and to perform *in situ* measurements of density profiles of 1D Bose gases at the crossover between the classical and quasi-condensate regimes [59, 60].

An accurate analysis of the coherence properties in such systems is then necessary for potential applications, such as matter-wave interferometry [66–68, 70–74, 105, 106], atom chips [69, 75–80] and atom lasers [35, 107–110].

1.4 Thesis overview

This thesis is divided into three main parts, consisting of a generic introduction to theories for modeling ultracold Bose gases (Part I), a detailed description (Part II) of the model used to reproduce the results from experiments, and a direct *ab initio* comparison to five independent experiments (Part III).

Part I - Introduction

In Chapter 2, we provide an essential theoretical background for modeling Bose gases, starting from a review of the zero-temperature Gross-Pitaevskii model. We then describe the main aspects of finite-temperature approaches, where the non-condensed part, i.e. the thermal cloud, is treated statically (Hartree-Fock approach, modified Popov theory [97]) and dynamically (Zaremba-Nikuni-Griffin theory [111]). Further finite-temperature approaches are discussed, namely the number-conserving method [112–114], and classical field (c-field) techniques [115], focusing on the so-called stochastic Projected Gross-Pitaevskii equation.

Part II - A Self-Consistent Quasi-1D Stochastic model

In Chapter 3, we introduce the Stochastic Gross-Pitaevskii equation (SGPE) [116, 117], which is a Langevin equation that takes the form of a dissipative nonlinear Schrödinger equation in the presence of dynamical noise added so as to mimick the effect of fluctuations.

We then describe our extended quasi-one-dimensional form of the SGPE [118, 119], which is suitable to describe the axial modes of a weakly interacting Bose gas, in a regime where the main dynamics occur along one dimension, but transverse effects also need to be accounted for. The quasi-1D SGPE is here supported by a static treatment of the transverse excited modes, which are treated as independent Bose gases at equilibrium, and the numerical scheme for solving these is discussed.

Part III - Quantitative *Ab Initio* Comparison to Quasi-1D Experiments

In this part of the thesis we demonstrate that our model is an excellent tool for *ab initio* studies of quasi-one-dimensional weakly-interacting Bose gases. The parameter regimes of the five experiments investigated in this part are shown in Figure 1.1 and in Table 1.1.

Chapter 4 deals with the regime $\mu < \hbar\omega_\perp$. Here we show that this model accurately reproduces *in situ* densities (hollow symbols in Fig. 1.1) and density fluctuations (filled red squares in Fig. 1.1) in atom chip experiments of the groups of I. Bouchoule [59, 61] and N. J. van Druten [60].

- The experiment by Trebbia *et al.* [59] (in the group of I. Bouchoule) investigated the physics of a quasi-one-dimensional weakly-interacting Bose gas in harmonic trap. Density profiles were measured *in situ*, at four values of the temperature, and it was observed that the gas enters the quasi-condensate regime. The theoretical analysis used in [59] was based on a 3D Hartree-Fock approach, which failed to predict the existence of a quasi-condensate in the center of the atomic cloud.

  We demonstrate that the model described in Part II provides excellent prediction of the experimental results at all temperatures, thereby improving on previous theoretical analysis [59].

- The experiment by van Amerongen *et al.* [60] (in the group of N. J. van Druten) also dealt with quasi-one-dimensional weakly-interacting Bose gases, in harmonic trap. The system, realised on an atom chip, was investigated at the crossover between the classical and the quasi-condensate regimes and spatial density profiles were measured *in situ*. The analytical model used in [60] to interprete the experimental results was based on the Yang-Yang thermodynamics, and provided very good agreement.

We further probe the model explained in Part II, undertaking a comparison with the experimental density profiles of [60], finding excellent agreement across the entire temperature regime. This test indirectly provides an insight on the matching between the predictions of the model explained in Part II and those from the Yang-Yang model; this agreement is further demonstrated by showing that the values of the numerical chemical potential in the SGPE are identical to those from the Yang-Yang model.

- The experiment by Armijo *et al.* [61] (in the group of I. Bouchoule) investigated the density fluctuations in a quasi-one-dimensional weakly-interacting Bose gas, confined on atom chip. The second- and third-order correlation functions were evaluated at the crossover between the ideal gas and the quasi-condensate regimes. Density fluctuations were measured by investigating the shot-to-shot variations of atom number in several independent experimental realisations; it was found that density fluctuations saturate in the presence of a quasi-condensate at low enough temperature. The analytical interpretation, based on a modified Yang-Yang model [61], recovered the experimental results in the ideal gas regime, but predicted too great a reduction of the density fluctuations in the lowest temperature case investigated.

  The quasi-1D SGPE model (Part II) gives instead excellent agreement with both second- and third-order experimental correlation functions at all temperatures. The numerical predictions are shown to provide a smooth crossover between the two regimes investigated, in perfect agreement with the corresponding mean-field results (ideal gas, quasi-condensate), only valid in the appropriate limits.

The work presented in this chapter has been previously published as:
Quantitative study of quasi-one-dimensional Bose gas experiments via the stochastic Gross-Pitaveskii equation
S. P. Cockburn, D. Gallucci and N. P. Proukakis,
Phys. Rev. A, **84**, 023613 (2011).
This work was undertaken jointly with Stuart Cockburn — who was leading the simulations — and its aim was to address the question of the optimum model for

analysing the experiments which form the key aspect of this thesis.

In the regime $\mu \sim \text{few}\,\hbar\omega_{\perp}$, we also demonstrate excellent reconstruction of two earlier quasi-one-dimensional phase fluctuation experiments in the group of A. Aspect [54, 95] (respectively denoted by stars and triangles in Fig. 1.1).

- Chapter 5 deals with the experiment by Richard *et al.* [54], who investigated the phase coherence properties of a 3D elongated weakly-interacting Bose gas confined in harmonic trap. In order to do so Richard *et al.* [54] measured the axial momentum distribution by means of Bragg spectroscopy, and extracted the coherence length from the measure of the half-width at half-maximum of the momentum profile. The regime of relatively 'strong' phase fluctuation, $6 < T/T_{\phi} < 28$, was analysed and the coherence length was found to be smaller than the quasi-condensate extent.

  By using the quasi-1D SGPE model (Part III) we investigate the temperature dependence of the phase coherence length; in particular we undertake a point-by-point analysis, and find excellent agreement with the experimental values of the coherence length (scaled to the size of the system), reported here as a function T/T_{ϕ}.

- Chapter 6 deals with the experiment by Hugbart *et al.* [95], who investigated the regime of relatively 'weak' phase fluctuations $0.8 < T/T_{\phi} < 8$. The spatial correlation function of a 3D elongated weakly-interacting Bose gas was investigated by means of an interferometric technique and the coherence length was finally extracted. The temperature dependence of the scaled coherence length was then investigated. The model used in [95] to reproduce the experimental results provided with predictions in line with the experimental trend, but were affected by a systematic shift.

  We further compare the quasi-1D SGPE model (Part II) with these experimental predictions, and find instead very good agreement across the temperature range investigated. Our findings however span a slightly smaller range of T/T_{ϕ}, an issue that we also address here. This is partially resolved by extracting the values of T/T_{ϕ} with an alternative method, based on the analysis of the distributions of the phase in our numerical simulations.

The work presented in these chapters has been previously published as:
Phase coherence in quasicondensate experiments: An ab initio analysis via the stochastic Gross-Pitaevskii equation
D. Gallucci, S. P. Cockburn and N. P. Proukakis,

Phys. Rev. A, **86**, 013627 (2012).

In order to identify the parameter regime of the five experiments discussed in Part III of this thesis, we report in Figure 1.1 the value of the thermal energy $k_\mathrm{B}T$, against the numerical chemical potential μ, (each scaled to the transverse excitation energy $\hbar\omega_\perp$), for all the data considered in the experiments. The vertical solid line separates the thermal ($\mu < 0$) and quasi-condensate ($\mu > 0$) regimes. The vertical dashed line instead divides the experiments for which $\mu < \hbar\omega_\perp$ (Trebbia *et al.* [59] (hollow, black circles), van Amerongen *et al.* [60] (hollow, blue diamonds) and Armijo *et al.* [61] (filled, red squares) from those for which $\mu \sim \text{few}\,\hbar\omega_\perp$ (i.e. Richard *et al.* [54] (brown stars) and Hugbart *et al.* [95] (filled, violet triangles)). The horizontal dashed line is only a guide to separate the data for which the transverse excited modes are not significantly populated ($k_\mathrm{B}T < \hbar\omega_\perp$) from those for which these states are also thermally populated ($k_\mathrm{B}T > \hbar\omega_\perp$).

In Table 1.1 we report approximate characteristic temperatures and interaction parameters as extracted from our theoretical analysis, presented in this thesis.

Experiment	T/T_ϕ	T/T_d	T/T_qc	$\gamma_\mathrm{int}(0)$	$g_\mathrm{1d}[\hbar\omega_z l_\mathrm{z}]$
Trebbia *et al.* [59]	$45 - 83$	~ 0.04	~ 0.4	$\sim 10^{-3}$	0.65
van Amerongen *et al.* [60]	$26 - 100$	$0.08 - 0.09$	$0.76 - 0.83$	$\sim 10^{-2}$	1.05
Armijo *et al.* [61]	$35 - 100$	$0.05 - 0.06$	$0.5 - 0.7$	$\sim 10^{-2}$	1.25
Richard *et al.* [54]	6 – 28	$\sim 10^{-3}$	~ 0.07	$\sim 10^{-4}$	0.32
Hugbart *et al.* [95]	0.8 – 8	$\sim 10^{-3}$	$\sim 10^{-2}$	$\sim 10^{-4}$	0.13; 0.24

Table 1.1: Approximate values (or ranges) of the reduced temperatures T/T_ϕ, T/T_d, T/T_qc and interaction parameters γ_int, g_1d, for the experimental data considered [54, 59–61, 95] (based on the theoretical analysis presented in this thesis).

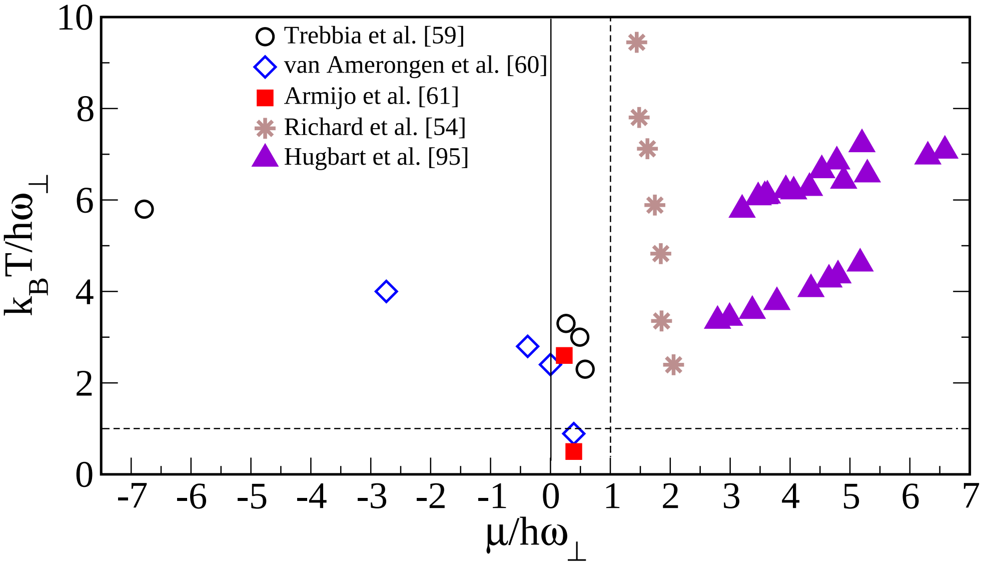

Figure 1.1: Phase diagram showing the regimes of all experimental data considered in this thesis (based on the theoretical analysis discussed in Chapter 3). Hollow symbols indicate density profiles data of Trebbia *et al.* [59] (circles) and van Amerongen *et al.* [60] (diamonds), whereas filled symbols indicate the density fluctuation data of Armijo *et al.* [61] (squares), and the phase fluctuation data of Richard *et al.* [54] (stars) and Hugbart *et al.* [95] (triangles).

Chapter 2

Theoretical background

A dilute interacting Bose gas confined in an external potential can be described by the following Hamiltonian [120]:

$$\hat{H} = \int d\mathbf{r}\, \hat{\Psi}^{\dagger}(\mathbf{r},t)\hat{h}_0(\mathbf{r})\hat{\Psi}(\mathbf{r},t) + \frac{1}{2}\int\int d\mathbf{r}d\mathbf{r}'\, \hat{\Psi}^{\dagger}(\mathbf{r},t)\hat{\Psi}^{\dagger}(\mathbf{r}',t)V(\mathbf{r}-\mathbf{r}')\hat{\Psi}(\mathbf{r}',t)\hat{\Psi}(\mathbf{r},t). \tag{2.1}$$

This is written in the occupation number representation (second quantised form), in terms of Bose field operator $\hat{\Psi}^{\dagger}(\mathbf{r},t)$ ($\hat{\Psi}(\mathbf{r},t)$)[1], which respectively creates (annihilates) a particle at position $\mathbf{r}$ and time t [122]. The single particle operator $\hat{h}_0(\mathbf{r})$ is defined by $\hat{h}_0(\mathbf{r}) = -\hbar^2\nabla^2/2m + V^{\mathrm{ext}}(\mathbf{r},t)$, where $V^{\mathrm{ext}}(\mathbf{r},t)$ is the external potential confining the system. The use of the exact two-body interatomic potential $V(\mathbf{r}-\mathbf{r}')$ is valid under the assumption that the gas is extremely dilute ($|a_{\mathrm{s}}| \ll n^{-1/3}$), as the probability that three- (or many-) body collisions occur is very low [123]. The factor $1/2$ avoids double counting of the interaction between pairs of particles.

For dilute, weakly-interacting Bose gases at very low temperature, the exact two-body potential $V(\mathbf{r}-\mathbf{r}')$ can be replaced by a contact interaction of the form [120]:

$$V(\mathbf{r}-\mathbf{r}') = g_{3\mathrm{d}}\delta(\mathbf{r}-\mathbf{r}'), \tag{2.2}$$

where $g_{3\mathrm{d}} = 4\pi\hbar^2 a_{\mathrm{s}}/m$ is the effective interaction strength. Under this approximation the Hamiltonian of Eq. (2.1) takes the form :

---

[1] $\hat{\Psi}^{\dagger}(\mathbf{r},t) = \sum_i \hat{a}_i^{\dagger}(t)\varphi_i^{*}(\mathbf{r},t)$ $\left(\hat{\Psi}(\mathbf{r},t) = \sum_i \hat{a}_i(t)\varphi_i(\mathbf{r},t)\right)$, where $\hat{a}_i^{\dagger}$ and $\hat{a}_i$ are the single-particle creation and annhilation operators [121] , and $\varphi_i(\mathbf{r},t)$ are single-particle wavefunctions.

$$\hat{H} = \int d\mathbf{r}\, \hat{\Psi}^\dagger(\mathbf{r},t)\hat{h}_0(\mathbf{r})\hat{\Psi}(\mathbf{r},t) + \frac{g_{3\mathrm{d}}}{2}\int d\mathbf{r}\, \hat{\Psi}^\dagger(\mathbf{r},t)\hat{\Psi}^\dagger(\mathbf{r},t)\hat{\Psi}(\mathbf{r},t)\hat{\Psi}(\mathbf{r},t). \tag{2.3}$$

In order to study the dynamics of the system, one can solve the equation of motion for the Bose field operator, which can be cast in the 'Heisenberg' picture [2] as follows:

$$i\hbar\frac{d\hat{\Psi}(\mathbf{r},t)}{dt} = [\hat{\Psi}(\mathbf{r},t), \hat{H}], \tag{2.4}$$

where $[\cdots]$ indicates the commutator. In order to work out an expression for the commutator in Eq. (2.4), it is useful to recall the commutation relations for the bosonic field operators:

$$[\hat{\Psi}(\mathbf{r},t), \hat{\Psi}^\dagger(\mathbf{r}',t)] = \delta(\mathbf{r}-\mathbf{r}'), \qquad [\hat{\Psi}(\mathbf{r},t), \hat{\Psi}(\mathbf{r}',t)] = [\hat{\Psi}^\dagger(\mathbf{r},t), \hat{\Psi}^\dagger(\mathbf{r}',t)] = 0. \tag{2.5}$$

The commutator in Eq. (2.4) can be expanded as (we drop the time dependence for compactness):

$$\begin{aligned}
&[\hat{\Psi}(\mathbf{r}), \hat{H}] = \\
&= \hat{\Psi}(\mathbf{r})\Big(\int d\mathbf{r}'\ \hat{\Psi}^\dagger(\mathbf{r}')\hat{h}_0(\mathbf{r}')\hat{\Psi}(\mathbf{r}')\Big) - \Big(\int d\mathbf{r}'\ \hat{\Psi}^\dagger(\mathbf{r}')\hat{h}_0(\mathbf{r}')\hat{\Psi}(\mathbf{r}')\Big)\hat{\Psi}(\mathbf{r}) + \\
&\frac{g_{3\mathrm{d}}}{2}\Big[\hat{\Psi}(\mathbf{r})\Big(\int d\mathbf{r}'\ \hat{\Psi}^\dagger(\mathbf{r}')\hat{\Psi}^\dagger(\mathbf{r}')\hat{\Psi}(\mathbf{r}')\hat{\Psi}(\mathbf{r}')\Big) - \Big(\int d\mathbf{r}'\ \hat{\Psi}^\dagger(\mathbf{r}')\hat{\Psi}^\dagger(\mathbf{r}')\hat{\Psi}(\mathbf{r}')\hat{\Psi}(\mathbf{r}')\Big)\hat{\Psi}(\mathbf{r})\Big] \\
&= \int d\mathbf{r}'\ \hat{\Psi}(\mathbf{r})\hat{\Psi}^\dagger(\mathbf{r}')\hat{h}_0(\mathbf{r}')\hat{\Psi}(\mathbf{r}') - \int d\mathbf{r}\ \hat{\Psi}^\dagger(\mathbf{r}')\hat{\Psi}(\mathbf{r})\hat{h}_0(\mathbf{r}')\hat{\Psi}(\mathbf{r}') + \\
&\frac{g_{3\mathrm{d}}}{2}\Big[\int d\mathbf{r}'\ \hat{\Psi}(\mathbf{r})\hat{\Psi}^\dagger(\mathbf{r}')\hat{\Psi}^\dagger(\mathbf{r}')\hat{\Psi}(\mathbf{r}')\hat{\Psi}(\mathbf{r}') - \int d\mathbf{r}'\ \hat{\Psi}^\dagger(\mathbf{r}')\hat{\Psi}^\dagger(\mathbf{r}')\hat{\Psi}(\mathbf{r})\hat{\Psi}(\mathbf{r}')\hat{\Psi}(\mathbf{r}')\Big] \\
&= \int d\mathbf{r}'\ [\hat{\Psi}(\mathbf{r}), \hat{\Psi}^\dagger(\mathbf{r}')]\hat{h}_0(\mathbf{r}')\hat{\Psi}(\mathbf{r}') + \frac{g_{3\mathrm{d}}}{2}\int d\mathbf{r}'\ [\hat{\Psi}(\mathbf{r}), \hat{\Psi}^\dagger(\mathbf{r}')\hat{\Psi}^\dagger(\mathbf{r}')]\hat{\Psi}(\mathbf{r}')\hat{\Psi}(\mathbf{r}').
\end{aligned} \tag{2.6}$$

By exploiting the commutation relations of Eq. (2.5) and the standard properties of commutators, the equation of motion for the Bose field operator becomes:

$$i\hbar\frac{d\hat{\Psi}(\mathbf{r},t)}{dt} = \hat{h}_0\hat{\Psi}(\mathbf{r},t) + g_{3\mathrm{d}}\hat{\Psi}^\dagger(\mathbf{r},t)\hat{\Psi}(\mathbf{r},t)\hat{\Psi}(\mathbf{r},t). \tag{2.7}$$

Bose condensed systems at very low temperature are typically characterised

---

[2] In this picture all the time-dependence is incorporated in the operators, whereas the state vectors are time-independent.

by the presence of a *condensate* surrounded by a *thermal cloud*; the former corresponds to the macroscopic occupation of the single (lowest) quantum state, whereas the latter refers to the particles lying in the excited quantum states above the condensate. Such a description can be mathematically reflected with a split of the bosonic field operator into two contributions as follows [124]:

$$\hat{\Psi}(\mathbf{r},t) = \hat{\phi}(\mathbf{r},t) + \hat{\delta}(\mathbf{r},t). \tag{2.8}$$

Here the condensate is contained into the operator $\hat{\phi}(\mathbf{r},t) = \hat{a}_0(t)\varphi_0(\mathbf{r},t)$, while the operator $\hat{\delta}(\mathbf{r},t) = \sum_{i\neq 0} \hat{a}_i(t)\varphi_i(\mathbf{r},t)$ accounts for both thermal and quantum fluctuations. In the limit of a large number, N_0, of condensed atoms (i.e. $N_0 \simeq N$), where N is the total atom number in the system, one can perform the so-called Bogoliubov replacement [125] through which $\hat{a}_0 \simeq \sqrt{N_0}$. The condensate contribution can therefore be treated as a classical field, and all the operator dependence is contained into the fluctuation operator:

$$\hat{\Psi}(\mathbf{r},t) = \phi(\mathbf{r},t) + \hat{\delta}(\mathbf{r},t), \tag{2.9}$$

with $\phi(\mathbf{r},t) = \sqrt{N_0}\varphi_0(\mathbf{r},t)$ often named the 'condensate wavefunction'. Performing the above approximation implies fixing the phase of the condensate, technically known as a symmetry-breaking procedure, which leads to the violation of particle number conservation [120]. In fact, since $N_0 \gg 1$, it is assumed that the addition or removal of one particle in the condensate does not affect the system, which implies that the states $|N\rangle$, $|N-1\rangle$ and $|N+1\rangle$ are physically equivalent [126].

A direct consequence is that the ensemble average of the bosonic field operator is equivalent to the condensate wavefunction, that is $\langle\hat{\Psi}(\mathbf{r},t)\rangle = \phi(\mathbf{r},t) \neq 0$, which means that the average is a well defined value [120]. In this case the symbol $\langle\cdots\rangle$ indicates the average between two states, where the left one contains one atom less than the right one [126].

At this stage one can substitute the approximation of Eq. (2.9) into the Heisenberg equation (Eq. (2.7)), and then take the mean-field value of this equation; this leads to an equation of motion containing products of two or three operators $\hat{\delta}$. Several levels of approximation arise then, depending on the order retained in the equation of motion; in the next section we discuss the lowest-order mean-field theory, corresponding to a zero-temperature treatment.

2.1 T = 0: Gross-Pitaevskii equation (GPE)

In the limit of very low temperature ($T = 0$), and to the lowest order of approximation, practically all the atoms are in the condensate ($N = N_0$); one can therefore neglect the operator for thermal and quantum fluctuations (i.e. $\hat{\delta} = 0$), and simply replace the bosonic field operator $\hat{\Psi}(\mathbf{r}, t)$ with the classical wavefunction $\phi(\mathbf{r}, t)$. The Heisenberg equation then takes the form of a nonlinear Schrödinger equation, known as the Gross-Pitaevskii equation [126, 127]:

$$i\hbar \frac{\partial \phi(\mathbf{r}, t)}{\partial t} = [\hat{h}_0(\mathbf{r}, t) + g_{3\mathrm{d}} |\phi(\mathbf{r}, t)|^2] \phi(\mathbf{r}, t). \tag{2.10}$$

This equation represents the lowest order mean-field approximation, and it is formally valid only at $T = 0$; however it describes very well a wide range of phenomena of BECs up to $T \approx T_\mathrm{c}/2$. The nonlinear character of the equation is given by the presence of the mean-field term, $g_{3\mathrm{d}}|\phi|^2$, which describes the interactions among the particles in the condensate.

The GPE (Eq. (2.10)) has both static and dynamical solutions. In order to seek for the stationary solution, characterising the ground state, one can eliminate the time via the replacement:

$$\phi(\mathbf{r}, t) = \phi_0(\mathbf{r}) e^{-i\mu t/\hbar} \tag{2.11}$$

and this yields the time-independent GPE [120]

$$\mu \phi_0(\mathbf{r}) = \left[-\frac{\hbar^2}{2m} \nabla^2 + V^{\mathrm{ext}}(\mathbf{r}) + g_{3\mathrm{d}} |\phi_0(\mathbf{r})|^2 \right] \phi_0(\mathbf{r}). \tag{2.12}$$

Here μ is the chemical potential, representing the energy necessary to add (remove) one particle from the condensate (i.e. $\mu = E(N) - E(N-1) \sim \partial E/\partial N$) [126].

2.1.1 Thomas-Fermi approximation

We now consider a typical approximation to the ground state solution of a condensate confined in harmonic trap:

$$V^{\mathrm{ext}}(x, y, z) = \frac{1}{2} m (\omega_x^2 x^2 + \omega_y^2 y^2 + \omega_z^2 z^2), \tag{2.13}$$

where $\omega_{x,y,z}$ is the frequency of the trap in each direction. It can be shown that for sufficiently large clouds and repulsive interactions ($a_\mathrm{s} > 0$), the kinetic term in Eq. (2.12) can be neglected, as it is smaller than the interaction and potential energies [127]. Under this so-called Thomas-Fermi approximation, Eq. (2.12) can be rewritten as:

$$\left[V^{\text{ext}}(\mathbf{r}) + g_{\text{3d}}|\phi_0(\mathbf{r})|^2\right]\phi_0(\mathbf{r}) = \mu\phi_0(\mathbf{r}). \tag{2.14}$$

The approximate density of the ground state is then given by:

$$|\phi_0(\mathbf{r})|^2 = \frac{\mu - V^{\text{ext}}(\mathbf{r})}{g_{\text{3d}}}. \tag{2.15}$$

This takes the form of an inverted parabola in the central region of the trap (within the Thomas-Fermi radius defined as $R^2_{x,y,z} = 2\mu/m\omega^2_{x,y,z}$), and it is defined as long as $\mu \geq V^{\text{ext}}$.

It is interesting to notice that under such an approximation the chemical potential is the same everywhere in the trap, and it is given by the sum of two contributions, i.e. the interaction term and the external potential confining the system [127]:

$$\mu = g_{\text{3d}}|\phi_0(\mathbf{r})|^2 + V^{\text{ext}}(\mathbf{r}). \tag{2.16}$$

2.1.2 Elementary excitations

In order to study the dynamics of the condensate, one can seek small amplitude oscillations. Typically one looks for solutions of the form [120]

$$\phi(\mathbf{r},t) = e^{-i\mu t/\hbar}[\phi_0(\mathbf{r}) + \delta\phi(\mathbf{r},t)], \tag{2.17}$$

where $\delta\phi(\mathbf{r},t)$ represents small excitations on top of the condensate wavefunction. One can then use the above *ansatz* into the time dependent GPE of Eq. (2.10): if $\delta\phi(\mathbf{r},t) \ll \phi_0(\mathbf{r})$, it is possible to linearise the equation, keeping only terms up to the first order in $\delta\phi(\mathbf{r},t)$. By subtracting the time independent GPE of Eq. (2.12) we then obtain:

$$i\hbar\frac{\partial}{\partial t}\delta\phi(\mathbf{r},t) = [\hat{h}_0 + 2g_{\text{3d}}|\phi_0|^2 - \mu]\delta\phi(\mathbf{r},t) + g_{\text{3d}}\phi_0^2\delta\phi^*(\mathbf{r},t). \tag{2.18}$$

One can assume excitations of the form [120]:

$$\delta\phi(\mathbf{r},t) = \sum_i [u_i(\mathbf{r})e^{-i\omega_i t} + v_i^*(\mathbf{r})e^{i\omega_i t}], \tag{2.19}$$

where ω_{i} is the frequency of the oscillation. Inserting the above into Eq. (2.18), and collecting all the terms containing prefactors like $e^{i\omega_i t}$ and $e^{-i\omega_i t}$ yields the following pair of equations, known as the (zero-temperature) Bogoliubov equations (analogous to the Bogoliubov de Gennes equations in superconductivity) [33, 120]:

$$[\hat{h}_0 + 2g_{3\mathrm{d}}|\phi_0(\mathbf{r})|^2 - \mu]u_i(\mathbf{r}) + g_{3\mathrm{d}}[\phi_0(\mathbf{r})]^2 v_i(\mathbf{r}) = \epsilon_i u_i(\mathbf{r}), \tag{2.20}$$

$$[\hat{h}_0 + 2g_{3\mathrm{d}}|\phi_0(\mathbf{r})|^2 - \mu]v_i(\mathbf{r}) + g_{3\mathrm{d}}[\phi_0^*(\mathbf{r})]^2 u_i(\mathbf{r}) = -\epsilon_i v_i(\mathbf{r}). \tag{2.21}$$

These equations describe the collective modes in the system and represent the response of the condensate to excitations at zero temperature, with energies $\epsilon_\mathrm{i} = \hbar\omega_\mathrm{i}$ [127]. These excitations can be considered as dressed particles (or quasi-particles), i.e. particles interacting via the mean-field [120].

For uniform condensates the solutions of the Bogoliubov equations are plane waves, that is $u_i(\mathbf{r}) = u_\mathbf{p} e^{i\mathbf{p}\cdot\mathbf{r}/\hbar}$ and $v_i(\mathbf{r}) = v_\mathbf{p} e^{i\mathbf{p}\cdot\mathbf{r}/\hbar}$; moreover the time independent GPE of Eq. (2.12) reduces to $\mu\phi_0 = (g_{3\mathrm{d}}|\phi_0|^2)\phi_0$. The Bogoliubov equations then become:

$$\left[\frac{|\mathbf{p}|^2}{2m} + g_{3\mathrm{d}}|\phi_0(\mathbf{r})|^2 - \epsilon_i\right]u_\mathbf{p} + g_{3\mathrm{d}}[\phi_0(\mathbf{r})]^2 v_\mathbf{p} = 0, \tag{2.22}$$

$$\left[\frac{|\mathbf{p}|^2}{2m} + g_{3\mathrm{d}}|\phi_0(\mathbf{r})|^2 + \epsilon_i\right]v_\mathbf{p} + g_{3\mathrm{d}}[\phi_0^*(\mathbf{r})]^2 u_\mathbf{p} = 0. \tag{2.23}$$

This system of coupled equations can be solved by imposing that the determinant of the coefficient equals zero, which yields:

$$\hbar\omega_\mathbf{p} = \sqrt{\frac{|\mathbf{p}|^2}{2m}\left[\frac{|\mathbf{p}|^2}{2m} + 2g_{3\mathrm{d}}|\phi_0|^2\right]}. \tag{2.24}$$

The above equation represents the Bogoliubov dispersion relation [125]. For small momenta (large wavelengths) the energy spectrum tends to the phonon dispersion relation $\hbar\omega_\mathbf{p} = \sqrt{g_{3\mathrm{d}}|\phi_0|^2/m}\,|\mathbf{p}|$, whereas in the opposite regime it tends to the free particle spectrum plus a mean- field contribution, $\hbar\omega_\mathbf{p} = |\mathbf{p}|^2/2m + g_{3\mathrm{d}}|\phi_0|^2$.

2.2 T > 0: Static models

The aim of this section is to go beyond the zero-temperature limit, and account for finite temperature effects. This is done by explicitly including the contribution from the fluctuation operator $\hat{\delta}$, within a mean-field treatment, in such a manner which corresponds to the thermal cloud being static.

2.2.1 Generalised mean-field: Phase-coherent condensate

In order to go beyond the zero temperature limit, and account for finite temperature effects, one must retain the non-condensate operator in Eq. (2.9); if we replace the full expression of Eq. (2.9) in the hamiltonian of Eq. (2.3) we can see that we obtain an expression containing products of three and four $\hat{\delta}$. At this stage one can perform a mean-field approximation, which reduces to the full hamiltonian into a quadratic form (which is convenient for performing the diagonalisation). Based on Wick's theorem, which states that at equilibrium an average over multiple operators is equal to the sums of averages of pairwise contracted operators [122], i.e. $\langle\hat{\delta}^\dagger\hat{\delta}^\dagger\hat{\delta}\hat{\delta}\rangle = 2\langle\hat{\delta}^\dagger\hat{\delta}\rangle\langle\hat{\delta}^\dagger\hat{\delta}\rangle + \langle\hat{\delta}\hat{\delta}\rangle\langle\hat{\delta}^\dagger\hat{\delta}^\dagger\rangle$, one may approximate:

$$\hat{\delta}^\dagger\hat{\delta}^\dagger\hat{\delta}\hat{\delta} \simeq 4\langle\hat{\delta}^\dagger\hat{\delta}\rangle\hat{\delta}^\dagger\hat{\delta} + \langle\hat{\delta}^\dagger\hat{\delta}^\dagger\rangle\hat{\delta}\hat{\delta} + \langle\hat{\delta}\hat{\delta}\rangle\hat{\delta}^\dagger\hat{\delta}^\dagger - [2\langle\hat{\delta}^\dagger\hat{\delta}\rangle\langle\hat{\delta}^\dagger\hat{\delta}\rangle + \langle\hat{\delta}\hat{\delta}\rangle\langle\hat{\delta}^\dagger\hat{\delta}^\dagger\rangle] \tag{2.25}$$

and

$$\hat{\delta}^\dagger\hat{\delta}\hat{\delta} \simeq 2\langle\hat{\delta}^\dagger\hat{\delta}\rangle\hat{\delta} + \hat{\delta}^\dagger\langle\hat{\delta}\hat{\delta}\rangle, \qquad \hat{\delta}^\dagger\hat{\delta}^\dagger\hat{\delta} \simeq 2\hat{\delta}^\dagger\langle\hat{\delta}^\dagger\hat{\delta}\rangle + \langle\hat{\delta}^\dagger\hat{\delta}^\dagger\rangle\hat{\delta}. \tag{2.26}$$

It can be shown that the approximation of Eq. (2.25) physically implies that collisions between thermal atoms are neglected. Analogously one can take the average of Eq. (2.26) which leads to $\langle\hat{\delta}^\dagger\hat{\delta}\hat{\delta}\rangle = \langle\hat{\delta}^\dagger\hat{\delta}\hat{\delta}\rangle = 0$, since by construction $\langle\hat{\delta}^{(\dagger)}\rangle = 0$. This approximation is instead equivalent to neglecting collisions that lead to exchange of atoms between condensate and thermal cloud. The only collision processes allowed are therefore those which preserve the number of atoms in the condensate and in the thermal cloud.

The above approximations have reduced both four- and three- points correlations to two-points correlations, allowing only mean-field coupling between the two subcomponents of the systems, i.e. the condensate $n_c(r,t) = |\phi(r,t)|^2$ and the thermal cloud $\tilde{n}(r,t) = \langle\hat{\delta}^\dagger(r,t)\hat{\delta}(r,t)\rangle$. An additional mean-field contribution arises from the approximation in Eqs. (2.25) and (2.26), $\tilde{m}(r,t) = \langle\hat{\delta}(r,t)\hat{\delta}(r,t)\rangle$, which is often referred to as the pair anomalous average, because an unequal number of creation and annihilation operators is averaged over [120]. This term is particularly important when dealing with attractive interactions, while it plays a minor role in repulsive BECs [33, 120].

In the so-called Hartree-Fock limit, one discards all the pair correlations of like non-condensed operators, i.e. the anomalous average and its conjugate. In this picture the generalised form of the time-independent GPE takes the form:

$$[\hat{h}_0 + g_{3\mathrm{d}}|\phi_0|^2 + 2g\tilde{n}_0]\phi_0 = \mu\phi_0.$$

The additional contribution is given by the (static) thermal cloud $\tilde{n}_0$, (a zero subscript denotes a static value), that accounts for collisions between one condensate and one thermal atoms. The system is still described by *single-particle energies*; however these energies are modified by the presence of the condensate mean field and by the thermal atoms, leading to dressed Hartee-Fock energies:

$$\tilde{\epsilon}_i(r) = \epsilon_i + 2g_{3\mathrm{d}}[|\phi_0|^2 + \tilde{n}_0] - \mu.$$

On the other hand, if the anomalous average is taken into account, the limit discussed is called Hartree-Fock-Bogoliubov, and the system is well described in terms of quasiparticles, whose energy is given by the generalised Bogoliubov equations [120]. The generalised GPE in this case takes an additional term [120]:

$$[\hat{h}_0 + g|\phi_0|^2 + 2g_{3\mathrm{d}}\tilde{n}_0]\phi_0 + g_{3\mathrm{d}}\tilde{m}_0\phi_0^* = \mu\phi_0.$$

2.2.2 Modified Popov: Inclusion of phase fluctuations

The methods discussed so far are symmetry-breaking approaches, thus meaning that the phase of the condensate is assigned a definite, yet random, value. In three dimensions, fluctuations in the phase only play a role in a very narrow region around the critical temperature; however, this is not the case for low dimensional Bose gases, where these fluctuations are enhanced and effectively preclude the formation of a condensate. The inclusion of phase fluctuations can be done by replacing the splitting of the Bose field operator of Eq. (2.8), with a more general expression [97]:

$$\hat{\Psi}(\mathbf{r},t) = \sqrt{n_0(\mathbf{r},t)}e^{i\hat{\Theta}(\mathbf{r},t)} + \hat{\psi}'(\mathbf{r},t). \tag{2.27}$$

The operator $\hat{\Theta}(\mathbf{r},t)$ permits to treat phase fluctuations exactly, and allows to evaluate the phase coherence in the system through calculation of first order correlation functions. Moreover density fluctuations are also accounted for via the presence of the operator $\hat{\psi}'(\mathbf{r},t)$. The density of the whole field can then be expressed as:

$$\begin{aligned}\langle\hat{\Psi}^\dagger(\mathbf{r},t)\hat{\Psi}(\mathbf{r},t)\rangle &= n_0(\mathbf{r},t)\langle e^{-i\hat{\Theta}(\mathbf{r},t)}e^{i\hat{\Theta}(\mathbf{r},t)}\rangle + \langle[\hat{\psi}'(\mathbf{r},t)]^\dagger\hat{\psi}'(\mathbf{r},t)\rangle \\ &+ \sqrt{n_0(\mathbf{r},t)}\langle e^{-i\hat{\Theta}(\mathbf{r},t)}\hat{\psi}'(\mathbf{r},t)\rangle + \sqrt{n_0(\mathbf{r},t)}\langle[\hat{\psi}'(\mathbf{r},t)]^\dagger e^{i\hat{\Theta}(\mathbf{r},t)}\rangle,\end{aligned} \tag{2.28}$$

where the first and second term on the right hand side can be identified as $n_0(\mathbf{r},t)$ and $\tilde{n}(\mathbf{r},t)$, while the other terms vanish in the assumption that correlations between condensate phase and non-condensate density can be neglected.

The mean-field methods discussed so far retain correlations of fluctuations about the mean field condensate only up to quadratic order, as we have seen before. Such a procedure is practically equivalent to taking the lowest order expansion in Eq. (2.27) such that $e^{i\hat{\Theta}(\mathbf{r},t)} \simeq 1 + i\hat{\Theta}(\mathbf{r},t)$.

It turns out that this approximation is not accurate enough for describing low dimensional systems, because the total density in Eq. (2.28) would then acquire an extra contribution, $n_0\langle\hat{\theta}(\mathbf{r},t)\hat{\theta}(\mathbf{r},t)\rangle$. This term becomes extremely large for momentum $p \to 0$ in one- and two-dimensional homogeneous systems (except at T=0 for the two dimensional case), leading to a so-called infrared divergence. This has been carefully handled by Andersen *et al.* [97], where they improved on the Popov theory by proposing a model where phase and density fluctuations are treated exactly, and the equations of state are free from any divergences. Practically, this is achieved by subtracting the term $n_0\langle\hat{\theta}(\mathbf{r},t)\hat{\theta}(\mathbf{r},t)\rangle$, that leads to the infrared divergence, from the total density, yielding a system of two coupled equations, that in the homogeneous case takes the form [90]:

$$n = n_0 + \frac{1}{V}\sum_p \left[\frac{\epsilon_p - \hbar\omega_p}{2\hbar\omega_p} + \frac{n_0 g_{3\mathrm{d}}}{2\epsilon_p + 2\mu} + \frac{\epsilon_p}{\hbar\omega_p}N(\hbar\omega_p)\right], \tag{2.29}$$

$$\mu = (2n - n_0)g_{3\mathrm{d}} = (2n' + n_0)g_{3\mathrm{d}}, \tag{2.30}$$

where $n' = n - n_0$ is the depletion in the condensate due to quantum and thermal fluctuations and $N(x) = 1/(e^{\beta x} - 1)$.

The corresponding equations for the trapped case are derived in [97] , and the generalisation of Eq. (2.30) to the trapped case (in the local density approximation) becomes the nonlinear Schrödinger equation:

$$\mu\Upsilon_0(\mathbf{r}) = \left[-\frac{\hbar^2}{2m}\nabla^2 + V^{\mathrm{ext}}(\mathbf{r}) + g_{3\mathrm{d}}(2n'(\mathbf{r}) + |\Upsilon_0(\mathbf{r})|^2)\right]\Upsilon_0(\mathbf{r}), \tag{2.31}$$

where $\Upsilon_0(\mathbf{r}) = \sqrt{n_0}$. However it turns out that to a good approximation one can calculate the densities through the Thomas-Fermi approximation, and solve Eqs. (2.29) and (2.30) locally at each point with a local chemical potential $\mu(\mathbf{r}) = \mu - V^{\mathrm{ext}}(\mathbf{r})$.

This model provides a good description of three-dimensional Bose gas, reproducing the quantum depletion expression (for a condensate) of the original Popov theory [128]; moreover it enables the study of the physics of low dimensional Bose gases, with an exact treatment of phase fluctuations, thereby avoiding the problem of infrared divergency.

2.3 T > 0: Dynamical and stochastic models

The static models discussed in the previous sections describe the Bose condensed system at different levels of approximation; however all of these methods neglect the dynamics of the thermal cloud, by assuming it to be static. At the mean-field level, one can derive the time-dependent generalisation of the Hartree-Fock and Hartree-Fock-Bogoliubov equations where the dynamics of the condensate is now coupled to the evolution of the normal and anomalous averages. To show this, we first write the Heisenberg equation for the condensate mean field, and use the split of Eq. (2.9) to obtain:

$$i\hbar\frac{\partial\phi(\mathbf{r},t)}{\partial t} = \hat{h}_0\phi(\mathbf{r},t) + g_{3\mathrm{d}}\langle\hat{\Psi}^\dagger(\mathbf{r},t)\hat{\Psi}(\mathbf{r},t)\hat{\Psi}(\mathbf{r},t)\rangle, \tag{2.32}$$

where

$$\langle\hat{\Psi}^\dagger(\mathbf{r},t)\hat{\Psi}(\mathbf{r},t)\hat{\Psi}(\mathbf{r},t)\rangle = n_c\phi + 2\tilde{n}\phi + \tilde{m}\phi^* + \langle\hat{\delta}^\dagger\hat{\delta}\hat{\delta}\rangle. \tag{2.33}$$

Note that terms including average of only one non-condensate operator are zero, due to the assumed symmetry-breaking. Analogously, one can derive the corresponding Heisenberg equation for the non-condensate operator:

$$i\hbar\frac{\partial\hat{\delta}(\mathbf{r},t)}{\partial t} = [\hat{\delta}(\mathbf{r},t),\hat{H}] = i\hbar\frac{\partial}{\partial t}(\hat{\Psi}(\mathbf{r},t) - \langle\hat{\Psi}(\mathbf{r},t)\rangle), \tag{2.34}$$

which can be expressed as [111]:

$$\begin{aligned} i\hbar\frac{\partial\hat{\delta}}{\partial t} &= \hat{h}_0\hat{\delta} + g_{3d}[2|\phi|^2\hat{\delta} + \phi^2\hat{\delta}^\dagger] + 2g_{3d}\phi(\hat{\delta}^\dagger\hat{\delta} - \langle\hat{\delta}^\dagger\hat{\delta}\rangle) \\ &\quad + g_{3d}\phi^*(\hat{\delta}\hat{\delta} - \langle\hat{\delta}\hat{\delta}\rangle) + g_{3d}(\hat{\delta}^\dagger\hat{\delta}\hat{\delta} - \langle\hat{\delta}^\dagger\hat{\delta}\hat{\delta}\rangle). \end{aligned} \tag{2.35}$$

By exploiting the above equation, one can then obtain the Heisenberg equations for the normal and anomalous averages:

$$i\hbar\frac{\partial\tilde{n}(\mathbf{r},t)}{\partial t} = \langle[\hat{\delta}^\dagger\hat{\delta},\hat{H}]\rangle, \qquad i\hbar\frac{\partial\tilde{m}(\mathbf{r},t)}{\partial t} = \langle[\hat{\delta}\hat{\delta},\hat{H}]\rangle. \tag{2.36}$$

At the Hartree-Fock level one discards the contribution from i) the anomalous average $\tilde{m}(\mathbf{r},t)$, which takes into account that collisions do not occur in vacuum, but may involve states already occupied, and ii) the triplet term, $\langle\hat{\delta}^\dagger\hat{\delta}\hat{\delta}\rangle$, responsible for the scattering processes leading to exchange of atoms between condensate and non-condensate part. If instead one considers the Hartree-Fock-Bogoliubov approximation, then the anomalous average is also included.

To also describe the collisional processes occurring within the thermal cloud, and the exchange collisonal processes between condensate and thermal cloud, one has to go beyond the mean-field approximations of Eq. (2.25) and Eq. (2.26) respectively.

2.3.1 Zaremba-Nikuni-Griffin (ZNG) kinetic model

In this section we describe the main aspects of the so-called 'ZNG' approach, named after the authors Zaremba, Nikuni and Griffin [111]. This method follows the lines of the early pioneering work by Kirkpatrick and Dorfman [129–131], and by Eckern [132].

The 'ZNG' method is a self-consistent treatment that describes the coupled dynamics of the mean-field condensate, via a dissipative Gross-Pitaevskii-like equation, and the thermal cloud, through a quantum Boltzmann equation.

In the evolution of the condensate, the anomalous averages are assumed to be zero; however a large part of their contribution is accounted for by implicitly retaining the triplet term, $\langle\hat{\delta}^{\dagger}\hat{\delta}\hat{\delta}\rangle$, into the theory. The equation for the evolution of the condensate then takes the form of a GPE at the Hartree-Fock level of approximation, with an additional dissipative term:

$$i\hbar\frac{\partial\phi(\mathbf{r},t)}{\partial t} = [\hat{h}_0 + g_{3\mathrm{d}}(|\phi(\mathbf{r},t)|^2 + 2\tilde{n}(\mathbf{r},t)) - iR(\mathbf{r},t)]\phi(\mathbf{r},t). \tag{2.37}$$

The term iR is directly linked to the triplet term as shown in the following equation:

$$\begin{aligned} R(\mathbf{r},t) =& -ig_{3\mathrm{d}}\frac{\langle\hat{\delta}^{\dagger}\hat{\delta}\hat{\delta}\rangle(\mathbf{r},t)}{\phi(\mathbf{r},t)} \\ &= 2\pi g_{3d}^2\int\frac{d\mathbf{p}_2}{(2\pi\hbar)^3}\int\frac{d\mathbf{p}_3}{(2\pi\hbar)^3}\int\frac{d\mathbf{p}_4}{(2\pi\hbar)^3}\times(2\pi\hbar)^3\delta(m\mathbf{v}_{\mathrm{c}}+\mathbf{p}_2-\mathbf{p}_3-\mathbf{p}_4) \\ &\times\delta(\boldsymbol{\epsilon}_c+\boldsymbol{\epsilon}_2-\boldsymbol{\epsilon}_3-\boldsymbol{\epsilon}_4)\times[f_2(f_3+1)(f_4+1)-(f_2+1)f_3f_4]. \end{aligned} \tag{2.38}$$

The energies ϵ_i are evaluated semi-classically, whereby one assumes that the relevant quantities, such as densities, vary slowly on the length scale of the trapping potential [120, 127]. In the Hartree-Fock limit these energies are single-particle energies dressed by the condensate and non-condensate mean-field potentials:

$$\epsilon_i(\mathbf{r},t) = \frac{|\mathbf{p}_i|^2}{2m} + U(\mathbf{r},t), \tag{2.39}$$

where $U(\mathbf{r}, t) = V^{\text{ext}}(\mathbf{r}_i, t) + 2g_{3\text{d}}[|\phi(\mathbf{r}_i, t)|^2 + \tilde{n}(\mathbf{r}_i, t)]$ is the generalised mean field potential.

The functions f_i in Eq. (2.38) are phase space distribution functions representing the thermal cloud, whose density is defined as:

$$\tilde{n}(\mathbf{r}, t) = \int \frac{d\mathbf{p}}{(2\pi\hbar^3)} f(\mathbf{p}, \mathbf{r}, t). \tag{2.40}$$

In Eq. (2.38) these functions represent the statistical factor for which a particle can be created ($f_i + 1$) or destroyed (f_i) in the state i. The dissipative term iR therefore leads to a transfer of atoms between the two subsystems (i.e. condensate and thermal cloud); however at equilibrium, this term becomes zero (on average), and we are left with a generalised GPE, at the Hartree-Fock level of approximation.

We have introduced the single particle distribution function, describing the thermal cloud in phase space; it is now desirable to also have an expression for the evolution of this distribution, in order to obtain a closed set of equations. The formulation of Zaremba, Nikuni and Griffin [111] is based on a Boltzmann-like equation [133] for the dynamics of the thermal cloud:

$$\frac{df(\mathbf{p}, \mathbf{r}, t)}{dt} = C[f]. \tag{2.41}$$

We first focus on the left hand-side of the above equation: the total derivative for a gas subjected to a slowly varying potential $U(\mathbf{r}, t)$ is [133]:

$$\frac{df(\mathbf{p}, \mathbf{r}, t)}{dt} = \frac{\partial f(\mathbf{p}, \mathbf{r}, t)}{\partial t} + \frac{\mathbf{p}}{m} \cdot \nabla f(\mathbf{p}, \mathbf{r}, t) - \nabla U(\mathbf{r}) \cdot \frac{\partial f(\mathbf{p}, \mathbf{r}, t)}{\partial \mathbf{p}}, \tag{2.42}$$

where $\mathbf{p}/m = d\mathbf{r}/dt$ and $-\nabla V(\mathbf{r}) = d\mathbf{p}/dt$ is the force exerted on the gas.

The functional $C[f]$, appearing on the right hand-side of Eq. (2.43) is the collisional integral, that represents the rate at which the distribution f changes over time. In absence of collisions, this term would be zero, and the Boltzmann equation would reduce to the Liouville equation $df/dt = 0$. When instead collisions are introduced in the treatment, then the Boltzmann equation becomes [111, 123]:

$$\frac{\partial f(\mathbf{p}, \mathbf{r}, t)}{dt} + \frac{\mathbf{p}}{m} \cdot \nabla f(\mathbf{p}, \mathbf{r}, t) - \nabla U(\mathbf{r}) \cdot \frac{\partial f(\mathbf{p}, \mathbf{r}, t)}{\partial \mathbf{p}} = C_{12}[f] + C_{22}[f]. \tag{2.43}$$

The collisional integral C_{12} describes the transfer of an atom from the thermal cloud into the condensate (and its inverse process):

$$
\begin{aligned}
C_{12}[f] = \frac{4\pi}{\hbar} g_{3d}^2 |\phi|^2 \int \frac{d\mathbf{p}_2}{(2\pi\hbar)^3} \int \frac{d\mathbf{p}_3}{(2\pi\hbar)^3} \int \frac{d\mathbf{p}_4}{(2\pi\hbar)^3} \\
\times (2\pi\hbar)^3 \delta(m\mathbf{v}_c + \mathbf{p}_2 - \mathbf{p}_3 - \mathbf{p}_4) \\
\times \delta(\boldsymbol{\epsilon_c} + \boldsymbol{\epsilon}_2 - \boldsymbol{\epsilon}_3 - \boldsymbol{\epsilon}_4) \\
\times (2\pi\hbar)^3 [\delta(\mathbf{p} - \mathbf{p}_2) - \delta(\mathbf{p} - \mathbf{p}_3) - \delta(\mathbf{p} - \mathbf{p}_4)] \\
\times [(f_2 + 1) f_3 f_4 - f_2 (f_3 + 1)(f_4 + 1)].
\end{aligned}
\tag{2.44}
$$

This integral is directly connected to the source term $R(\mathbf{r}, t)$:

$$
R(\mathbf{r}, t) = \frac{\hbar}{|\phi(\mathbf{r}, t)|^2} \int \frac{d\mathbf{p}}{(2\pi\hbar)^3} C_{12}[f(\mathbf{p}, \mathbf{r}, t)]. \tag{2.45}
$$

The term C_{22} instead accounts for scattering processes involving two particles within the thermal cloud, and that leads to a rearrangement of the atoms in each mode:

$$
\begin{aligned}
C_{22}[f] = \frac{4\pi}{\hbar} g_{3d}^2 \int \frac{d\mathbf{p}_2}{(2\pi\hbar)^3} \int \frac{d\mathbf{p}_3}{(2\pi\hbar)^3} \int \frac{d\mathbf{p}_4}{(2\pi\hbar)^3} \\
\times (2\pi\hbar)^3 \delta(\mathbf{p} + \mathbf{p}_2 - \mathbf{p}_3 - \mathbf{p}_4) \\
\times \delta(\boldsymbol{\epsilon} + \boldsymbol{\epsilon}_2 - \boldsymbol{\epsilon}_3 - \boldsymbol{\epsilon}_4) \\
\times [(f + 1)(f_2 + 1) f_3 f_4 - f f_2 (f_3 + 1)(f_4 + 1)].
\end{aligned}
\tag{2.46}
$$

The ‘ZNG’ theory is a fully self-consistent dynamical approach, that can describe a considerable part of the physics of finite temperature BECs; it is however a method based on symmetry-breaking. For this reason it is not suitable to describe low-dimensional systems, where fluctuations are enhanced with respect to their three-dimensional counterpart; moreover it can not reproduce the formation of a condensate, as it assumes that a condensate already exists.

2.3.2 Number-conserving approach

The mean-field methods discussed in the previous sections are based on the assumption that the average of $\hat{\Psi}(\mathbf{r}, t)$ is $\phi(\mathbf{r}, t)$ (i.e. $\langle\hat{\Psi}(\mathbf{r}, t)\rangle = \phi(\mathbf{r}, t)$). This is the basis of a broken-symmetry procedure, whereby the phase of the condensate $\phi(\mathbf{r}, t)$ takes on a fixed value, thus implying that the number of particles is not conserved. From a mathematical point of view it is however desirable that for a closed system with a fixed number N of bosons, the average of the full Bose field operator is zero (i.e. $\langle N|\hat{\Psi}|N\rangle = 0$). The operator $\hat{\Psi}$ in fact annihilates an atom at position r and time t, and in the number basis representation one is left with $\langle N|N-1\rangle$, which is zero because of orthogonality between states with different number. One usually solves the problem by resorting to a different basis, where each state is represented by a coherent superposition of states with different number, e.g. $|N-1\rangle, |N\rangle, |N+1\rangle$... [120]. However, the splitting of Eq. (2.9), does not guarantee the necessary orthogonality between the condensate and the fluctuation operator.

Several works have been performed into this direction [112–114, 134], with the aim of preserving the number of atoms, and ensuring the correct orthogonality between the two parts of the system. It turns out that these number conserving approaches essentially lead to equations that look very similar but feature some subtle modifications, upon redefining the operators in the splitting of Eq. (2.8). In the work by S. A. Gardiner and Morgan [114], as reviewed in [120], the operator $\hat{\Psi}$ is first expanded in terms of an orthogonal set $\{\phi^N(\mathbf{r}), \varphi_i^N(\mathbf{r})\}$:

$$\hat{\Psi}(\mathbf{r},t) = \hat{a}_0\phi^N(\mathbf{r},t) + \hat{\delta}(\mathbf{r},t) = \hat{a}_0\phi^N(\mathbf{r},t) + \sum_{i\neq 0}\varphi_i(\mathbf{r},t)\hat{a}_i(t). \qquad (2.47)$$

Here $\hat{a}_0$, the condensate annihilation operator. is defined as the projection of the full Bose field operator onto the condensate state ϕ^N [114]:

$$\hat{a}_0(t) = \hat{P}\hat{\Psi}(\mathbf{r},t) = \int d\mathbf{r}\, \phi^N(\mathbf{r},t)\hat{\Psi}(\mathbf{r},t). \qquad (2.48)$$

The non-condensate operator is instead defined as the orthogonal projection [114]:

$$\hat{\delta}(\mathbf{r},t) = \hat{Q}\hat{\Psi}(\mathbf{r},t) = \int d\mathbf{r}'\, Q(\mathbf{r},\mathbf{r}',t)\hat{\Psi}(\mathbf{r}',t), \qquad (2.49)$$

where $Q(\mathbf{r},\mathbf{r}',t) = \delta(\mathbf{r}-\mathbf{r}') - \phi^N(\mathbf{r},t)[\phi^N(\mathbf{r}',t)]^*$.

Following the work of Castin and Dum [113], the condensate wave function ϕ^N is defined by using the Penrose-Onsager criterion [135]. The condensate number N_0 is then related to the single-body density matrix $\rho(\mathbf{r},\mathbf{r}',t)$ by the following expression:

$$N_0\phi^N(\mathbf{r},t) = \int d\mathbf{r}'\, \rho(\mathbf{r},\mathbf{r}',t)\phi^N(\mathbf{r}',t) = \int d\mathbf{r}'\, \langle\hat{\Psi}^\dagger(\mathbf{r}',t)\hat{\Psi}(\mathbf{r},t)\rangle\phi^N(\mathbf{r}',t). \qquad (2.50)$$

The integral in the above equation can be solved by replacing the full expression of Eq. (2.47); the orthogonality within the set $\{\phi^N(\mathbf{r}), \varphi_i^N(\mathbf{r})\}$ allows to reduce the above equation as:

$$N_0\phi^N(\mathbf{r},t) = \langle \hat{a}_0^\dagger \hat{a}_0 \rangle \phi^N(\mathbf{r},t) + \langle \hat{a}_0^\dagger \hat{\delta}(\mathbf{r},t)\rangle. \tag{2.51}$$

Multiplying by $[\phi^N]^*$ and integrating over $\mathbf{r}$, yields $N_0 = \langle \hat{a}_0^\dagger \hat{a}_0 \rangle$, and this guarantees that the following property is satisfied:

$$\langle \hat{a}_0^\dagger \hat{\delta}(\mathbf{r},t)\rangle = 0. \tag{2.52}$$

This result motivates the use of $\langle \hat{a}_0^\dagger \hat{\delta}(\mathbf{r},t)\rangle$ as the fluctuation operator: we notice that the above property is now a direct consequence of the orthogonality between the condensate and the other part of the system, unlike in the symmetry broken picture, where this result arises in an ad hoc manner [120]. There exist a number of different definitions for the fluctuation operator in the literature, e.g. $(\hat{a}_0^\dagger/\sqrt{\hat{N}_0})/\hat{\delta}(\mathbf{r},t)$ [113], or $(\hat{a}_0^\dagger/\sqrt{\hat{N}})/\hat{\delta}(\mathbf{r},t)$ [112]; in the work by S. A. Gardiner and Morgan [114] the fluctuation operator contains a prefactor of $1/\sqrt{N_0}$, so that the Bose field operator can be expressed in a number conserving manner as:

$$\hat{\Psi}(\mathbf{r},t) = \hat{a}_0\phi^N(\mathbf{r},t) + \sqrt{N_0}[a_0^\dagger]^{-1}\hat{\delta}^N(\mathbf{r},t). \tag{2.53}$$

At this stage one usually uses the same procedure as adopted in the mean-field treatments, i.e. to expand the full hamiltonian in powers of the fluctuation operator; since each of these terms contains a prefactor of $1/\sqrt{N_0}$, such expansion can be interpreted as a ratio of the non-condensate to condensate atoms. This procedure leads to the following generalised finite temperature Gross-Pitaevskii equation:

$$\begin{aligned} i\hbar\frac{\partial}{\partial t}\phi^N(\mathbf{r},t) &= [\hat{h}_0(\mathbf{r},t) - \lambda(t)]\phi^N(\mathbf{r},t) \\ &+ g(N_0(t) + \mathit{\Delta}N_0))|\phi^N(\mathbf{r},t)|^2\phi^N(\mathbf{r},t) \\ &+ 2g\tilde{n}^N(\mathbf{r},t)\phi^N(\mathbf{r},t) + g\tilde{m}^N(\mathbf{r},t)[\phi^N(\mathbf{r},t)]^* - f(\mathbf{r},t). \end{aligned} \tag{2.54}$$

The parameter λ takes the form of a nonlinear eigenvalue, whereas the function f ensures the orthogonality during the temporal evolution [114, 120]. The quantity $\mathit{\Delta}N_0 = (\langle \hat{N}_0^2\rangle - \langle \hat{N}_0\rangle^2)/N_0 - 1$ is instead related to statistical fluctuations, and usually is a small contribution [114, 120].

2.3.3 c-field methods

Classical field (c-field) approaches (recently reviewed in [115], see also [120, 136]) share a common feature that consists in treating the low-energy part of the full quantum Bose field operator as a classical object, in the limit that the mode occupation is very high. The discrete nature of these modes can therefore be approximated by a continuum, and a classical wave equation is suitable to describe their dynamics [137]. This is similar in spirit to the approach commonly used in electromagnetism, for which the quantum description of the blackbody radiation in terms of Planck's distribution can be replaced by a classical description using the Rayleigh-Jeans equation, in the long-wavelength limit (i.e. low energy). However, by analogy to the well known ultraviolet catastrophe of the electromagnetic field at short wavelengths, classical field approaches should only be used to describe the low-energy modes of the full Bose field operator. This is achieved by firstly imposing a high-energy cutoff, appropriately chosen to eliminate the high-energy modes; this also allows to use an effective field theory, where the details of the potential at short distances are unimportant, and one can use the s-wave approximation for the scattering [115]. The requirement on this high-energy cutoff is that it should be much greater than the chemical potential, μ, and the thermal energy, $k_B T$, such that these high-energy modes will not be occupied. The remaining part of the spectrum of the full Bose field operator $\hat{\Psi}$, is then further split into two subsets, referred to in the literature as coherent (or c-field region) and incoherent [115]:

$$\hat{\Psi}(\mathbf{r}) = \hat{\Psi}_{\mathbf{C}}(\mathbf{r}) + \hat{\Psi}_{\mathbf{I}}(\mathbf{r}). \tag{2.55}$$

In order to perform this split, a projection operator is introduced in the method, which projects the full Bosonic operator to the coherent region only [137]:

$$\hat{\Psi}_{\mathbf{C}}(\mathbf{r}) = P_{\mathbf{C}}[\hat{\Psi}(\mathbf{r})] = \sum_{n \in \mathbf{C}} \hat{a}_n \varphi_n(\mathbf{r}), \tag{2.56}$$

where the φ_n are the eigenvectors in the single-particle Hamiltonian.

- *The coherent region* includes all the highly occupied low-energy modes, up to a predetermined cutoff (not to be confused with the high-energy cutoff discussed before), which depends on the thermodynamic parameters of the system. The value of the cutoff is chosen in a such a way that the highest energy mode in the coherent region is highly occupied, i.e. that the mean average occupation of this mode lies in a range from 1 to 10 [115]. For the c-field to be treated classically, quantum corrections should be small; the mode occupation should therefore be compared to the minimum level of quantum fluctuations, which typically account for half a particle per mode [115].

- *The incoherent region* contains the high-energy modes that are instead sparsely occupied or vacuum modes, and therefore cannot be treated classically, but necessitate a quantum mechanical description. However as the dynamics of the c-field is only weakly influenced by the presence of the atoms in these high-energy modes [115], it is a reasonable first approximation to omit their dynamics.

There exist a number of distinct implementations of such classical field approaches, which differ in terms of technical aspects [115]; we discuss briefly here the stochastic projected Gross-Pitaevskii equation (SPGPE).

The stochastic projected Gross-Pitaevskii equation (SPGPE)

Among the distinct c-field approaches, the SPGPE [138, 139] is the most relevant to the topic discussed in this thesis, as it is closely related to the underlying theory of the model used here (i.e. Stoof's theory [116]). The SPGPE combines the kinetic theory of C. W. Gardiner and co-workers [140–142] with the formalism of finite temperature Gross-Pitaevskii equation of Davis and co-workers [143, 144]. In this approach the coherent c-field region is treated as an open system coupled to the incoherent region, which acts as a thermal bath and is assumed to be at equilibrium. A further approximation is done in this approach, requiring that all the frequencies of the c-field modes are much smaller than the thermal energy [139]; for this reason this method is more suitable to describe the physics at relatively high temperatures, e.g. typically from $T > 0.5T_\mathrm{c}$ up to $T \approx T_\mathrm{c}$ for a 3D system.

The SPGPE is derived by means of a master equation for the density operator associated to the c-field region; this master equation can then be mapped onto an equivalent Fokker-Planck equation, in terms of the Wigner probability distribution [145]. The resulting Fokker-Planck equation contains third order derivatives of the Wigner function which make the mapping to an equivalent stochastic representation not simple [145, 146]; however, as the modes in the c-field region are highly populated one can use the so-called Truncated Wigner approximation (TWA), by means of which these terms are discarded [146], and the mapping to a stochastic equation yields the SPGPE for the classical field $\varPhi_C$:

$$\begin{aligned}
d\varPhi_{\mathbf{C}}(\mathbf{r}) = P_{\mathbf{C}}\Big\{ &-\frac{i}{\hbar}\Big(-\frac{\hbar^2}{2m}\nabla^2 + V^{\text{ext}}(\mathbf{r}) + g_{3\text{d}}|\varPhi_{\mathbf{C}}(\mathbf{r})|^2\Big)\varPhi_{\mathbf{C}}(\mathbf{r})\,dt \\
&+ \frac{G(\mathbf{r})}{k_{\text{B}}T}\Big[\mu - \Big(-\frac{\hbar^2}{2m}\nabla^2 + V^{\text{ext}}(\mathbf{r}) + g_{3\text{d}}|\varPhi_{\mathbf{C}}(\mathbf{r})|^2\Big)\varPhi_{\mathbf{C}}(\mathbf{r})\,dt + dW_{\text{G}}(\mathbf{r},t)\Big] \\
&+ \int d\mathbf{r}' M(\mathbf{r}-\mathbf{r}')\frac{i\hbar\nabla\cdot J_{\mathbf{C}}(\mathbf{r}')}{k_B T}\varPhi_{\mathbf{C}}(\mathbf{r})\,dt + i\varPhi_{\mathbf{C}}(\mathbf{r})dW_{\text{M}}(\mathbf{r},t)\Big\}.
\end{aligned} \tag{2.57}$$

The first line of the right hand side of the equation is essentially the Gross-Pitaeskii equation, with the presence of the projector. The second line describes instead the growth processes, i.e. scattering events associated with transfer of atoms in (or out of) the coherent region. The rate of these collisions is given by the value of $G(\mathbf{r})$ [115], while their random character is ensured by the presence of the complex noise $dW_{\text{G}}(\mathbf{r},t)$. The third line is instead associated with scattering events (with amplitude $M(\mathbf{r}-\mathbf{r}')$), that lead to exchange of atoms between the coherent and incoherent region, but leave the particle number in each subsystem unchanged. The noise term, $dW_{\text{M}}(\mathbf{r},t)$, associated with these scattering events, is non-local (i.e. $\langle dW_{\text{M}}(\mathbf{r}',t')dW_{\text{M}}(\mathbf{r},t)\rangle = 2M(\mathbf{r}-\mathbf{r}')dt$) and multiplicative, and as a consequence the numerical implementation is not straightforward [137, 147]. However the equation can be simplified by discarding the terms of the third line (associated with scattering) yielding the so-called *simple growth* SPGPE [115, 148, 149]. The SPGPE has been applied in several contexts, e.g. study of vortex formation at the condensate transition [150]; for a review about the applications of the SPGPE, see Ref. [115]. In the next section we introduce a similar method, namely the Stochastic Gross-Pitaevskii equation [151].

2.4 The stochastic Gross-Pitaevskii equation

The SPGPE approach discussed in the previous section is closely related to the Stochastic Gross-Pitaevskii equation derived by Stoof [116] (see Chapter 3 for more details), which essentially relies on a description of the system in terms of an appropriate probability distribution. Despite different derivations the two approaches share key aspects in the underlying fundamental assumptions about the low-lying modes. It has been shown [120] that the two approaches are practically equivalent (although there may be additional issues with respect to numerical implementations) upon discarding the projector and the scattering terms in the

SPGPE.

The Stochastic Gross-Pitaevskii equation takes the form of a nonlinear dissipative Schrödinger equation, with the presence of a noise to mimic fluctuation, and describes the evolution of a set of (highly-populated) low-lying modes in contact with a "heat bath" [152]. It is particularly suitable to model physical systems in which fluctuations are enhanced, since the wavefunction in the SGPE represents the condensate and low-lying excitations on top of it.

The first application of the SGPE in its original form (see Eq. (3.11)) was by Stoof and Bijlsma [151], in which it was shown to qualitatevely recover the features of the experiment of Stamper-Kurn *et al.* [153]. Subsequently a variational approach was pursued in modelling the low-lying collective modes of a condensate with repulsive interactions at finite temperature [152], the growth and collapse of a condensate with attractive interactions [152] and the vortex motion in a partially Bose condensed gas [154]. The SGPE was also applied in the context of low-dimensional Bose gases [90], where good agreement was found with the modified Popov theory. The coherence properties of a one-dimensional Bose gas were also investigated in [155, 156], and a reduced form of the SGPE was used to investigate the dynamics of quasi-condensate on atom chip [157]. The SGPE has additionally been applied to the study of spontaneous solitons formation around the phase transition in a low-dimensional Bose gas [158, 159] and to the dynamics of dark solitons in elongated condensates at finite temperature [160].

In the next chapter we discuss the key aspects of the derivation of the SGPE by Stoof [151], and we then explain the model adopted throughout this work, which is based on a modified form of the SGPE.

2.5 Chapter summary

In this chapter we have presented theoretical approaches suitable for a description of weakly-interacting ultracold Bose gases. We started with a brief review of the Gross-Pitaevskii equation, that provides a mean-field treatment at zero temperature. We then included finite temperature effects, by discussing the Hartree-Fock and Hartree-Fock-Bogoliubov limits, which incorporate the static contribution from the thermal cloud and the anomalous average respectively, while only mean-field coupling is allowed. Beyond a symmetry-breaking procedure, we have discussed the modified Popov approach, that explicitly retains phase fluctuations. We then highlighted the main aspects of the Zaremba-Nikuni-Griffin (ZNG) approach, where the coupled dynamics of the condensate and the thermal cloud is described at the mean-field level. One of the limitations of a broken-symmetry procedure, is that the number of atoms is not conserved: this problem is solved in the number-conserving approach, also discussed here. We have then concluded this chapter with a general introduction to classical field (c-field) methods, where a classical wave equation describes the dynamics of the low energy part of the full quantum Bose operator. We have mainly focused on the implementation known as Stochastic Projected Gross-Pitaevskii equation (SPGPE), since it is closely related to the Stochastic GPE, briefly introduced here and discussed in the next chapter.

Part II

A self-consistent quasi-1d stochastic model

Part II introduces the theoretical model we use throughout this thesis. We initally outline the derivation of the Stochastic Gross-Pitaevskii equation (SGPE). We then discuss the 1D-3D crossover regime (characterised by $\mu \sim \hbar\omega_\perp$), in the simplest mean-field limit and derive an effective 1D equation, which also incorporates the contribution from the transverse degrees of freedom. Subsequently we extend, in a somewhat heuristical manner, the above result to the SGPE, by the inclusion of stochastic terms, thereby obtaining the quasi-one-dimensional SGPE: this provide an accurate description of the axial modes in a cigar-shaped condensate. The transverse excited modes with energy $k_\mathrm{B}T \gtrsim \hbar\omega_\perp$ are instead treated statically, as independent 1D Bose gases. The quasi-one-dimensional SGPE together with a static treatment of few transverse excited modes provide an ab initio self-consistent model for quasi-one-dimensional experiments, in the regime $\mu, k_\mathrm{B}T \gtrsim \hbar\omega_\perp$. We also provide the detailed numerical procedure that will be adopted in Part III of this thesis, and show some examples of physical observables calculated at equilibrium, such as density profiles and first- and second-order correlations functions. Finally we show how to extract the density and phase coherent parts from the total density distribution within our model.

We point out that in our numerical simulations we use realistic parameters, taken from the experiments we model in Part III of this thesis.

Chapter 3

The quasi-1D stochastic Gross-Pitaevskii equation (SGPE)

3.1 Origin and formulation of the SGPE

In this section we provide a description of the Stochastic Gross-Pitaevskii equation, which is a theoretical model describing the nonequilibrium dynamics of a harmonically confined, weakly-interacting Bose gas at finite temperature. We use the approach given by Stoof [116, 117, 151, 152, 161], which is similar in spirit, but based on different methods and implementation, to the approach of C. W. Gardiner and co-workers [138, 139, 141, 142], as already discussed in Part I of this thesis.

Focusing on the approach of Stoof, he gives a unified description of the whole Bose gas in terms of a Wigner distribution function $P[\varPhi^*, \varPhi; t]$, which describes the probability for the system to be in a coherent state $|\varPhi(\mathbf{r}; t)\rangle$ [1]. Using a functional formulation of the Keldysh formalism [162, 163], he derives a Fokker-Planck equation for the time evolution of the above probability density distribution, associated with the whole matter wave field.

In order to solve the full equation, one can use a Hartree-Fock type *ansatz*, which consists of splitting the Wigner probability distribution into a product, as $P[\varPhi^*, \varPhi; t] = P_0[\psi^*, \psi; t]P_1[\phi'^*, \phi'; t]$: here P_0 and P_1 are the distributions describing the probability for the system to be in the condensed [2] (ψ) and noncondensed (ϕ') part respectively [151]. This splitting naturally leads to a system of coupled equations: replacing this *ansatz* in the full Fokker-Planck equation, and integrating

---

[1] A coherent state is an eigenstate of the annihilation operator.

[2] Here the word 'condensed' has a broader meaning than its Gross-Pitaevskii counterpart, as will be explained later in the text.

over the condensate degrees of freedom, leads to a quantum Boltzmann equation for the time evolution of the noncondensed part of the gas (see Appendix A).

The integration over the non-condensate degrees of freedom yields instead a Fokker-Planck equation, describing the dynamics of the coherent (low-energy) part of the system [116, 152]:

$$\begin{aligned}
&i\hbar\frac{\partial}{\partial t}P_0[\psi^*,\psi;t] = \\
&-\int d\mathbf{r}\frac{\delta}{\delta\psi(\mathbf{r})}\Big(-\frac{\hbar^2\boldsymbol{\nabla}^2}{2m}+V^{\text{ext}}(\mathbf{r})-\mu(t)-iR(\mathbf{r},t)+g_{3d}|\psi(\mathbf{r})|^2\Big)\psi(\mathbf{r})P_0[\psi^*,\psi;t] \\
&+\int d\mathbf{r}\frac{\delta}{\delta\psi^*(\mathbf{r})}\Big(-\frac{\hbar^2\boldsymbol{\nabla}^2}{2m}+V^{\text{ext}}(\mathbf{r})-\mu(t)+iR(\mathbf{r},t)+g_{3d}|\psi(\mathbf{r})|^2\Big)\psi^*(\mathbf{r})P_0[\psi^*,\psi;t] \\
&-\frac{1}{2}\int d\mathbf{r}\frac{\delta^2}{\delta\psi(\mathbf{r})\delta\psi^*(\mathbf{r})}\hbar\Sigma^K(\mathbf{r},t)P_0[\psi^*,\psi;t].
\end{aligned} \tag{3.1}$$

In this treatment ψ may be referred to as an 'order parameter' describing the low-energy part of the system, including (but not restricted to) the condensate [117]. Loosely ψ describes the condensate plus low-lying excitations. A strict division from the high-lying modes (i.e. noncondensed part ϕ') is made in the numerical implementation. Unlike the wavefunction ϕ in the Gross-Pitaevskii equation, which only describes the condensate in the mean-field approximation, in this context ψ also accounts for the effects of fluctuations around it [117]. In order to allow for a full dynamical treatment, with the thermal cloud being not in thermal equilibrium, the chemical potential μ is initially kept time dependent; however, it is not the purpose of this work to solve the Boltzmann equation (see Appendix A), therefore we will assume the thermal cloud to be sufficiently close to equilibrium, as will be explained later.

The imaginary term, iR, in Eq. (3.1) describes the interaction between the low-energy region of the system and the high-lying thermal cloud (i.e. exchange of atoms between these two subsystems) due to elastic collisions. The full expression is given (in the Hartree-Fock approximation) by:

$$\begin{aligned}
R(\mathbf{r},t) =& 2\pi g_{3d}^2\int\frac{d\mathbf{p}_1}{(2\pi)^3}\int\frac{d\mathbf{p}_2}{(2\pi)^3}\int\frac{d\mathbf{p}_3}{(2\pi)^3}(2\pi)^3\times\delta(\mathbf{p}_1-\mathbf{p}_2-\mathbf{p}_3) \\
&\delta(\epsilon_c+\epsilon_1-\epsilon_2-\epsilon_3)\times[N_1(1+N_2)(1+N_3)-(1+N_1)N_2N_3].
\end{aligned} \tag{3.2}$$

The conservation of momentum and energy (i.e. elastic collisions), is ensured by the presence of the δ functions. The functions $N_i(\mathbf{r},\mathbf{p}_i,t)$ are the Wigner distributions for the thermal particles in the high-lying modes of the system, and can be found by solving Eq. (A.1); at equilibrium these are in general Bose distributions. The scattering processes described in Eq. (3.2) are associated with transfer of atoms in the condensate, $\mathit{\Gamma}_{\text{in}} \propto |\psi|^2(1+N_1)N_2N_3$, and out of the condensate, $\mathit{\Gamma}_{\text{out}} \propto |\psi|^2 N_1(1+N_2)(1+N_3)$. The distribution functions N_i represent the bosonic enhancement of the scattering into the populated level i, whereas additional contribution of the "1" in N_i+1 is associated with spontaneous scattering events.

The Keldysh self-energy $\hbar\mathit{\Sigma}^k$ appearing in the diffusive term of Eq. (3.1) provides the strength of the thermal fluctuations in the system, associated with incoherent collisions between the low-lying energy modes and the high incoherent region in the system. The full expression is as follows [152]:

$$\begin{aligned}\hbar\mathit{\Sigma}^K(\mathbf{r},t) = -4\pi i g_{3d}^2 &\int \frac{d\mathbf{p}_1}{(2\pi)^3}\int \frac{d\mathbf{p}_2}{(2\pi)^3}\int \frac{d\mathbf{p}_3}{(2\pi)^3}(2\pi)^3 \\ &\times \delta(\mathbf{p}_1-\mathbf{p}_2-\mathbf{p}_3)\delta(\epsilon_c+\epsilon_1-\epsilon_2-\epsilon_3) \\ &\times [N_1(1+N_2)(1+N_3)+(1+N_1)N_2N_3].\end{aligned} \tag{3.3}$$

Equations (3.2) - (3.3) describe the dissipation and the fluctuations in the system; despite looking rather similar at first sight, the two equations account for the scattering mechanisms in different ways. While in Eq. (3.2) the two scattering processes are subtracted, in Eq. (3.3) these two contributions are added instead. A natural consequence is that at equilibrium the contribution from the dissipative term $iR(\propto \mathit{\Gamma}_{\text{out}} - \mathit{\Gamma}_{\text{in}})$ is zero on average; so although transfer of atoms still occurs, there is no net exchange of atoms between condensate and thermal cloud. The fluctuations $\hbar\mathit{\Sigma}^k \propto (\mathit{\Gamma}_{\text{out}}+\mathit{\Gamma}_{\text{in}})/2$, described by Eq. (3.3), are still present, thus meaning that a dynamical equilibrium is reached when the fluctuations balance the dissipation in the system.

The energies of the thermal atoms are given by the following expression:

$$\epsilon_i = \frac{|\mathbf{p}_i|^2}{2m} + V^{\text{ext}}(\mathbf{r}) + 2g_{3d}|\langle\psi(\mathbf{r},t)\rangle|^2. \tag{3.4}$$

We notice that the contribution due to the mean-field of the thermal component above the cut-off has not been taken into account in the above equation, under the assumption that it has a negligible effect on the properties of the condensate (see also Ref. [164]).

The energy necessary to remove one atom from the low-lying modes represented by ψ is instead given by [116]:

$$\epsilon_c = -\frac{\hbar^2 \boldsymbol{\nabla}^2}{2m} + V^{\text{ext}}(\mathbf{r}) + g_{3d}|\psi(\mathbf{r},t)|^2. \tag{3.5}$$

Here ϵ_c represents an operator, which appears in both Eq. (3.2) and Eq. (3.3). The dependence of both the dissipation $iR(\mathbf{r},t)$ and the Keldysh self-energy $\Sigma^K(\mathbf{r},t)$ on the wavefunction ψ (through their dependence on ϵ_c) makes a numerical implementation of the model very complicated at this stage, because the Langevin equation corresponding to the Fokker Planck equation will in general contain multiplicative noise, with a prefactor that depends on ψ [152]. In order to make the numerical treatment easier we may therefore assume that the thermal cloud is near-equilibrium, and acts as a heat bath in contact with the low-lying modes in the system. Under this assumption, the Wigner distribution functions for the thermal cloud $N_i(\mathbf{r},\mathbf{p}_i,t)$, which for a consistent dynamical description should be derived by solving Eq. (A.1), can be replaced by the Bose-Einstein distributions $N_{\text{BE}}(\epsilon_i) = [e^{\beta(\epsilon_i-\mu)} - 1]^{-1}$, which are the equilibrium solutions to the full quantum Boltzmann equation. With this assumption, one can then derive a relation between the magnitude of the fluctuations and the dissipation in the system [116, 152]:

$$iR(\mathbf{r};\epsilon_c) = -\frac{1}{2}\hbar\Sigma^K(\mathbf{r};\epsilon_c)[1 + 2N_{\text{BE}}(\epsilon_c)]^{-1}. \tag{3.6}$$

This is here the form of the fluctuation-dissipation relation, which states that at equilibrium the amount of fluctuation in the system is related to the dissipation. Equation (3.6) ensures that the system tends to the correct equilibrium distribution, and is only valid in the regime of linear response (i.e. near-equilibrium) [152].

The Fokker-Planck equation can now be mapped onto an equivalent Langevin equation, describing the evolution of the low-lying energy modes, in the presence of a static thermal cloud, which acts as a reservoir. The Langevin equation takes the form of a nonlinear dissipative Schrödinger equation, in the presence of noise:

$$i\hbar\frac{\partial\psi(\mathbf{r},t)}{\partial t} = \left[-\frac{\hbar^2\nabla^2}{2m} + V^{\text{ext}}(\mathbf{r}) - iR(\mathbf{r},t) + g_{3d}|\psi(\mathbf{r},t)|^2 - \mu \right]\psi(\mathbf{r},t) + \eta(\mathbf{r},t). \tag{3.7}$$

For a partially Bose condensed gas, the low-lying modes in the system are likely to be highly occupied; the term $\beta(\epsilon_c - \mu)$ is in fact very small ($\ll 1$) at high temperatures (sufficiently close to or below the critical temperature) and near equilibrium (i.e. $\epsilon_c - \mu \ll 1$). This allows to replace the fluctuation-dissipation relation (Eq. (3.6)) with its classical counterpart, whereby one perform the approximation $N_{\mathrm{BE}} + 1/2 \simeq [\beta(\epsilon_c - \mu)]^{-1}$ [165]. This approximation is justified as long as the average number of particles per mode is larger than one (typically between 1 and 10) [115]. With the above classical approximation, the term in brackets appearing in Eq. (3.6) can be recast as follows:

$$[1 + 2N_{BE}(\epsilon_c)]^{-1} \simeq \frac{1}{2}\beta(\epsilon_c - \mu). \tag{3.8}$$

Replacing this back into Eq. (3.6) leads to the classical approximation of the fluctuation-dissipation relation:

$$-iR(\mathbf{r};t) = \frac{\beta}{4}\hbar\Sigma^K(\mathbf{r};t)(\epsilon_c - \mu), \tag{3.9}$$

where ϵ_c is still given by Eq. (3.5). It is important to notice that the classical approximation to the fluctuation-dissipation theorem makes the equation amenable to numerical implementation. By replacing Eq. (3.9) (using the full expression for ϵ_c of Eq. (3.5)), the initial Fokker-Planck equation can now be recast as [152]:

$$\begin{aligned}
&i\hbar\frac{\partial}{\partial t}P_0[\psi^*, \psi; t] = \\
&-\frac{\beta}{4}\int d\mathbf{r}\,\hbar\Sigma^K(\mathbf{r},t)\frac{\delta}{\delta\psi(\mathbf{r})}\bigg(-\frac{\hbar^2\boldsymbol{\nabla}^2}{2m} + V^{\mathrm{ext}}(\mathbf{r}) + g_{3d}|\psi(\mathbf{r})|^2 - \mu(t)\bigg)\psi(\mathbf{r})P_0[\psi^*, \psi; t] \\
&-\frac{\beta}{4}\int d\mathbf{r}\,\hbar\Sigma^K(\mathbf{r},t)\frac{\delta}{\delta\psi^*(\mathbf{r})}\bigg(-\frac{\hbar^2\boldsymbol{\nabla}^2}{2m} + V^{\mathrm{ext}}(\mathbf{r}) + g_{3d}|\psi(\mathbf{r})|^2 - \mu(t)\bigg)\psi^*(\mathbf{r})P_0[\psi^*, \psi; t] \\
&-\frac{1}{2}\int d\mathbf{r}\,\hbar\Sigma^K(\mathbf{r},t)\frac{\delta^2}{\delta\psi(\mathbf{r})\delta\psi^*(\mathbf{r})}P_0[\psi^*, \psi; t].
\end{aligned} \tag{3.10}$$

Next we discuss the formulation of the SGPE in three dimensions [152].

3.1.1 3D SGPE

The corresponding Langevin equation (formally equivalent to the Fokker-Planck of Equation. (3.10)) for the low-lying modes in the system can be re-written as:

$$
\begin{aligned}
&i\hbar\frac{\partial\psi(\mathbf{r},t)}{\partial t} = \\
&\left(1+\frac{\beta}{4}\hbar\Sigma^K(\mathbf{r},t)\right)\left[-\frac{\hbar^2\nabla^2}{2m}+V^{\mathrm{ext}}(\mathbf{r})+g_{3d}|\psi(\mathbf{r},t)|^2-\mu\right]\psi(\mathbf{r},t)+\eta(\mathbf{r},t).
\end{aligned}
\tag{3.11}
$$

The noise term $\eta(\mathbf{r},t)$ has Gaussian correlations, defined as:

$$
\langle\eta^*(\mathbf{r},t)\eta(\mathbf{r}',t')\rangle = \frac{i\hbar^2}{2}\Sigma^K(\mathbf{r},t)\delta(t-t')\delta(\mathbf{r}-\mathbf{r}'),
\tag{3.12}
$$

where the strength of the noise is given by the Keldysh self-energy in Eq. (3.3). Eq. (3.11) is the so-called Stochastic Gross-Pitaevskii equation (SGPE); it describes both the effect of dissipation and fluctuations in the system. It was first used in [117] to discuss reversible formation of a condensate when cycling through the phase transition. Since then, it has been used under the assumption that the thermal cloud is sufficiently close to equilibrium, which is equivalent to assuming that the high-energy modes thermalise on a very short timescale compared to the dynamics of the low-energy modes. The thermal cloud therefore behaves as a heat bath with a fixed temperature T and chemical potential μ, in contact with the low-lying energy modes in the system, represented by ψ.

3.1.2 Key considerations

Physical observables in the SGPE are obtained by averaging the stochastic field ψ over different realizations of the noise. In particular, since ψ is associated with both the mean-field and fluctuations around it (i.e. it implicitly retains information on density and phase fluctuations), correlation functions of any order can be calculated within this theory. This is achieved upon making the replacement of the Bose field operator $\hat{\Psi}$, with the stochastic field ψ such that [156]:

$$
\langle\hat{\Psi}^\dagger(z,t)\hat{\Psi}(z',t')\rangle \rightarrow \langle\psi^*(z,t)\psi(z',t')\rangle.
\tag{3.13}
$$

For example the axial density (corresponding to transversely integrated density over the low-lying energy modes), at time t is given by $\langle\psi^*\psi\rangle = \sum_{i=1}^{N}\psi_i^*\psi_i/N$, where i identifies a specific noise realization, while N is the total number of stochastic trajectories, over which the wavefunction ψ is sampled. Nonetheless single numerical realisations in the SGPE (i.e. single stochastic trajectories) are still to be considered, as these contain essential informations (e.g. regarding fluctuations in the system) that are needed when comparing to experimental results (see Section 4.2).

3.1.3 Formulation in 1D

Next we focus on the formulation of the Stochastic Gross-Pitaevskii equation in one dimension. This is done to prepare the ground for the theoretical model we explain in Section 3.3 and use throughout this work (with direct comparison to experiments discussed in Part III).

We consider a weakly interacting one dimensional Bose gas confined in a harmonic potential; we assume the conditions $\hbar\omega_\perp > \mu, k_BT$ and $\omega_\perp \gg \omega_z$, where $\omega_\perp$ and ω_z are the transverse and axial frequencies respectively. One of the consequences of such a condition is that the main dynamics occurs along the axial direction z, whereas the system is tightly confined in the radial direction, where the motion is reduced to the zero point oscillation. The SGPE in one dimension takes on the following expression:

$$\begin{aligned} &i\hbar\frac{\partial\psi(z,t)}{\partial t} = \\ &\Big(1 - i\gamma(z,T,t)\Big)\Big[-\frac{\hbar^2}{2m}\frac{\partial^2}{\partial z^2} + \frac{1}{2}m\omega_z^2 z^2 + g_{1d}|\psi(z,t)|^2 - \mu\Big]\psi(z,t) + \eta(z,t), \end{aligned} \tag{3.14}$$

where the interaction strength $g_{1d} = g_{3d}/2\pi l_\perp^2 = 2\hbar a_\mathrm{s}\omega_\perp$ [84]. This equation is essentially equivalent to the *simple growth* stochastic projected Gross-Pitaevskii equation (SPGPE) used and discussed by Davis and co-workers in [115], with the main difference arising from the presence of a projector (see also [120] for a comparison between the two schemes). In Eq. (3.14) γ has been defined via:

$$\gamma = i\frac{\beta}{4}\hbar\Sigma^K, \tag{3.15}$$

with the Keldysh self-energy calculated from Eq. (3.3). The term γ simulates the interaction between the system (i.e. low-lying highly populated modes) parametrised by ψ and the high-lying modes ("heat bath"). It also sets the rate of growth towards the equilibrium result; although it has in general both spatial and time dependence, in this work we do not solve the integral in Eq. (3.3), but we use the following approximation:

$$\gamma \simeq \kappa \times \frac{4mk_BT}{\pi}\left(\frac{a_\mathrm{s}}{\hbar}\right)^2. \tag{3.16}$$

This approximation to the damping term was first used by Penckwitt *et al.* [166]

to describe vortex dynamics, and it was found that the value $\kappa = 3$ yields good agreement with the typical experimental growth. Although this is an expression valid in three dimensions, this does not affect the equilibrium properties calculated in this work. The value of γ in fact only determines how the system relaxes (dynamically) to equilibrium: the higher (lower) is the value for γ, the shorter (longer) is the time needed to reach the equilibrium state. We point out that for the purpose of our work, which is mainly focussed on investigating the properties of weakly interacting Bose gases at equilibrium, neglecting the spatial dependence in γ does not have drastic consequences on the equilibrium state, as also discussed in [165, 167].

The noise term η is related to the values of γ and temperature and is characterised by Gaussian correlations:

$$\langle \eta^*(z,t)\eta(z',t')\rangle = 2\hbar k_B T \gamma(z,t)\delta(t-t')\delta(z-z'). \tag{3.17}$$

The presence of the noise is essential to initiate the growth process [168]: the wavefunction ψ is in fact equal to zero at time $t = 0$, and the noise is responsible for randomly seeding the modes in the system, which then evolve according to Eq. (3.14). The presence of the noise is therefore crucial at least for the initial stages of the formation of the condensate. Within the SGPE theory, the growth to equilibrium is a dynamical process, i.e. the system relaxes to the equilibrium configuration in a dynamical manner, when scattering and fluctuation balance out (see Section 3.4).

To conclude this preliminary discussion of the SGPE in one dimension, we note that the one dimensional conditions $\mu, k_B T \ll \hbar\omega_\perp$ under which Eq. (3.14) can be applied are rather extreme, and were not fulfilled in the experimental cases we will consider in Part III of this thesis. The experiments under investigation are in fact characterised by the more relaxed conditions $\mu \lesssim \hbar\omega_\perp$, $k_B T \sim \text{few}\,\hbar\omega_\perp$, for the experiments [59–61] investigated in Chapter 4, and $\mu, k_B T \sim \text{few}\,\hbar\omega_\perp$, for the experiments [54, 95] analysed in Chapter 5-6; we therefore semi-heuristically propose a quasi-one-dimensional extension to Eq. (3.14), in order to account for the bulging of the condensate in the transverse direction as well as the excited transverse modes being also populated. In the next section we first discuss how this extension arises in the context of mean-field model, by deriving a quasi-one-dimensional Gross-Pitaevskii equation; we then apply (in a somewhat heuristic manner) the same approach to the Stochastic Gross-Pitaevskii equation.

3.2 The Gross-Pitaevskii equation in the 1D-3D crossover regime

The aim of this section is to discuss how one can obtain an effective 1D equation that still incorporates some features of elongated 3D systems. Our derivation here is given in the context of the simple mean-field Gross-Pitaevskii equation. However, this is directly relevant to our subsequent stochastic formulation. The derivation presented here mainly follows the arguments used in the approach of Gerbier [101], and Mateo *et al* [169]. Our starting point is the 3D time dependent Gross-Pitaevskii equation, which takes the usual form:

$$i\hbar\frac{\partial\phi(\mathbf{r},t)}{\partial t}=\left[-\frac{\hbar^2\boldsymbol{\nabla}^2}{2m}+V^{\mathrm{ext}}(\mathbf{r})+g|\phi(\mathbf{r},t)|^2\right]\phi(\mathbf{r},t). \tag{3.18}$$

We consider a weakly interacting Bose gas in a cylindrical harmonic trap, such that $V^{\mathrm{ext}}(\mathbf{r})=m\omega_\perp^2r_\perp^2/2+V(z)$. We consider the case where the gas is tightly confined in the radial direction, such that the aspect ratio $\omega_\perp/\omega_z\gg 1$, and we allow for a certain number of transverse modes to be occupied, i.e. $\mu\simeq$ few $\hbar\omega_\perp$. In such a regime the radial degrees of freedom are not completely frozen (the radial motion is not reduced to the zero point oscillation); we therefore need an effective 1D equation, able to also incorporate the contribution from the dynamics of the radial excited states. Since the aspect ratio is very high, the evolution of the radial degrees of freedom occurs on a much faster timescale than the axial one, (the characteristic time $\tau\simeq\omega_\perp^{-1}\ll\omega_z^{-1}$). We can therefore use the *adiabatic approximation* [170], as the radial degrees of freedom adapt almost instantaneously to the new axial configuration. As a consequence the correlations between the transverse and axial degrees of freedom are negligible, and we can factorise the wavefunction as follows:

$$\phi(\mathbf{r},t)=\Phi(r_\perp;z,t)f(z,t). \tag{3.19}$$

Inserting the wavefunction into Eq. (3.18) yields:

$$\left(i\hbar\frac{\partial f}{\partial t}+\frac{\hbar^2}{2m}\frac{\partial^2 f}{\partial z^2}-V(z)f\right)\Phi=\left(-\frac{\hbar^2}{2m}\boldsymbol{\nabla}_\perp^2\Phi+\frac{1}{2}m\omega_\perp^2r_\perp^2\Phi+g_{3d}N|f|^2|\Phi|^2\Phi\right)f. \tag{3.20}$$

The axial variation of the radial part of the wavefunction has been neglected in the above equation, since the axial potential is assumed to be sufficiently shallow, as generally applicable for a highly elongated condensate. The time derivative of the radial part has also been neglected, as a consequence of the adiabatic approximation.

Multiplying both sides of the equation by Φ^* and integrating over the radial coordinates yields:

$$\left(i\hbar\frac{\partial f}{\partial t} + \frac{\hbar^2}{2m}\frac{\partial^2 f}{\partial z^2} - V(z)f\right)\Phi = \mu_\perp f, \tag{3.21}$$

where we have defined the local chemical potential:

$$\mu_\perp = \int d^2r_\perp \Phi^* \left(-\frac{\hbar^2}{2m}\boldsymbol{\nabla}_\perp^2 + \frac{1}{2}m\omega_\perp^2 r_\perp^2 + g_{3d}N|f|^2|\Phi|^2 \right)\Phi. \tag{3.22}$$

We now minimise Eq. (3.22): this is because in condensates with repulsive interactions, there is a lower bound on $\mu_\perp$ [170]. A reasonable ansatz for the radial part of the wavefunction is a Gaussian whose width σ is a variational parameter:

$$\Phi = \frac{1}{\sqrt{\pi}\sigma}e^{-\frac{{r_\perp}^2}{2\sigma^2}}. \tag{3.23}$$

In the 1D limit the system is transversally in the ground state given by a Gaussian with width $l_\perp = \sqrt{\hbar/m\omega_\perp}$ (harmonic oscillator length); in the 1D-to-3D dimensional crossover instead, we expect few transverse excited states to be populated, and the width of the Gaussian therefore becomes bigger.

By performing the integration in Eq. (3.22), we obtain the following result for $\mu_\perp$:

$$\mu_\perp = \frac{\hbar^2}{2m}\sigma^{-2} + \frac{m\omega_\perp^2}{2}\sigma^2 + \frac{1}{2\pi}g_{3d}N|f|^2\sigma^{-2}. \tag{3.24}$$

By minimising this expression with respect to the width, σ, we obtain:

$$\sigma^2 = l_\perp^2\sqrt{1 + 4a_\mathrm{s}N|f|^2}. \tag{3.25}$$

The new equation of state then reads as:

$$\mu_\perp = \hbar\omega_\perp\sqrt{1 + 4a_\mathrm{s}N|f|^2}. \tag{3.26}$$

By replacing the above expression into Eq. (3.21), we find that the new equation of motion for the axial wavefunction becomes:

$$i\hbar\frac{\partial f}{\partial t} = -\frac{\hbar^2}{2m}\frac{\partial^2 f}{\partial z^2} + V(z)f + \hbar\omega_\perp(\sqrt{1 + 4a_\mathrm{s}N|f|^2} - 1)f. \tag{3.27}$$

This is an effective 1D equation, which also incorporates transverse effects (due to interactions) via the presence of the modified non-linearity $\hbar\omega_\perp\sqrt{1 + 4a_\mathrm{s}N|f|^2}$, as opposed to the nonlinear term $g_{1\mathrm{d}}|f|^2$ in the ordinary GPE. This modification is likely to become important when the inequality $\mu \ll \hbar\omega_\perp$ is not satisfied, as demonstrated experimentally by Kruger *et al.* [91].

3.3 Quasi-1D model

Equipped with the previous tools, in this section we introduce a modified stochastic equation which enables us to perform a successful *ab initio* description of weakly interacting ultracold Bose gas experiments, in the 'intermediate' regime $\mu, k_B T \lesssim \text{few}\ \hbar\omega_\perp$, where quasi-condensate physics dominates, but transverse effects still need to be appropriately accounted for. The model we present consists of two parts: i) a quasi-one-dimensional form of the stochastic Gross-Pitaevskii equation, to describe the dynamics of the low-energy axial modes, and ii) an additional equation to account for the static contribution of the excited transverse modes. In Part III of this thesis, we demonstrate that these two equations provide excellent *ab initio* prediction of experimental results from five independent experiments [54, 59–61, 95].

3.3.1 Quasi-1D stochastic Gross-Pitaevskii equation

The modified one-dimensional (1D) form [118] of the stochastic Gross-Pitaevskii equation (SGPE) [116, 117, 139], takes the form:

$$i\hbar\frac{\partial\psi(z,t)}{\partial t} = \\ [1 - i\gamma(z,t)]\left(-\frac{\hbar^2}{2m}\frac{\partial^2}{\partial z^2} + \frac{1}{2}m\omega_z^2 z^2 + \hbar\omega_\perp\left[\sqrt{1+4|\psi|^2 a_\mathrm{s}} - 1\right] - \mu\right)\psi(z,t) + \eta(z,t). \tag{3.28}$$

It was first proposed in [118] (joint work in which I was involved) — where it was found to be essential to accurately simultaneously reproduce both *in situ* density profiles and density fluctuations obtained in several recent quasi-one-dimensional experiments [59–61].

It differs from the one-dimensional SGPE of Eq. (3.14) in the form of the nonlinear term $\hbar\omega_\perp\left[\sqrt{1+4|\psi|^2 a_\mathrm{s}} - 1\right]$, as opposed to $2\hbar\omega_\perp a_\mathrm{s}|\psi|^2$ of Eq. (3.14). This modification accounts for the transverse effects when $\mu \lesssim \text{few}\ \hbar\omega_\perp$. This condition in fact leads to a swelling of the condensate in the transverse direction, relative to the true 1D transverse ground state, just as in the ordinary GPE. It is therefore necessary to account for the fact that the system is no longer confined trasversely into the ground state of the harmonic potential, but it populates few transverse modes. This quasi-1D effect, which is due to repulsive interactions and captured by the new nonlinearity in Eq. (3.28) was verified experimentally in [91]. It is important to notice that the term $\hbar\omega_\perp[\sqrt{1+4|\psi|^2 a_\mathrm{s}}-1]$ in Eq. (3.28), reduces to $2\hbar\omega_\perp a_\mathrm{s}|\psi|^2$, in the limit $4|\psi|^2 a_\mathrm{s} \ll 1$. This result is exactly the nonlinear term, $g_{1d}|\psi|^2$, appearing in the one-dimensional SGPE of Eq. (3.14). This shows that for small axial densities, such that $4|\psi|^2 a_\mathrm{s} \ll 1$, the quasi-one-dimensional SGPE recovers the one-dimensional form. This has also been shown in the context of the ordinary Gross-Pitaevskii equation in Refs. [82, 101, 171–173].

The wavefunction ψ is associated, as in Eq. (3.14), with the low-lying (highly-populated) axial modes, up to a cut-off that separates these modes from the high-energy ones assumed to be at equilibrium and acting as a heat bath. The density profile $|\psi|^2$ obtained by numerically solving Eq. (3.28) will undergo appropriate averaging over different realizations of the noise. Although a single-run density profile contains qualitatively important information, it is generally very noisy. The process of averaging over a large number ($\sim 10^3$) of runs results instead in a very smooth density profile (but washes away features that vary from realisation to realisation, e.g spontaneous dark soliton formation).

3.3.2 Transverse thermal atoms

The equation discussed in the previous section describes the dynamics of the low-energy axial modes, and incorporates the quasi-one-dimensional effects resulting from the condition $\mu \lesssim \text{few } \hbar\omega_\perp$. However the experiments under investigation in Part III of this thesis, are characterized by a further important condition, i.e. $k_B T \lesssim \text{few } \hbar\omega_\perp$. This means that the particle thermal energy, $k_B T$, is also of the same order of the transverse excitation energy, $\hbar\omega_\perp$, and therefore the transverse excited modes are populated. In order to match to experimental atom numbers and density profiles, it is therefore crucial to also include in our treatment the (static) contribution of transverse thermal atoms with energy greater than $\hbar\omega_\perp$. These transverse modes are treated as independent 1D Bose gases, and their (static) contribution to the transversely integrated density profile is derived by solving the following equation:

$$n_\perp(z;\mu,T) = \frac{1}{\lambda_\mathrm{dB}}\sum_{j=1}^{\infty}(j+1)g_{1/2}\left(e^{\mu_j(z)/k_B T}\right). \tag{3.29}$$

Here $g_{1/2}(e^{\mu_j(z)/k_BT}) = \sum_{l=1}^{\infty}(e^{\mu_j(z)/k_BT})^l/l^{1/2}$ is the polylogarithm (or Bose function) of order $1/2$, and $\lambda_{\rm dB} = h/\sqrt{2\pi m k_B T}$ is the thermal de Broglie wavelength. The fraction of atoms in the transverse modes is therefore accounted for by summing over transverse quantum levels j ($j \geqslant 1$) with degeneracy $j+1$. Such an approach of including the above cut-off static thermal cloud component into the formalism has been implemented and described in other works (e.g. [60, 174, 175]).

We now describe the two different levels of approximation to the term $\mu_j(z)$ (appearing in Eq. (3.29)) that we use throughout this work. In general we find $\mu_j(z) = \mu - V^{\rm eff}(z) - j\hbar\omega_\perp$; for Eq. (3.29) to work, we require $\mu_j(z) < 0$ for all z. In principle $V^{\rm eff}(z) = V(z) + 2g_{\rm 1d}(\langle|\psi(z)|^2\rangle + n_\perp(z))$; however it is tempting to discard the contribution $2g_{\rm 1d}(\langle|\psi(z)|^2\rangle + n_\perp(z))$. This does not have a significant effect on truly 1D weakly-interacting gases, but it does prove crucial when $\mu \sim \hbar\omega_\perp$. Throughout this thesis we hence use the following approximate scheme:

- In the limit $\mu < \hbar\omega_\perp$ studied in [118], it was found sufficiently accurate to use [60, 175]:
$$\mu_j(z) = \mu - V(z) - j\hbar\omega_\perp. \tag{3.30}$$
The transverse thermal atoms are therefore treated as independent 1D ideal Bose gases. This approach is adopted in Chapter 4, where we model the density profiles and density fluctuations of the experiments of Refs. [59–61]

- In the regime $\mu \sim$ few $\hbar\omega_\perp$, with $\mu > \hbar\omega_\perp$, studied subsequently [119], it was found to be essential to account for the effect of mean-field potential experienced by the transverse thermal atoms. This is characteristic of the experiments of Refs. [54, 95] studied in Chapters 5-6, for which we instead use the full expression:
$$\mu_j(z) = \mu - V(z) - j\hbar\omega_\perp - 2g_{\rm 1d}(\langle|\psi(z)|^2\rangle + n_\perp(z)). \tag{3.31}$$

Regardless of the level of approximation used, we note that within this approach, the thermal atoms above the numerical energy cut-off (i.e. with energies $> \hbar\omega_\perp$) experience the true mean-field potential due to all atoms in the trap. However because we expect the contribution of $n_\perp(z; \mu, T)$ not to significantly affect the axial modes (due to the relatively lower density of these high energy atoms), we do not include the mean-field contribution due to these atoms within the nonlinearity of the SGPE in Eq. (3.28) (see Ref. [164] for a 'quantitative' justification for doing so). We emphasise, that interaction effects due to all atoms (i.e. condensate and thermal) within the axial modes beneath the energy cut-off are fully accounted for within the nonlinearity of the SGPE.

The total density, corresponding to transversely integrated density profiles, typical of ultracold gas experiments is ultimately given by

$$n(z;\mu,T) = \langle|\psi(z;\mu,T)|^2\rangle + n_\perp(z;\mu,T), \tag{3.32}$$

where $\langle\cdots\rangle$ denote ensemble averaging, obtained by averaging over many different realizations of the noise in Eq. (3.28).

3.3.3 Numerical procedure

A typical numerical simulation implementing the modified one-dimensional stochastic GPE of Eq. (3.28) together with Eq. (3.29) for the transverse modes, generally requires a certain number of steps. In this section we provide details of the numerical procedure that needs to be applied in order to reproduce the equilibrium configurations obtained in the experiments analysed in Part III of this thesis.

For each of the 5 experiments analysed in Part III of this thesis, we initially set the following parameters as input in the numerical simulations:

1. Mass, m, and scattering length, a_s, of the atomic species used in the experiment, i.e. $^{87}\mathrm{Rb}$ ($m = 1.44\times10^{-25}\,\mathrm{Kg}$ and $a_\mathrm{s} = 5.05\,n\mathrm{m}$).
2. Trap configuration, i.e. axial (ω_z) and radial ($\omega_\perp$) frequencies.
3. Temperature, T, of the gas at equilibrium.

We stress that the above are the only input parameters from the experiments, and that every other observable is calculated *ab initio*, as will be explained in more detail in Part III.

Subsequently, we need to find the exact numerical value of the chemical potential, μ, such that the *total number of atoms*[3], obtained by integrating the density in Eq. (3.32), matches the experimental one. Notice that the contributions to the density arise from solving Eqs. (3.28)–(3.29) for the axial and transverse modes respectively. Therefore we proceed as follows:

1. We initially choose a value for the chemical potential and we solve the quasi-one-dimensional SGPE (Eq. (3.28)), to generate an axial density profile (appropriately averaged over the noise realizations).

---

[3] Notice that for the experiment by Richard *et al.* [54], we match the experimental *quasi-condensate* atom number instead (see Section 5.2 for details).

2. We then solve Eq. (3.29), to obtain the density of the transverse thermal atoms.

We iterate the above procedure until a suitable value for the chemical potential is found. As in most cases discussed in this thesis, the ratio of the chemical potential to the transverse excitation energy is already given in the experiment, thus implying that we know which approximation (Eq. (3.30) or Eq. (3.31)) to use from the outset. We point out that solving Eq. (3.28) before Eq. (3.29) is a necessary requirement if $\mu > \hbar\omega_\perp$, as the axial density feeds into Eq. (3.29) through the expression of μ_j (Eq. (3.31)).

3.4 Growth to dynamical equilibrium

The equilibrium configuration obtained by numerically solving Eqs. (3.28)–(3.29), is characterised by a dynamical contribution of the axial modes, and a static contribution of the transverse excited modes. In this section we focus on the process that leads the axial modes to equilibration, hence we consider only Eq. (3.28). The wavefunction ψ, associated with the low-energy axial modes in the system, is initially zero (i.e. $\psi(z, t = 0) = 0$). The growth process is initiated by the noise term η, which seeds the population of the low-energy axial modes (described by ψ) in a random way, but is generally characterised by a prescribed initial shape based on the Keldysh self-energy. The axial modes then evolve according to Eq. (3.28).

A visual representation of the growth process is given in Figure 3.1: here we show snapshots of the averaged density profiles at different times during the equilibration. The initial small amplitude distribution (red, solid) evolves to the final distribution at equilibrium (black, dashed), which takes the form of an inverted parabola around the centre of the trap, as expected, due to the presence of the harmonic potential. The equilibrium generated via growth is attained when the number of particles reaches a constant value, determined by the set of parameters chosen, as shown in Figure 3.2; given that this is a dynamical equilibrium, the number of particles exhibits fluctuations around an equilibrium value, and the actual value about which fluctuations arise also varies slightly from numerical run to run. The slope of the curve shown in Figure 3.2 is indirectly determined by γ, which sets the rate of collisions in the gas: the higher (lower) is γ, the faster (slower) the gas relaxes to equilibrium. As pointed out in Section 3.1.3, we use a constant value of γ through Eq. (3.15): although this is an approximation, we have numerically confirmed that a spatial dependent γ does not affect the equilibrium configuration [165, 167], unlike the case for any dynamical studies. For the pur-

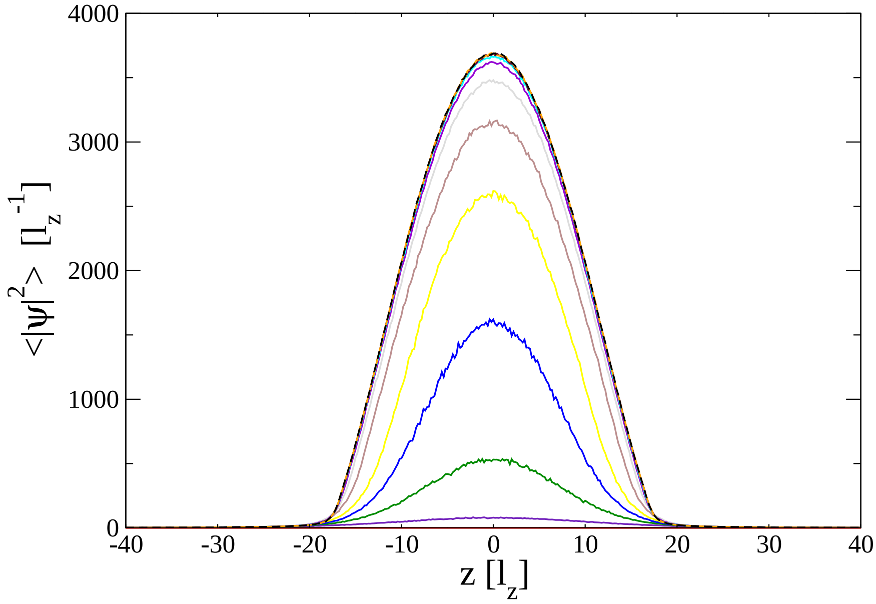

Figure 3.1: Dynamical growth to equilibrium: snapshots of averaged density profiles taken at different times during evolution. The dashed black curve corresponds to the equilibrium configuration. The trap parameters are taken from the experiment of Hugbart *et al.* [95] (discussed further in Chapter 6), and correspond to $\omega_z = 2\pi \times 8.67\,\mathrm{Hz}$, $\omega_\perp = 2\pi \times 395\,\mathrm{Hz}$, $\mu = 165\,\hbar\omega_z$ and $T = 116$ nK.

pose of this work, focused only on the investigations of properties at equilibrium, Eq. (3.15) is therefore a sufficient approximation.

As mentioned in [117], the process shown in Figure 3.1 describes the first stage of the experiment by Stamper-Kurn *et al.* [153], where a three-dimensional Bose gas is initially confined in a cigar-shaped harmonic trap, with frequencies ω_z and ω_r, at a temperature just above the critical one; subsequently a dimple is created in the external potential, with frequencies ω_z and $\omega_\perp$, that contains only one energy level along the transverse direction.

The depth of the dimple can be lowered to the point where the only energy level becomes lower than the chemical potential μ of the noncondensed cloud: under this condition the atoms condense into the transverse ground state of the dimple. During the formation of the condensate, the noncondensed part of the gas remain sufficiently close to equilibrium, acting as a reservoir of particles for the atoms in the dimple.

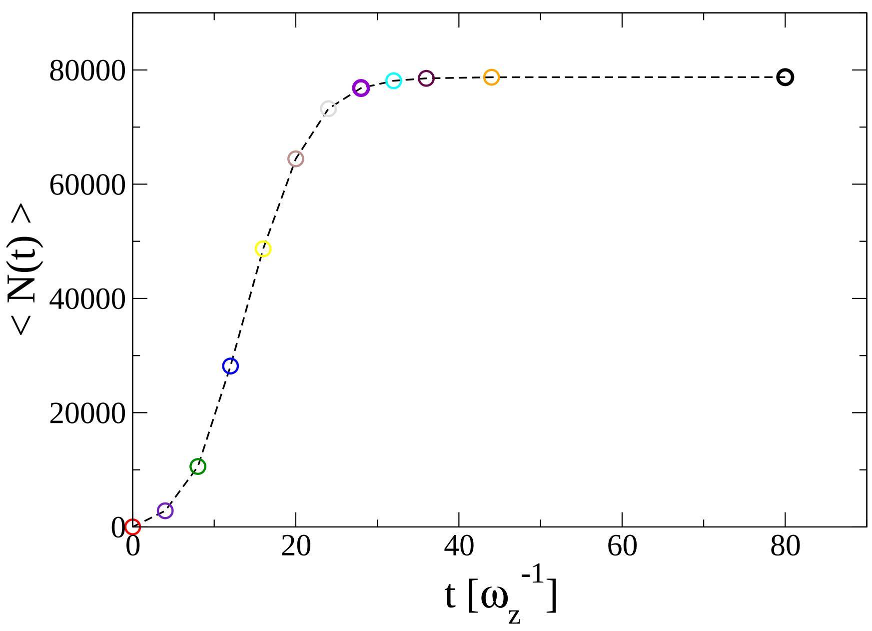

Figure 3.2: Average atom number vs time. The value of γ is approximately 6×10^{-3}. Same parameters as in Fig. 3.1.

3.5 Density profiles

In typical experiments with ultracold Bose gases, similar to those analysed in Part III of this thesis, the results are generally obtained by repeating the same experimental conditions several times, and then averaging over the single measurements. Similarly, one single run of our numerical SGPE model can be loosely associated to a single experimental realization, in the sense of eventually extracting results after averaging. In Figure 3.3 we show a comparison at equilibrium, between the axial density ($\langle|\psi|^2\rangle$, dashed black) and a single run profile ($|\psi|^2$, solid orange), obtained by solving Eq. (3.28). As expected, the single run density profile is very noisy compared to the much smoother averaged one, obtained by performing an average over 1200 numerical realizations of the noise. Typically, a large number of stochastic trajectories (i.e. number of numerical runs), are required to obtain such a smooth profile (this is more crucial in low dimensions due to the enhanced amplitude and role of fluctuations). Nonetheless, a lot of physics relevant to experiments is captured within one single run; it will be shown in Chapter 4 that for example, information on density fluctuations are accessible only through an analysis of atom number fluctuations based on multiple

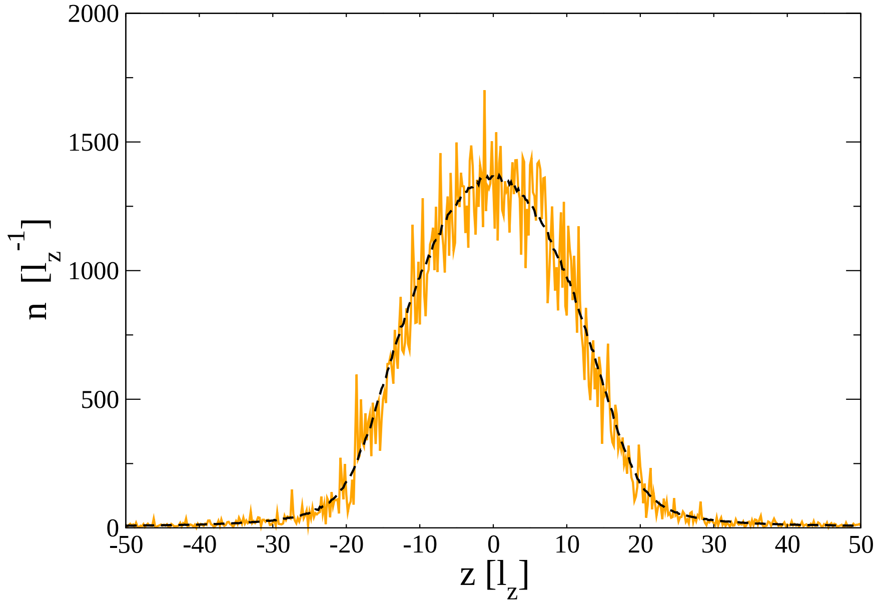

Figure 3.3: Density profiles obtained from Eq. (3.28): Comparison between single run (solid, orange) and averaged (dashed, black) density profile. Parameters are taken from experiment by Richard *et al.* [54]: $\omega_\perp = 2\pi \times 760$ Hz, $\omega_z = 2\pi \times 5$ Hz, $T = 345\ n$K. The numerical chemical potential is $\mu = 243\,\hbar\omega_z$.

individual runs.

It is worthwhile mentioning that the set of parameters used to generate the density profile in Figure 3.3 are taken from the experiment of Richard *et al.* [54], whose experimental findings we model in Chapter 5.

We also highlight the fundamental role of the nonlinearity in Eq. (3.28), which makes the quasi-one-dimensional version of the SGPE more suitable to the implementation of typical experimental conditions. This can be demonstrated by estimating the value of $4a_\mathrm{s}\langle|\psi|^2\rangle$, appearing in Eq. (3.28), at the trap centre; the values of the density in the central region of the trap ($\sim 10^3[l_z^{-1}]$, with $l_z = 3.7\,\mu m$) and of the scattering length ($a_\mathrm{s} \approx 5\,nm$), yield $4a_\mathrm{s}\langle|\psi|^2\rangle \approx 5$, hence this term is not negligible, and the simpler one-dimensional SGPE would be inappropriate in this case (see Section 3.3.1 for further details).

The density profiles shown in Figure 3.3 represent the contribution from the low-energy axial modes; however, as already discussed in Section 3.3, the model used in Part III also incorporates the contribution of the transverse excited modes with energy $k_B T \sim$ few $\hbar\omega_\perp$ via Eq. (3.29). In Figure 3.4 we show a comparison between the density profile (dashed black) obtained from Eq. (3.28) alone and the corresponding profile (red solid) which also incorporates the density from Eq. (3.29). Note that the latter corresponds to transversely integrated density profiles as relevant in experiments based on imaging. We notice that taking into account the presence of the atoms in the transverse excited modes mainly affects the wings of the density distribution, where the highly energetic atoms reside. As visible in Figure 3.4, the inclusion of the transverse thermal atoms result in an increase of the density in the outer region of the trap, compared to the contribution of the axial thermal wings. Moreover, the tails of the transversely integrated density distribution decay exponentially, a feature that is not present in the axial distribution, where the density of thermal atoms decays algebraically, because of the classical approximation discussed in Section 3.1 and in [115, 117].

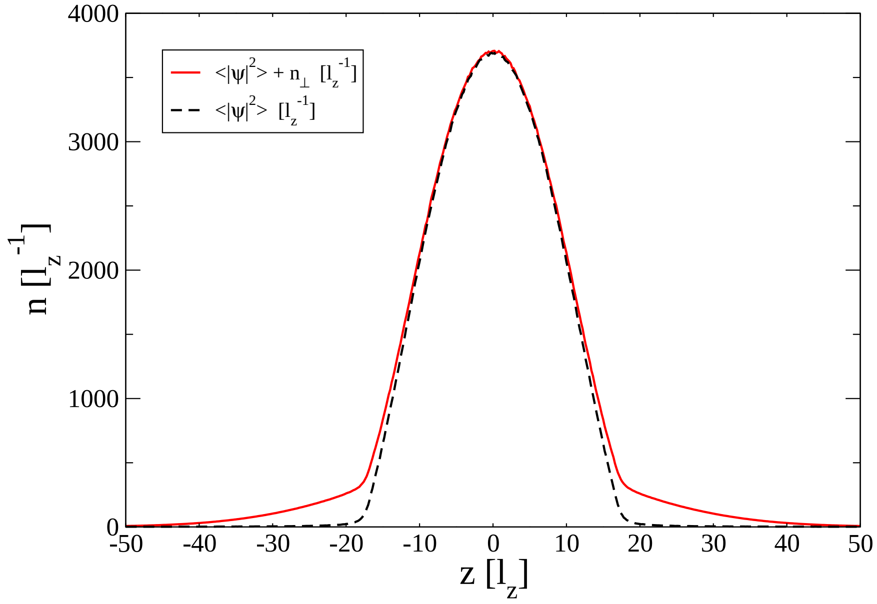

Figure 3.4: Comparison between axial (dashed, black) and axial plus transverse thermal cloud (solid, red) density profiles, the latter corresponding to total transversely integrated profiles. Same parameters as in Fig. 3.3.

3.6 Correlation functions

Reducing the dimensionality of a system can have dramatic consequences on its coherence; fluctuations are in fact much more pronounced than in the 3D counterpart - where they are important only in a very narrow range around the critical temperature [176] - and tend to destroy the long range order in the system. An accurate analysis of the coherence properties in such systems is therefore necessary for potential applications, such as matter-wave interferometry [67, 68, 77, 105, 106, 177, 178], atom chips [179] and atom lasers [35, 107–110].

The SGPE model in this respect is well suited to such a study, since the fluctuations are retained within ψ, and we can therefore access the information about coherence by studying the auto-correlation functions, first introduced by Glauber [180]. Usually the lowest order correlation function is already sufficent to obtain important information on the coherence properties of the system. An in-depth numerical study of the three lowest order correlation functions, in equilibrium one-dimensional Bose gases, by means of the Stochastic GPE is reported in [156]; these observables can also be explored experimentally, as demonstrated in [53, 58, 61, 63, 103].

In this work we focus on the study of systems at equilibrium; as a consequence we are only interested in equal time auto-correlation functions. We therefore firstly let the system evolve for a sufficient time to reach equilibirum, and then we compute the auto-correlation functions.

3.6.1 First-order correlation function

In the Chapters 5-6 we investigate the phase coherence properties of quasi-one-dimensional Bose gases; the information about the phase coherence of the system is accessible through the first order correlation function, which we here define in its symmetrical form, normalised to the central density:

$$g^{(1)}(-z/2, z/2) = \frac{\langle \psi^*(-z/2)\psi(z/2)\rangle}{.}\langle|\psi(0)|^2\rangle \tag{3.33}$$

This function is referred to, in the condensed matter literature, as the off-diagonal one-body density matrix, and gives information on the correlation between pairs of points in the system separated by a distance z. There also exist other forms for the first order correlation function: for example it can be defined in asymmetrical form, or it can be normalized to the densities in each spatial point. A comparison between the symmetrical and asymmetrical first order correlation function in 1D can be found in [156]. Here we use the definition given in Eq. (3.33), as this is relevant for the experiments of Refs. [54, 95] analysed in Chapters 5-6. Each state of matter is characterized by a definite type of correlation between particles: for example the solid state features a diagonal long-range order, because of the periodicity in the atomic density [181]. In a classical gas

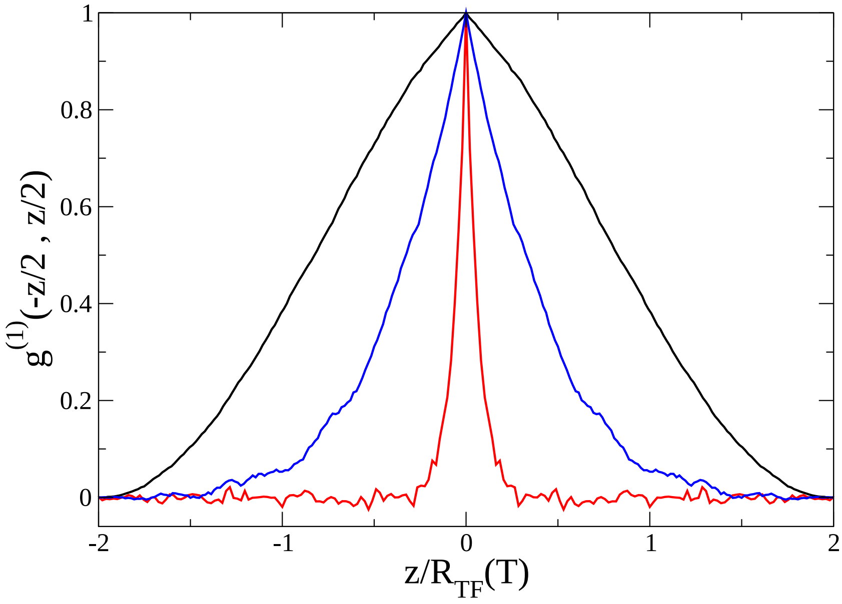

Figure 3.5: Spatial dependence of the first-order symmetrical correlation functions (normalized to the central peak density) at $T/T_\phi = 0.8$ (black), $T/T_\phi = 4.2$ (blue), and $T/T_\phi = 24.9$ (red). The axial coordinate z is scaled to the temperature dependent Thomas-Fermi radius $R_{\mathrm{TF}}(T)$. Parameters are taken from the experiments of Hugbart *et al.* [95] ($T/T_\phi = 0.8$ and $T/T_\phi = 4.2$) and from Richard *et al.* [54] ($T/T_\phi = 24.9$).

the first order correlation function decays to zero on a distance which is of the order of the de Broglie wavelength (see, e.g. [182]). In a three-dimensional Bose gas below the degeneracy temperature the off-diagonal long-range order is the signature of the Bose-Einstein condensation, therefore the first-order correlation function is expected to be non-zero across the entire sample. In low-dimensional homogeneous Bose gases instead, the Bose-Einstein condensation does not occur (except at $T = 0$ in 2D) [27, 28].

If the system is confined in a trap, at sufficiently low T (such that $T \sim T_\phi$), the first-order correlation function $g^{(1)}$ is found to decay to zero within the system size, at a slower rate compared to the classical gas case. Figure 3.5 shows a comparison between first-order correlation functions for three different temperatures. At $T/T_\phi = 24.9$ (red), the correlation function decays exponentially within the system size. At $T/T_\phi = 4.2$ (blue), the coherence increases, but the correlation function still shows an exponential behaviour; at $T/T_\phi = 0.8$ (black) instead the gas shows a large amount of phase coherence, revealed by a Gaussian-like behaviour of the correlation function, which decays to zero only at the edges of the system. The variation of the correlation function from exponential to Gaussian indicates the crossover from quasi-condensation to "true" condensation [31, 64, 156]. In Figure 3.5 the spatial coordinate z is scaled to the half-size of the quasi-condensate, given by the temperature dependent Thomas-Fermi radius, $R_{TF}(T)$ (see Section 3.7.2 for details), which takes on a different value in each of the three cases analyzed. Notice that the correlation function for the lowest temperature case goes to zero at $z = \pm 2R_{TF}(T)$; this is because we compute $g^{(1)}(-z/2, z/2)$ as opposed to $g^{(1)}(-z, z)$, in which case it would go to zero at $z = R_{TF}(T)$.

3.6.2 Second-order correlation function

The second-order correlation function gives information about density coherence in the system, and can be computed through the following expression:

$$g^{(2)}(z) = \frac{\langle|\psi(z)|^4\rangle}{(\langle|\psi|^2\rangle)^2}. \tag{3.34}$$

This is also called the density-density correlation function and gives information on the probability of finding two particles at the same spatial point. The second order correlation function tends to the value of one ($g^{(2)}(z) \to 1$) if the density fluctuations are suppressed; the system is then said to be a quasi-condensate. For a density incoherent system instead, where density flucuations are large, $g^{(2)}(z) \to 2$. It is in fact well established that for a system where a single mode dominates, $g^{(2)} = 1$, whereas for a multimode incoherent field $g^{(2)} = 2$ [183, 184].

In Figure 3.6 we plot the second order correlation function of a degenerate Bose gas, confined in harmonic trap, at temperatures $T/T_\phi = 0.8$ (black), $T/T_\phi = 4.2$ (blue) and $T/T_\phi = 24.9$ (red). The spatial coordinate z is scaled to the temperature dependent Thomas-Fermi radius, $R_{TF}(T)$ (see Section 3.7.2 for details), which actually differs slightly for each of the cases analysed.

For the lower temperature case ($T < T_\phi$) the system is fully density coherent ($g^{(2)} = 1$) within the quasi-condensate size, which is given by the temperature dependent Thomas-Fermi radius, $R_{TF}(T)$ (see Section 3.7.2 for details); at the edges instead it becomes incoherent as $g^{(2)} = 2$. For the intermediate temperature case (solid blue), the density coherence is reduced with respect to the previous case, but it still extends over a large part of the system. For the higher temperature case (solid red), the system is not fully density coherent, as the correlation function is slightly greater than one ($g^{(2)} \gtrsim 1$), even at the centre of the trap. We also notice that the crossover to the incoherent region is quantitatively different in the two extreme temperature cases, as $g^{(2)}$ changes smoothly for $T/T_\phi = 24.9$, while

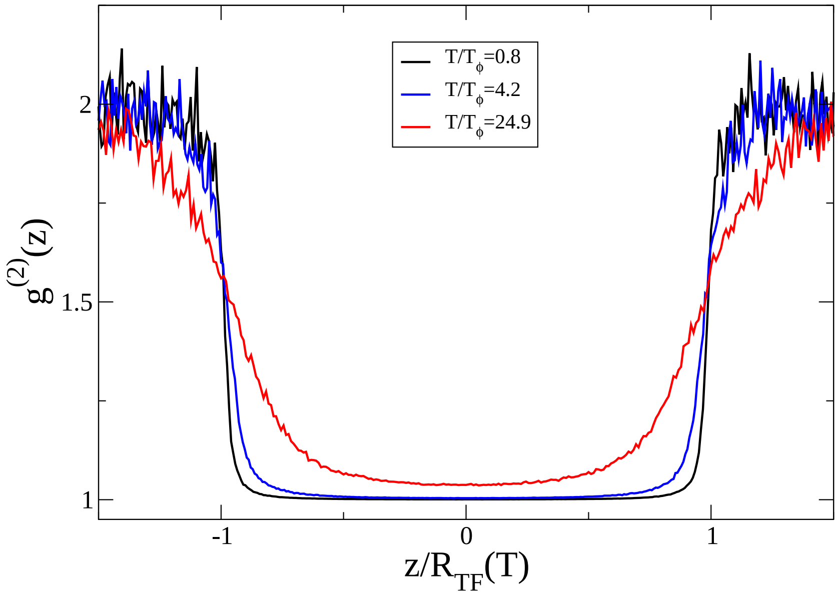

Figure 3.6: Density correlation function $g^{(2)}(z)$ [Eq. (3.34)] from SGPE simulations, at $T/T_\phi = 0.8$ (solid black), $T/T_\phi = 4.2$ (solid blue) and $T/T_\phi = 24.9$ (solid red). The spatial coordinate z is scaled to the temperature dependent Thomas-Fermi radius, $R_{\mathrm{TF}}(T)$. Same parameters as in Fig. 3.5

it exhibits a very steep jump for $T/T_\phi = 0.8$.

3.7 Density and phase coherent part

The quasi-1D stochastic Gross-Pitaevskii equation (Eq. (3.28)) provides the atomic density profile $|\psi(z)|^2$ along the axial direction; as already discussed before, $|\psi(z)|^2$ represents a set of low-lying highly populated modes up to a predetermined cut-of (and in general higher-lying modes should also be considered for the total density). However the SGPE density distribution contains all coherent and a large part of the incoherent density in the system (up to the cut-off), and so a method to identify the coherent component within $|\psi(z)|^2$ is required. This is analogous to what is typically done in experiments with degenerate Bose gases, where the experimental measurement of the total density profile includes all atoms, while the coherent fraction is extracted *a posteriori* (e.g. by bimodal fit).

We now discuss different means that can be used to extract the coherent component of $|\psi(z)|^2$, and contrast their different physical interpretations.

3.7.1 Quasi-condensate density

The quasi-condensate is the density-coherent part of $|\psi|^2$; unlike other theories (e.g. modified Popov [97]) where the separation between quasi-condensate and thermal component is done explicitly at the beginning, for the SGPE (and related classical field theories) it is necessary to extract the quasi-condensate *a posteriori*, via the following formula:

$$n_{\rm qc}(z) = \sqrt{2\langle|\psi(z)|^2\rangle^2 - \langle|\psi(z)|^4\rangle}. \tag{3.35}$$

Such a definition had been already put forward by Prokofev *et al.* [185], in the case of a two-dimensional weakly interacting Bose gas, and it has been used in the context of the SGPE model in [156, 167, 186] and classical field methods [187]. In particular, see Ref. [156] for a brief review of its physical origin and a corresponding illustration for the SGPE.

In Figure 3.7 we compare the quasi-condensate (Eq. (3.35)) to the axial (Eq. (3.28)) density profiles at three different temperatures. For $T/T_\phi = 0.8$ (Figure 3.7 left), the axial density profile (solid black), closely matches the quasi-condensate density (dashed red), thus suggesting that the density coherence extends throughout the whole system, represented by $|\psi(z)|^2$. This is in agreement with the behaviour of the second order correlation function, analyzed in Figure 3.6 , for the same temperature case. At relatively high temperature ($T/T_\phi = 24.9$, Figure 3.7 central), most of the atoms reside in the quasi-condensate, but the density coherence does not extend over the whole sample, given that the tails of the quasi-condensate distribution (dashed red) decay faster to zero. For the highest temperature case ($T/T_\phi \sim 40$, Figure 3.7 right) far less of the system atoms are in the quasi-condensate (dashed red) density, which is further distinguished from the axial profile (solid black), than the lower temperature case. In this (high temperature) case, it is more meaningful to compare the value of the temperature to $T_{\rm qc}$ of Eq. (1.14), which roughly indicates the crossover to the quasi-condensate regime. We find that $T \approx 0.7T_{\rm qc}$, as opposed to the other lower temperature cases in Fig. 3.7 where $T \ll T_{\rm qc}$.

3.7.2 Identifying the size of the quasi-condensate

In some of the plots shown in this chapter, we scale the axial coordinate, z, to the so-called temperature dependent Thomas-Fermi radius, $R_{\rm TF}(T)$, which identifies the extent of the quasi-condensate in our model. By scaling correlation functions, density profiles, and coherence lengths to the effective size of the quasi-

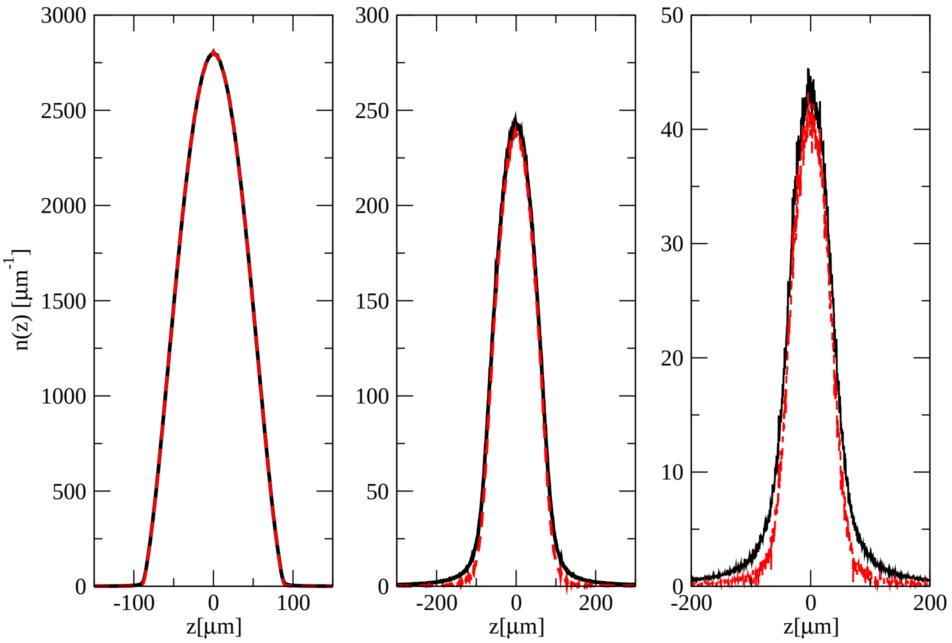

Figure 3.7: Comparison between axial density distributions (solid black, Eq. (3.28)) and quasi-condensate profile (dashed red, Eq. (3.35)) at $T/T_\phi = 0.8$ (left), $T/T_\phi = 24.9$ (central) and $T/T_\phi \sim 40$ (right). Three different trap configurations were used, taken from: Hugbart *et al.* [95] $\omega_z = 2\pi \times 8.67\,\mathrm{Hz}$ and $\omega_\perp = 2\pi \times 395\,\mathrm{Hz}$ (left), Richard *et al.* [54] $\omega_z = 2\pi \times 5\,\mathrm{Hz}$ and $\omega_\perp = 2\pi \times 760\,\mathrm{Hz}$ (central), van Amerongen *et al.* [60] $\omega_z = 2\pi \times 8.5\,\mathrm{Hz}$ and $\omega_\perp = 2\pi \times 3280\,\mathrm{Hz}$ (right).

condensate gives an idea of the behaviour of these observables relative to the particular system under investigation. This scaling is also performed in the experiments, in which case the size of the quasi-condensate is typically identified via bimodal fits. Unlike this parameter, the temperature dependent Thomas-Fermi radius accounts instead for finite temperature effects, as it results smaller for increasing temperatures, due to quasi-condensate depletion.

In previous works (see e.g. [88, 156, 186]) the extent of the quasi-condensate within the SGPE model was obtained by also independently solving the modified Popov theory of Andersen *et al.* [90, 97] in parallel for the same paramaters, since a well defined criterion exists for identifying the quasi-condensate in modified Popov. Such an approach is supported by the excellent agreement between the density profiles extracted within the SGPE model and the modified Popov theory, as demonstrated in [167]. However the aim in this work is to make the SGPE fully self-consistent, with all the necessary parameters calculated *ab initio* within SGPE. We therefore calculate the size of the quasi-codensate (in a somewhat heuristic manner) by extending the modified Popov criterion to our SGPE model, in the way we explain below.

We recall that in order to find the quasi-condensate density within the modified Popov theory, one has to solve Eq. (2.31) (see also [90, 167].

However, for the purpose of only extracting the size of the quasi-condensate, one can use the Thomas-Fermi approximation, that neglects the kinetic term, and Eq. (2.31) is recast (in 1D) as:

$$[V(z) - \mu + g_{1\mathrm{d}}(n_0 + 2n')]\sqrt{n_0} = 0, \tag{3.36}$$

where n_0 is the quasi-condensate density and n' is the thermal part (i.e. quasi-condensate depletion).

We now wish to extend Eq. (3.36) to the quasi-one-dimensional case, in analogy to the approach used for the GPE and SGPE, as discussed in Sections 3.2-3.3.1. In the quasi-one-dimensional limit, Eq. (3.36) takes the following form:

$$\big[V(z) - \mu + \hbar\omega_\perp\big(\sqrt{1 + 4a_\mathrm{s}(n_0 + 2n')} - 1\big)\big]\sqrt{n_0} = 0. \tag{3.37}$$

We point out that the above expression is heuristic, and actually relies on a somewhat crude approximation $\langle|\psi|^2\rangle \approx n_0 + 2n'$; the latter makes a distinction between density-coherent quasi-condensate (prefactor of 1) and incoherent thermal (prefactor of 2, as usual for thermal contribution due to direct and exchange terms) and is further supported by the excellent agreement between the SGPE and the modified Popov theory [167]. One could however argue that an alternative form to Eq. (3.37) is also plausible, in which the quasi-one-dimensional character is reflected only on the quasi-condensate n_0, yielding:

$$\big[V(z) - \mu + \hbar\omega_\perp\big(\sqrt{1 + 4a_\mathrm{s}n_0} - 1\big) + 2g_{1\mathrm{d}}n'\big]\sqrt{n_0} = 0. \tag{3.38}$$

While the correct form remains an open issue here, we decided to opt for the form of Eq. (3.37), as this is also consistent with the identification between the densities in the SGPE and modified Popov theory. However, we point out that the resulting values of the temperature dependent Thomas-Fermi radius are not noticeably affected by the particular form chosen, at least for the data of the experiments analysed in Chapters 5-6 of this thesis. We find in fact that the values of the Thomas-Fermi radius — calculated assuming Eq. (3.38) holds — result smaller only in 4 (out of 35) cases (for the data set in the experiments of Refs.[54, 95] analysed in Chapters 5-6), and the percentage difference compared to the values obtained assuming that Eq. (3.37) holds instead, is less than 1%.

The Thomas-Fermi radius is then identified as the spatial point, z, at which the quasi-condensate density becomes zero:

$$\mu - V(z) = \hbar\omega_\perp[\sqrt{1 + 8a_s n'(z)} - 1]. \tag{3.39}$$

Near the centre of the trap the left hand side (LHS) in the above equation is greater than the right hand side (RHS), as $V(z)$ and $n'(z)$ are small. Towards the outer region of the trap however the LHS (RHS) tends to smaller (higher) values, as $V(z)$ and $n'(z)$ increase with increasing z. Given the discrete nature of the spatial grid in a typical numerical simulation, it is unlikely that there exists a spatial point z at which Eq. (3.39) is precisely fulfilled. We therefore numerically implement the criterion to find $R_{\mathrm{TF}}(T)$ by seeking for the *largest* value of z within our simulated grid, at which the LHS in Eq. (3.39) is greater than or equal to the RHS:

$$R_{\mathrm{TF}}(T) = max\{z,\, \mu - V(z) \geq \hbar\omega_\perp[\sqrt{1 + 8a_s n'(z)} - 1]\}, \tag{3.40}$$

where $\mu_{3\mathrm{d}} = \mu + \hbar\omega_\perp$ (with μ denoting the effective one-dimensional chemical potential).

In order to extend and apply the criterion of Eq. (3.40) within the SGPE model, we approximate the quasi-condensate depletion (n') within the modified Popov theory, with the density of the thermal atoms (below the energy cut-off) in the SGPE:

$$n' \approx \langle|\psi(z)|^2\rangle - n_{\mathrm{qc}}(z). \tag{3.41}$$

The condition to find the Thomas-Fermi radius within the SGPE model then reads:

$$R_{\mathrm{TF}}(T) = max\{z,\, \mu - V(z) \geq \hbar\omega_\perp[\sqrt{1 + 8a_s(\langle|\psi|^2\rangle - n_{\mathrm{qc}})} - 1]\}. \tag{3.42}$$

The above criterion will be used in Chapters 5-6, in which we investigate the experiments by Richard *et al.* [54] and Hugbart *et al.* [95].

3.7.3 Penrose-Onsager mode and approximate determination via correlation functions

We identify the 'true' (phase) coherent part of the field ψ by adopting the Penrose-Onsager (PO) criterion [135] (see also e.g. Refs. [187, 188]), which states that Bose-Einstein condensation occurs when an eigenvalue of the one-body density matrix takes on a macroscopic value (of the order of the total number of particles in the system).

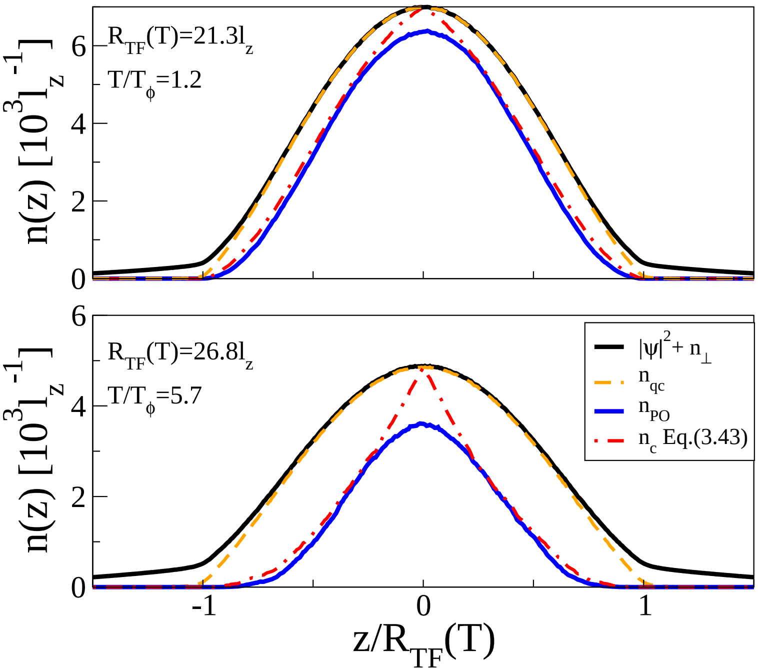

Figure 3.8: Density profiles from SGPE numerical simulations, for two experimental cases (corresponding to points with error bars in Figure 6.4). Black, solid line: total transversely integrated density profile (Eq. 3.32). Dashed, orange: quasi-condensate. Blue, solid: Penrose-Onsager density. Red, dot-dashed: condensate density from Eq. (3.43). Parameters are taken from experiment of Hugbart *et al.* [95]: (top) $\omega_z = 2\pi \times 8.67\,\text{Hz}$, $\omega_\perp = 2\pi \times 395\,\text{Hz}$, $l_z = 3.7\mu\text{m}$, $\mu = 241\,\hbar\omega_z$; (bottom) $\omega_z = 2\pi \times 6.55\,\text{Hz}$, $\omega_\perp = 2\pi \times 655\,\text{Hz}$, $l_z = 4.2\mu\text{m}$, $\mu = 393\,\hbar\omega_z$

In the SGPE model we extract the Penrose-Onsager mode by numerically diagonalizing the one-body density matrix $\rho(z,z') = \langle\psi^*(z)\psi(z')\rangle$, and identifying the condensate mode as the one corresponding to the largest eigenvalue [135, 187, 188]. An alternative way to obtain an estimate of the phase coherent part of ψ is to combine the notion of first and second order correlation functions as follows [167]:

$$n_c(z) = \langle|\psi|^2\rangle\sqrt{2 - g^{(2)}(z)}\, g^{(1)}(0, z). \tag{3.43}$$

This expression was found to agree well with the PO condensate at large $|z|$ in Cockburn *et al.* [167] for a range of temperatures. Notice that the Penrose-Onsager criterion is strictly valid in the limit $|z - z'| \to \infty$. Eq. (3.43) arises as an adaptation to the trapped case, of the definition given for an homogeneous system by Al Khawaja *et al.* [90]. We believe that Eq. (3.43) provides also a useful experimental tool to extract the coherent part from the density profile, as it only requires the simultaneous knowledge of first- and second- order correlation functions (in addition to density profiles), all of which are experimentally accessible.

Figure 3.8 shows density profiles obtained within the SGPE model, for two experimental data sets from the experiment of Hugbart *et al.* [95]. It is worth to highlight the clear distinction between the quasi-condensate (orange, dashed) and PO condensate (blue, solid); the difference is already noticeable at low temperature ($T = 1.22T_\phi$), and becomes bigger at relatively high temperature ($T = 5.73T_\phi$), where the phase coherence is much more reduced compared to the density coherence.

We also notice the excellent agreement (in particular at large $|z|$) between the PO density (blue, solid) calculated via diagonalisation of the one-body density matrix, and Eq. (3.43) (red, dot-dashed). In the central region of the trap instead, the density distribution of the condensate (calculated via Eq. (3.43)) shows a 'spike', due to the fact that at $z = 0$, one has necessarily $g^{(1)}(0) = 1$ and as a consequence $n'_{\rm c}(0) = n_{\rm qc}(0)$, whereas by diagonalising the one-body density matrix, one finds that $n_{\rm PO}(0) < n_{\rm qc}(0)$. In the numerical simulations this can be theoretically cured (see Ref. [167]), but such modification cannot be directly related to experimental observables and will thus not be considered any further here.

3.8 Chapter summary

In this chapter we have initially summarised key considerations in the derivation of the stochastic Gross-Pitaevskii equation (SGPE), through a mapping of the Fokker-Planck equation onto a non-linear stochastic differential equation. By showing how to obtain an effective 1D mean-field equation, suitable for the dynamics of cigar-shaped condensate at $T = 0$, in the regime $\mu \sim \hbar\omega_\perp$, we subsequently extended this result to the SGPE; this led, in a somewhat heuristical manner to the quasi-one-dimensional SGPE, which is suitable to describe the highly populated low-lying axial modes, while also self-consistently incorporating the contribution from transverse degrees of freedom. The transverse excited modes with thermal energy $k_{\rm B}T \gtrsim \hbar\omega_\perp$ are instead treated in a static manner, as 1D independent Bose gases. The quasi-one-dimensional SGPE and the equation for the transverse excited modes provide a self-consistent *ab initio* model for reproducing physical observables of quasi-one-dimensional experiments. We have then explained the detailed numerical approach we undertake when comparing our model to the experiments, and given some example of observables calculated at equilibrium, such as density profiles and correlation functions up to the second order, and how such observables may be observed. Importantly, the parameters used for these calculations are taken from the experiments we model in Part III. We have finally discussed how to extract the quasi-condensate (i.e. density coherent part) and the 'pure' condensate (based on the Penrose-Onsager criterion) from the total density distribution in our simulations, also proposing an alternative approximate form for obtaining the Penrose-Onsager condensate mode.

Part III

Quantitative *ab initio* comparison to quasi-1d experiments

Part III is divided into three chapters, discussing the main achievements of our work.

In the first chapter we reproduce the in situ density profiles obtained in the experiments of Trebbia et al. [Phys. Rev. Lett. **97***, 250403 (2006)] and van Amerongen et al. [Phys. Rev. Lett.* **100***, 090402 (2008)], and the density fluctuation data reported by Armijo et al. [Phys. Rev. Lett.* **105***, 230402 (2010)]. The above results are presented in the joint work by S. P. Cockburn, D. Gallucci and N. P. Proukakis [Phys. Rev. A* **84** *, 023613 (2011)], with numerical simulations undertaken by S. P. Cockburn.*

In the second and third chapter we perform an ab initio analysis of the temperature dependence of the phase coherence length of finite temperature quasi-one-dimensional Bose gases measured in the experiments of Richard et al. [Phys. Rev. Lett. **91***, 010405 (2003)] and Hugbart et al. [Eur. Phys. J. D* **35***, 155 (2005)] respectively. The above results are presented in the work by D. Gallucci, S. P. Cockburn and N. P. Proukakis [Phys. Rev. A* **86***, 013627 (2012)].*

Chapter 4

In situ density profiles and density fluctuations: *Ab initio* experimental modelling

In this chapter, we show that the model described in Part II provides an accurate *ab initio* prediction of the *in situ* density profiles and density fluctuations measured in the weakly-interacting, elongated Bose gas experiments of Trebbia *et al.* [59], van Amerongen *et al.* [60], and Armijo *et al.* [61]. For each of these experiments we initially give a general description of the experimental procedure and the theory used to analyse the experimental findings, before comparing these to our numerical results.

We begin with a quantitative comparison between our method and the experiments by Trebbia *et al.* [59] and van Amerongen *et al.* [60] in Section 4.1.1 and 4.1.2 respectively; in these experiments several measurements of density profiles of finite-temperature quasi-1D Bose gases realised on atom chips, were obtained by *in situ* absorption imaging. We further test our model in Section 4.2, by directly comparing to the density fluctuations measurements from the experiment of Armijo *et al.* [61].

We emphasise that in order to reproduce the experimental results, the only experimental parameters used as input to the theory are the temperature of the gas at equilibrium, the atomic species and the trap configuration, whereas every other physical observable is calculated *ab initio* in our model.

4.1 Density profiles: comparison to experiments

We briefly review the numerical approach we use to match to the experimental density profiles in the works of Trebbia *et al.* [59] and van Amerongen *et al.* [60]. Our method is based on solving the quasi-1D form of the SGPE (Eq. 3.28) together with the equation for the tranverse thermal modes (Eq. 3.29). Importantly, as the parameter regime of these two experiments is such that $\mu < \hbar\omega_\perp$ (see Figure 1.1), we treat the transverse excited thermal modes with $k_\mathrm{B}T > \hbar\omega_\perp$ as independent ideal 1D Bose gases, thereby using Eq. (3.30).

For a direct comparison to the density profiles, we take here the approach of varying the numerical value of the chemical potential in our model, until the total density from Eq. (3.32) matches the experimental profile at the trap centre. The values of temperature and chemical potential are obtained in the experiment by fitting the wings of the atomic density profile with the ideal Bose gas distribution.

In our method we choose to fix the temperature to that reported in the experimental papers, whereas the chemical potential is used as a free parameter in our model. A comparison between the value for the numerical chemical potential and the one extracted from the experiment is also reported in each case.

A further interesting point to highlight is a common feature shared between the experimental density profiles obtained with absorption imaging, and the ones obtained with our stochastic model: namely both density distributions require further analysis to extract the phase coherent (i.e. ‘true’ condensate) and density coherent (i.e. quasi-condensate) fractions. This is because the SGPE, as well as the experimental measurements, provides with an atomic density distribution which includes both coherent and incoherent atoms. In particular, while in the experiment the identification of quasi-condensate is obtained by performing bimodal fits on the total density profile, in the case of SGPE, knowledge of the second-order correlation function is sufficient to extract this component, as previously discussed in Section 3.7.1. We emphasise that all total densities presented in this chapter correspond to transversely integrated densities in the trap.

4.1.1 Comparison to work of Trebbia *et al.* [Phys. Rev. Lett. 97, 250403 (2006)]

In the experiment by Trebbia *et al.* [59] an atom chip was used to confine a finite-temperature weakly-interacting Bose gas, in a quasi-one-dimensional geometry, with trap frequencies $\omega_z = 2\pi \times 15.7\,\mathrm{Hz}$ and $\omega_\perp = 2\pi \times 2.75\,\mathrm{kHz}$. Atomic density distributions were measured *in situ*, by means of absorption imaging, at

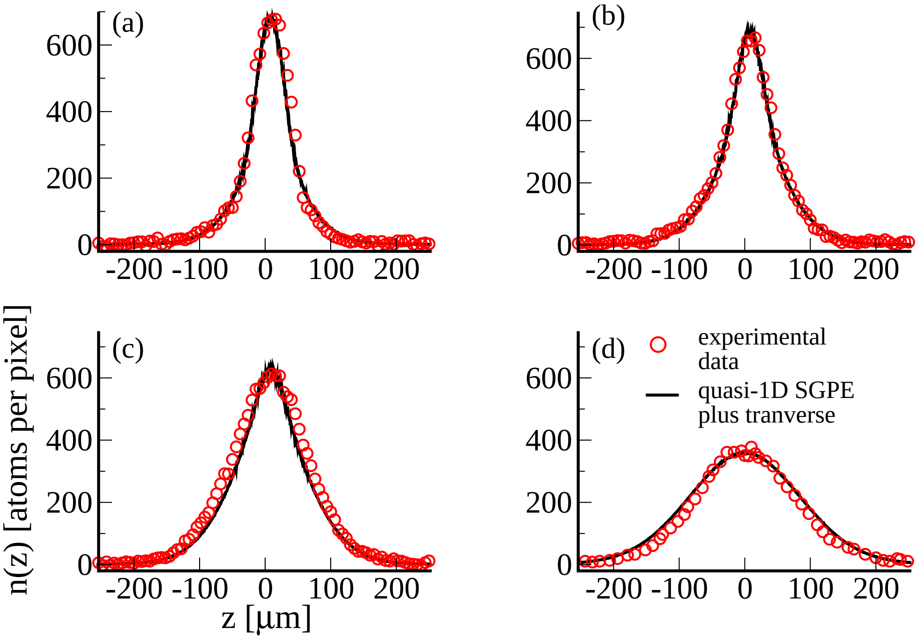

Figure 4.1: Total density profiles from the quasi-1D SGPE model (Eq. 3.32; black solid line) versus data from the experiment of Trebbia *et al.* [59] (red circles), at $T = 302\,\text{nK}$ (a), $T = 362\,\text{nK}$ (b), $T = 434\,\text{nK}$ (c), $T = 759\,\text{nK}$ (d).

four different values for the temperature (red circles, Figure 4.1).

The gas was shown to undergo a smooth crossover between the classical and the quasi-condensate regime. The published theoretical analysis to interpret the results was based on a 3D Hartree-Fock approach, which failed to explain the formation of quasi-condensate in the centre of the trap. It was concluded that the reason for this failure is linked to the too large density fluctuations that the Hartree-Fock approach predicts in a quasi-one-dimensional gas; the spatial correlations induced by interactions between particles are not properly accounted for in this model. These density correlations [156, 189–191] are key to correctly predicting the onset of quasi-condensation and the associated reduction in density fluctuations.

Figure 4.1 shows that our numerical prediction for the density profile (black solid lines) provide instead excellent agreement with the experimental density profiles, across the entire range of temperatures considered. In particular while the Hartree-Fock approach was shown to provide good matching with the experimental atomic density profile at the highest temperature considered (see Fig.1(a) in [59]), but found to have a lower peak than the experimental data at the crossover temperature (see Fig.1(c) in [59]), the total density profile calculated with Eq. (3.32) in our model instead accurately reproduces the experimental profile even at the

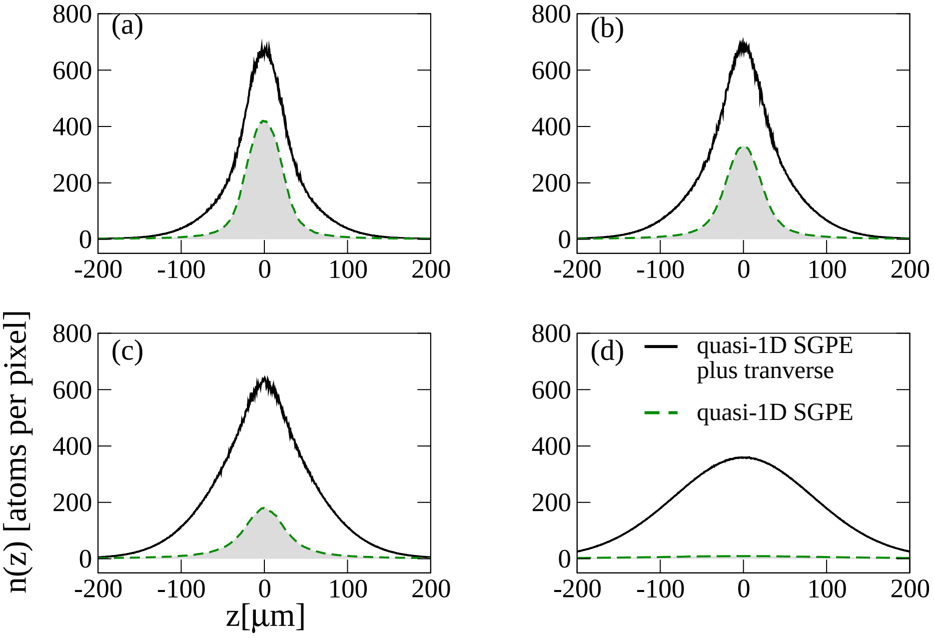

Figure 4.2: Quasi-1D SGPE contribution (Eq. (3.28); green dashed shaded region) to the total density profiles (Eq. (3.32); black solid line). Parameters as in Figure 4.1.

crossover between classical and quasicondensate regime (Fig. 4.1(c)). The breakdown of the Hartree-Fock approach in this regime is due to the absence of a well defined mean-field, caused by the enhanced fluctuations, that are instead retained within the stochastic wavefunction in the quasi-1D SGPE.

The total density profiles reported in Figure 4.1 (black solid lines) are due to two contributions, namely the axial density $\langle|\psi(z)|^2\rangle$ obtained from the solution of the stochastic quasi-1D SGPE (Eq. 3.28), and the density of transverse thermal atoms, $n_\perp$, with energy $k_\mathrm{B}T > \hbar\omega_\perp$ (Eq. 3.29). It is then interesting to see the individual effect due to each density, on the total density profile; this is done by isolating the contribution due the axial quasi-1D SGPE density (green dashed, shaded region in Figure 4.2), from the total density (black solid line, Figure 4.2).

We notice that the density due to the atoms in the axial modes decreases with increasing temperature, and in the highest temperature case (Figure 4.2(d)), where $\mu < 0$, we have essentially a thermal gas, as the total density is due only to the atoms in the transverse excited modes.

We have previously mentioned that in our numerical approach we fix the temperature to the experimentally measured value, and use the chemical potential as a free parameter. Table 4.1 reports a comparison between the calculated values for μ in our model, and the ones obtained from the published Hartree-Fock

Fig.	$k_B T/\hbar\omega_\perp$	$\mu/\hbar\omega_\perp$	
		Analysis of [59]	Current SGPE analysis
		3D Hartree-Fock	Quasi-1D
4.1a	2.3	0.40	0.58
4.1b	3.0	0.65	0.49
4.1c	3.3	0.60	0.26
4.1d	5.8	-6.78	-6.78

Table 4.1: Chemical potentials obtained from the current quasi-1D SGPE model versus the Hartree-Fock analysis of [59] for the density profiles of Fig.4.1. These parameters are for ^{87}Rb atoms and trap frequencies $\omega_\perp = 2\pi \times 2750\text{Hz}$ and $\omega_z = 2\pi \times 15.7\text{Hz}$.

analysis: we observe a slight variation in the three lowest temperature cases considered. The chemical potential is somewhat dependent on the model used; this is because theories approximate the full quantum Hamiltonian of the interacting system to different orders (see e.g. [120]), therefore the chemical potential which appears in the model, and compared to experiment, represents an approximation to the underlying, true value. In making different approximations, different theories capture the true chemical potential to differing degrees of accuracy.

4.1.2 Comparison to work of van Amerongen *et al.* [Phys. Rev. Lett. 100, 090402 (2008)]

In this section we further probe our model, by investigating the measurements of van Amerongen *et al.* [60]. As in the experiment by Trebbia *et al.* [59], previously discussed, a quasi-1D weakly-interacting degenerate Bose gas is realised on an atom chip, whose confining magnetic trap has frequencies $\omega_z = 2\pi \times 8.5\,\text{Hz}$ and $\omega_\perp = 2\pi \times 3.28\,\text{kHz}$. We notice that the confinement in this case is tighter than the previous experiment since the aspect ratio, $\omega_\perp/\omega_z$, is more than twice as big as the one in Trebbia *et al.* [59]: this implies that the gas in this case is closer to a pure one-dimensional configuration. The density distributions were measured *in situ*, at four different values of the temperature (red circles, Figure 4.3), and the formation of a quasi-condensate was observed (red circles, Figure 4.3)(d)). The experimental results were analyzed via a model based on the Yang-Yang thermodynamic formalism [192], a method also referred to as the thermodynamic Bethe ansatz. This was the first experimental comparison to the exact Yang-Yang thermodynamic solution to the finite temperature 1D Bose gas problem. In particular, the solution to the one-dimensional Yang-Yang thermodynamics corresponds to the density given by the atoms in the axial modes, while the transverse excited modes with energy $k_\text{B}T > \hbar\omega_\perp$ are also accounted for with the method adopted here, i.e. Eqs.(3.29)–(3.30). The density profiles resulting from this approach showed very good agreement with the experimental findings (see Fig.1 in [60]).

In order to reproduce the experimental results, we apply the same approach adopted in Section 4.1.1, i.e. we use the quasi-1D SGPE (Eq. 3.28) for the axial modes, and Eqs. (3.29)–(3.30) for the tranverse excited modes. It is interesting to notice that the SGPE contribution, $\langle|\psi(z)|^2\rangle$, here plays the same role as the 1D Yang-Yang prediction of the published theoretical analysis in [60]. As a consequence, by modeling the experimental density distributions, we also (indirectly) obtain information on how good is the matching between the SGPE model predictions and those obtained with the Yang-Yang thermodynamics.

Figure. 4.3 shows that the agreement between the experimental data and the proposed quasi-1D SGPE approach is again very good across the entire temperature range probed, including the crossover from quasi-condensate to degenerate thermal gas (Figure. 4.3(c)).

We now want to test the importance of the quasi-1D character of the SGPE in the physical regime considered in the experiment. In order to do so we simply replace the quasi-1D SGPE (Eq. 3.28) with the pure one-dimensional SGPE (Eq. 3.14). This essentially amounts to substituting the quasi-1D non-linearity,

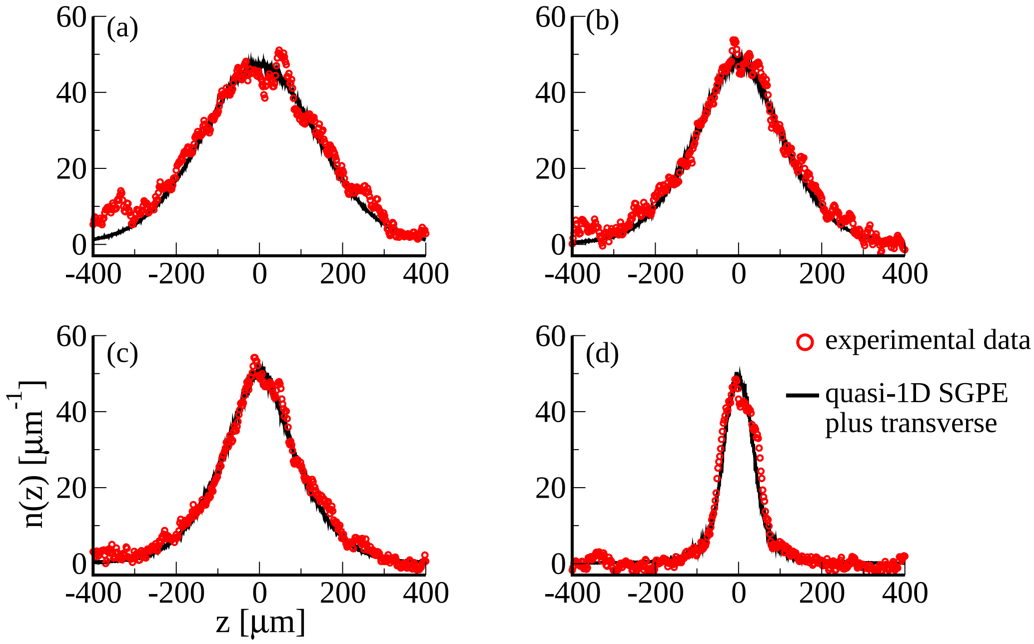

Figure 4.3: Total density profiles from the quasi-1D SGPE model (Eq. 3.32; black solid line) versus the experimental data of van Amerongen *et al.*[60] (red circles), at $T = 620\,\mathrm{nK}$ (a), $T = 440\,\mathrm{nK}$ (b), $T = 380\,\mathrm{nK}$ (c), $T = 140\,\mathrm{nK}$ (d).

$\hbar\omega_\perp\left[\sqrt{1+4|\psi|^2 a_{\rm s}}-1\right]$, with the usual 1D form, $g_{\rm 1d}|\psi(z,t)|^2$ (where $g_{\rm 1d} = 2\hbar\omega_\perp a_{\rm s}$). The transverse thermal atoms are however still accounted for via Eqs. (3.29)–(3.30). In Figure 4.4 we compare the total density profiles obtained by treating the axial modes with the pure 1D SGPE (brown solid line) against the quasi-1D SGPE (black solid line), at each temperature investigated. The results obtained by using the pure 1D SGPE essentially recover the predictions derived by using the quasi-1D SGPE, and consequently also provide an excellent agreement with the experimental findings. While adopting the 1D SGPE or the quasi-1D SGPE equally recovers the experimental atomic density distributions at each temperature, the numerical values for the chemical potential differ slightly between the two approaches. This suggests that if we are to match the experimental density profile at each experimental T, different values of μ are required. This is shown in Table 4.2, where the parameters predicted by the quasi-1D SGPE, 1D SGPE and modified Yang-Yang models are reported. However we find a remarkable result: the values of the chemical potential used to obtain the 1D SGPE results are *identical* to those obtained from fits of the modified Yang-Yang model to the density data in [60]. These predictions have also been found to arise in the context of the 1D stochastic projected Gross-Pitaevskii equation (SPGPE) in the work of Davis *et al.* [193]; as a consequence we have indirectly gained an insight on the agreement

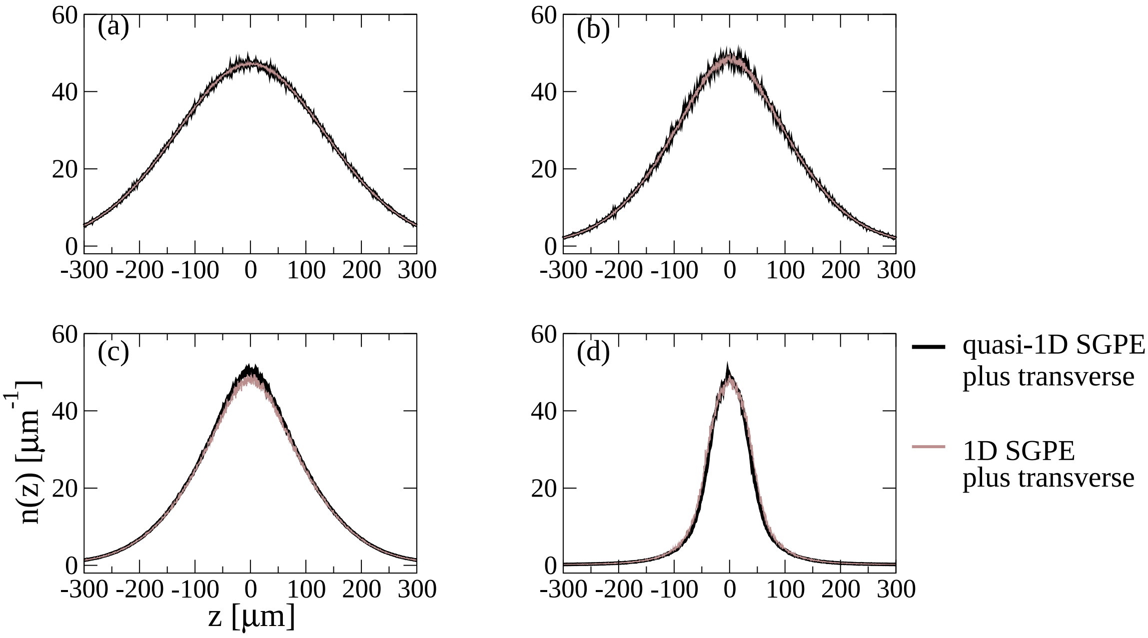

Figure 4.4: Quasi-1D SGPE (thick black line) versus 1D SGPE (thin brown line) density profiles. Each equation is supported by a static treatment of the transverse modes via Eqs.(3.29)–(3.30). Parameters as in Figure 4.3.

between 1D SGPE, the 1D SPGPE and Yang-Yang thermodynamics.

Fig.	$k_BT/\hbar\omega_\perp$	$\mu/\hbar\omega_\perp$		
		Analysis of [60]	Current SGPE analysis	
		modified Yang-Yang	1D	Quasi-1D
4.4a	4.0	-2.74	-2.74	-2.74
4.4b	2.8	-0.38	-0.38	-0.38
4.4c	2.4	0	0	0.03
4.4d	0.89	0.45	0.45	0.39

Table 4.2: Chemical potentials obtained from the current quasi-1D SGPE model versus the Yang-Yang analysis of [60] for the density profiles of Figures 4.3-4.4. These parameters are for ^{87}Rb atoms and trap frequencies $\omega_\perp = 2\pi \times 3280$Hz and $\omega_z = 2\pi \times 8.5$Hz.

While in the regime analyzed in the work by van Amerongen [60] , there is no significative difference between the 1D SGPE and its quasi-1D form, in the next section we will demonstrate that the quasi-1D SGPE is crucial for accurately matching the density fluctuations in the experiment by Armijo *et al.* [61].

4.2 Density fluctuations: comparison to work of Armijo *et al.* [Phys. Rev. Lett. 105, 230402 (2010)]

In a recent work (Ref. [61]), Armijo *et al.* measured the second and third moments of the density fluctuations of a harmonically trapped, finite temperature weakly-interacting Bose gas, comparing these to theoretical predictions from ideal Bose gas and quasi-condensate mean-field models, and also the modified Yang-Yang model of Ref. [60], mentioned in Section 4.1.2. The measure of density fluctuations was performed *in situ*, analysing the absorption images of the longitudinal density profiles, obtained by probing the gas via a CCD camera with pixel size $\Delta = 4.5\ \mu m$. Hundreds of images were taken under the same experimental conditions, and a statistical analysis was performed. For each experimental realisation, the number of atoms within each pixel, N, was measured as well as the average number per pixel, $\langle N\rangle$. This allowed to calculate the quantity $\delta N = N - \langle N\rangle$, and consequently the $p_{\rm th}$ moment of the density fluctuations could be evaluated as $\langle \delta N^p\rangle = \langle (N - \langle N\rangle)^p\rangle$.

Both the second ($p = 2$) and third ($p = 3$) order of the density fluctuations were then plotted as functions of the average number of atoms, $\langle N\rangle$, at two values of the temperature. These findings are reported here in Figure 4.5 (red circles), where the top row shows the second moment while the bottom row shows the third moment, each versus $\langle N \rangle$ for two temperatures: $T = 376$nK (left) and $T = 96$nK (right).

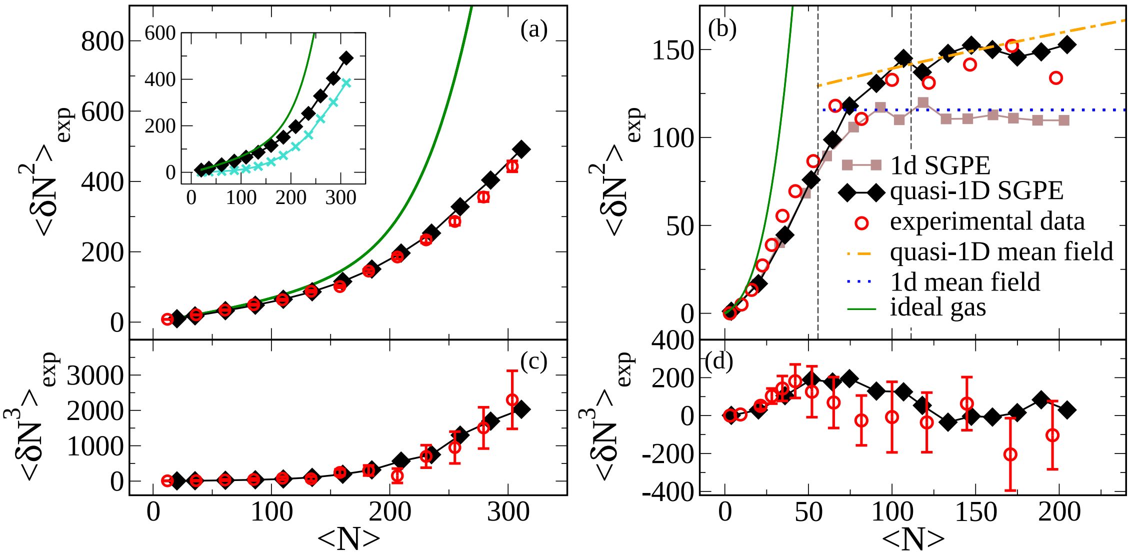

Figure 4.5: Second ((a)-(b)) and third ((c)-(d)) moments of the atom number fluctuations from the quasi-1D SGPE data (filled black diamonds) and experimental data from the paper of Armijo *et al.* [61] (hollow red circles). Temperatures are $T = 376$nK ((a)-(b)) and $T = 96$nK ((c)-(d)). Also shown in (b) are mean field results for an ideal Bose gas (green solid line), 1D quasi-condensate (dotted blue, horizontal) and quasi-1D quasi-condensate (dot-dashed orange); the thin, vertical dashed lines indicate the 'crossover' region where the interaction and thermal energies become comparable. Inset to (a): SGPE result with (filled black diamonds) and without (light blue crosses) transverse contributions to the number fluctuations vs. the ideal gas result (solid green line).

The possibility to span the reported range of $\langle N \rangle$ is allowed by the harmonic potential, that leads to an inhomogeneous density distribution where the number of particles varies spatially. At the edge of the trap, the gas in nondegenerate and is still effectively non-interacting; the low-density wings of the distribution can be therefore considered as an ideal Bose gas. Close to the trap center where the density is higher, the presence of a quasicondensate suggests a high-level of degeneracy. While density fluctuations are enhanced within an ideal Bose gas, due to an effect of quantum statistics that causes atomic bunching, in a quasicondensate instead, spatial correlations induced by interactions lead to a suppression of density fluctuations relative to those expected in an ideal gas. Thus, at a single temperature, by scanning the spatial extent of the trapped gas it is possible to observe both the enhancement of density fluctuations, due to quantum statistics (low density, ideal Bose gas), and their subsequent suppression, due to particle interactions (higher density, quasi-condensate regime) [61–63].

The experimental results for the second moment show that density fluctuations increase with increasing $\langle N\rangle$, and then saturate in the lower temperature case, $T = 96$nK [Fig. 4.5(b)], at high value of the average atom number. The reason why density fluctuations do not saturate in the higher temperature case [Fig. 4.5(a)], is due to the presence of a smaller quasicondensate.

In Figure 4.5(b) we also report mean-field results for density fluctuations, valid in the appropriate limits. Mean-field results for the density fluctuations can be derived from the thermodynamic relation $\langle \delta N^2\rangle = k_B T \varDelta (\partial n/\partial \mu)_T$ [194]. The ideal gas result, which should be valid in the case of small $\langle N\rangle$, i.e. at the trap edges [solid green line in Figs. 4.5(a)-(b)], thus becomes [62]:

$$\langle \delta N^2\rangle = \frac{\varDelta}{\lambda_{\mathrm{dB}}} \sum_{j=1}^{\infty} \sqrt{j} \frac{e^{j(\mu - V(z))/k_B T}}{\left(1 - e^{-j\hbar\omega_\perp/k_B T}\right)^2}. \tag{4.1}$$

The quasi-condensate equation of state, valid at large $\langle N\rangle$, i.e. the central trap region, yields instead $\langle \delta N^2\rangle_{\mathrm{quasi-1D}} = \langle \delta N^2\rangle_{\mathrm{1D}} \left[1 + (\mu - V(z))/\hbar\omega_\perp\right]$ [dot-dashed orange line in Fig. 4.5(b)], where $\langle \delta N^2\rangle_{\mathrm{1D}} = k_B T \varDelta / g$ is the result for a purely 1D equation of state ($\mu[n] = gn$) [63] (horizontal dotted blue line).

The theoretical analysis reported in Armijo *et al.* [61] to model the experimental results was based on the modified Yang-Yang approach [60]. This provided good agreement in the regime where the gas is nondegenerate (low values of $\langle N\rangle$), but it failed to describe the observed behaviour in the quasi-condensate regime [corresponding to $\langle N\rangle \gtrsim 70$ in Fig. 4.5(b)]. In this regime the modified Yang-Yang model predicted too great a reduction in density fluctuations, relative to the observed experimental behaviour, and recovered the 1D mean-field result (horizontal dotted blue line).

While the mean-field result based on the ideal gas equation of state [solid green line in Figs. 4.5(a)-(b)] is valid only for small densities, and that from the quasi-1D equation of state [dot-dashed orange line in Fig. 4.5(b)] holds at high densities, the quasi-1D SGPE [filled black diamonds Fig. 4.5(a)-(b)], like the experimental data, provides a smooth crossover between each of these regimes. The predictions of the quasi-1D SGPE capture the experimental behaviour very well at both temperatures, and are also in good agreement with the quasi-1D mean field expression [dot-dashed orange line in Fig. 4.5(b)]. We also find that using the 1D SGPE [filled brown squares of Fig. 4.5(b)] leads to a good matching with the 1D mean-field results [horizontal dotted blue line of Fig. 4.5(b)], and consequently with the modified Yang-Yang prediction of Ref. [61], hinting once again to good agreement between 1D SGPE and Yang-Yang. Physically, this suggests that the effect of the transverse swelling of the quasi-condensate near the centre of the trap cannot be ignored for these parameters, and that the quasi-1D extension to the SGPE is therefore essential here. Importantly, our numerical results for the quasi-1D SGPE [filled black diamonds of Fig. 4.5(b)] show that this model captures the experimental data across the *entire* parameter regime very well, thereby improving on the theoretical analysis reported in Armijo *et al.* [61]. Finally we also notice the good agreement (within experimental error bar) between the predictions of the quasi-1D SGPE and the experimental results for the third moment of density fluctuations, as shown in Figure 4.5(c)-(d). A description of the methodology undertaken to reproduce the experimental findings follows.

4.2.1 Numerical SGPE procedure

We now describe the procedure we adopted to reproduce the experimental results on density fluctuations of Armijo *et al.* [61]. In our stochastic treatment, every run of the SGPE can be loosely associated to an experimental realisation. We perform around 1000 numerical simulations, in each temperature case investigated. Each numerical realisation of the noise in the SGPE provides with a fluctuating density profile, $|\psi(z)|^2$, given by Eq. (3.28); in order to mimic the experimental procedure, we also perform the spatial binning, which effectively divides the numerical data into Δ-sized regions (where Δ is the spatial resolution of the CCD camera). The same procedure is applied to the average, $\langle|\psi(z)|^2\rangle$, performed over the several numerical noise realisations, and also to the transverse density profile $n_\perp$ of Eq. (3.29). The axial contribution, N_z, to the total atom number within a pixel is then given by the integral of $|\psi(z)|^2$ over that pixel, as well as the transverse contribution, $N_\perp$ is instead given by the integral of the transverse profile over the same pixel. The total atom number within the pixel is therefore given by $N = N_z + N_\perp$. Figure 4.6 shows a comparison between the single run (black) and average (red solid line) profiles, after spatial binning; we notice the qualitative agreement with the experimental binned data, reported in Fig.1(c) of Ref. [61]. The inset of Fig. 4.6 shows instead single run and averaged density profiles prior to spatial binning. As we treat the atoms in the transverse modes in a static way, they give a non-zero contribution only to average properties, and so do not contribute to moments of the density fluctuations directly. However these atoms are treated as 1D ideal Bose gases, and therefore the following approximation $\langle\delta N^2\rangle_\perp \simeq \langle\delta N^3\rangle_\perp \simeq \langle N\rangle_\perp$ [61] holds at small densities. We then assume the atoms in the excited transverse modes give a contribution $\langle N\rangle_\perp$ to the second

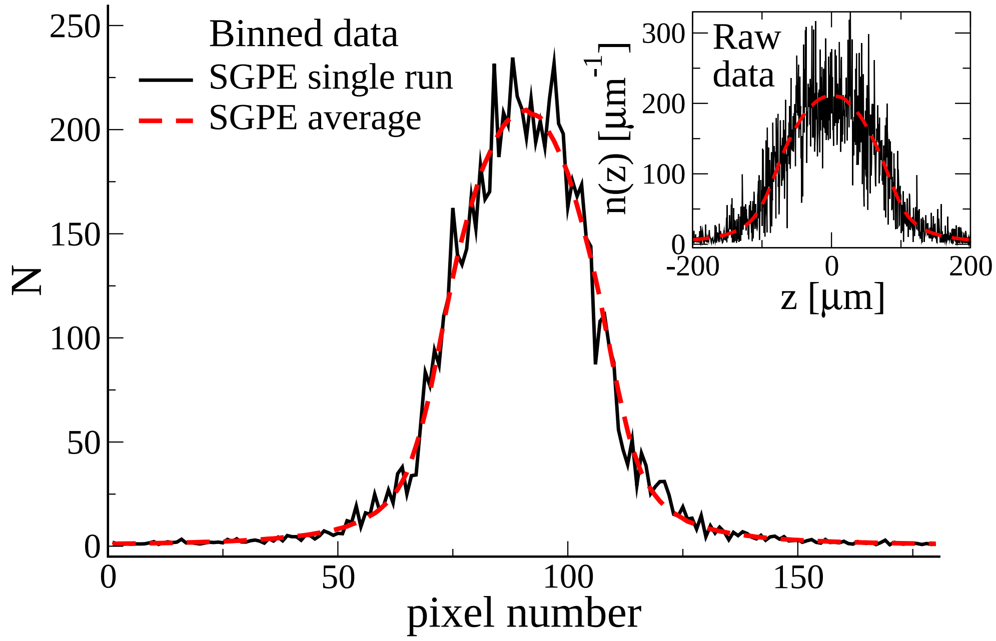

Figure 4.6: SGPE density following spatial binning for single realisation (noisy black line) and average data (dashed red line); the inset shows the raw data prior to binning.

and third moment of the atom number fluctuations, yielding:

$$\langle \delta N^p \rangle = \langle (N_z - \langle N_z \rangle)^p \rangle + \langle N \rangle_\perp. \tag{4.2}$$

The role of the atoms in the transverse modes is particularly important for the high temperature case, and its role was crucial to accurately match the experimental values for the second moment of fluctuations. This is shown in the inset of Fig. 4.5(a), where we compare the SGPE results for density fluctuations with (black diamonds) and without (light blue crosses) contribution from the atoms in the transverse modes, $N_\perp$. The inclusion of $N_\perp$ results in a noticeable shift upward in the SGPE data, leading to a very good agreement with the experimental results (red circles). The corresponding comparison for the lower temperature case is not reported, as the difference between the two approaches is negligible.

Finally, we mention that in order to reproduce the experimental results, we take into account systematic effects reported in [61], that lead to a factor κ_p relating the experimentally measured moments, $\langle \delta N \rangle_{\rm exp}$, to the true values, via $\langle \delta N^p \rangle_{\rm exp} = \kappa_p \langle \delta N^p \rangle$. The factor κ_p arises due to the finite spatial resolution of the experiment and therefore we also scale our theoretical findings by the published values of κ_p [61], in order to account for this experimental issue.

4.3 Chapter summary

The quasi-1D SGPE (Eq. 3.28) supported by Eq. (3.29) for the transverse excited modes was shown to provide excellent *ab initio* predictions for both *in situ* experimental density profiles obtained by Trebbia *et al.* [59] and van Amerongen *et al.* [60], and *in situ* density fluctuation data from the experiment of Armijo *et al.* [61]. This was achieved by matching peak densities (equivalent to total atom number).

The study of density fluctuations showed that our combined approach captures all experimental regimes studied in a unified manner, smoothly interpolating between mean field models, whose individual validity is restricted to either the low density or high density regimes. Importantly, it was found that analyzing individual stochastic realisations in the same way as individual experimental runs (once experimental resolution issues are properly accounted for), led to good agreement between the density statistics in each case.

Reducing our stochastic model to the previously tested one-dimensional stochastic Gross-Pitaevskii equation showed that: (i) the latter model is consistent with Yang-Yang predictions (in the weakly-interacting regime probed here); (ii) while both one-dimensional and quasi-one-dimensional approaches accurately reproduce equilibrium density profiles, they do so with slightly different chemical potentials.

Chapter 5

Phase coherence I : *Ab initio* modelling of experiment by Richard *et al*. [Phys. Rev. Lett. 91, 010405 (2003)]

In this chapter we undertake an *ab initio* analysis of the experimental findings by Richard *et al.* [54], using the Stochastic Gross-Pitaevskii model described in Chapter 3. The experimental investigation aimed to extract the phase coherence properties of weakly interacting, quasi-1D Bose gases in the 'strong' phase fluctuation regime for which $T \gg T_\phi$, namely here $6 < T/T_\phi < 28$; we will mainly focus on the modelling of the temperature dependence of the coherence length, L_c. In Section 5.1 we provide a brief description of this experiment. In Section 5.2 we explain the methodology we adopt to reproduce the experimental findings and in Section 5.3 we compare our results to the experimental ones.

5.1 Description of the experiment

In the experiment by Richard $et\ al.$ [54], carried out in the group of A. Aspect in Orsay (Paris), the phase coherence properties of quasi-condensates in elongated harmonic traps were investigated. The experimental sequence consisted of loading a beam of ^{87}Rb atoms in a magneto-optical trap (MOT) and optically pumping the atoms into the F=1 state, before transferring them to an anisotropic Ioffe-Pritchard trap [94]. The aspect ratio of the trap was $\lambda = 152$, the frequencies being $\omega_\perp = 2\pi \times 760$ Hz and $\omega_z = 2\pi \times 5$ Hz. In this way, they managed to produce cigar-shaped quasi-condensates with atom numbers in the range $0.25\times10^5 - 0.65\times$

10^5 and typical half-length $L(\text{axial size}) \sim 130\ \mu\text{m}$ and $R_\perp(\text{radial size}) \sim 0.8\ \mu\text{m}$. These parameters enabled the 'strong' phase fluctuation regime $6 < T/T_\phi < 28$ to be probed: in this range of temperatures, fluctuations in the phase play a dominant role in the behaviour of the system, whereas density fluctuations, although still present, are relatively suppressed compared to phase fluctuations.

In order to investigate the phase coherence properties of the gas, the axial momentum distribution was measured by means of Bragg spectroscopy [54, 94]. Two counterpropagating laser beams formed a standing wave, which was moved over the condensate so that the atoms were diffracted out of the condensate by interaction with the wave. By measuring the fraction of atoms scattered out of the condensate as a function of the detuning between the two counterpropagating laser beams, the momentum profile was extracted along the axial direction of the sample. Several spectra were measured at different temperatures varying from $85 \leq T \leq 350$ nK, in the regime $0.3 \leq T/T_\text{c} \leq 0.9$. The momentum distributions were found to have Lorentzian shapes, resulting in an exponential decay of the correlation function in space, typical of large phase fluctuations [53, 54, 58, 64]. The coherence length L_c was then extracted from the measure of the half width at half maximum (HWHM) of the momentum profile, which was found to become smaller for decreasing temperatures. They found values of the coherence length in the range $5.9 \leq L_\text{c} \leq 39\,\mu\text{m}$; these values, scaled to the half-length of the quasi-condensate, were found to be in the regime $0.05 \leq L_\text{c}/L \leq 0.28$. Since the coherence length, L_c, is smaller than the axial size, L, for all cases the coherence does not extend over the whole system size, and the system is thus a quasi-condensate.

It is interesting to study how the coherence length, L_c, varies with temperature, T, for a weakly-interacting Bose gas confined in harmonic trap. Such behaviour should best be characterised in a universal manner, i.e. by eliminating any dependence on the system parameters, such as trap frequencies, atom number and length. For example, investigating the absolute value of the coherence length with two different experimental configurations, characterised by different trap aspect ratios, system atom numbers, and system sizes, may lead to different results; however this does not indicate that one system is more phase coherent than another. For this reason it is convenient to scale the coherence length to the axial half-length of the system, L, and investigate the behaviour of this quantity against a reduced temperature, T/T_ϕ, where T_ϕ is the characteristic temperature associated with the onset of phase fluctuations [31]. In Ref. [54] T_ϕ was defined in terms of the 1D axial quasi-condensate peak density, $n_\text{qc}(0)$, rather than in terms of total atom number and chemical potential, as already introduced in Eq. (1.13). The corresponding expression was defined as [54]:

$$T_\phi[n_{\rm qc}(0)] = \frac{\hbar^2 n_{\rm qc}(0)}{m k_B L}. \tag{5.1}$$

This is the most general expression for T_ϕ, and only requires the Local Density Approximation to hold, as demonstrated in [101]; for details of how this expression relates to the one used in the experiment of Ref. [95], analysed in Chapter 6, see also Appendix B.

The experimental values of the coherence length $L_{\rm c}$, scaled to the half-length of the condensate L, are shown plotted against the reduced temperature T/T_ϕ in Figure 5.4 . Such a graph may be generated by extracting L from Figure 3 of Ref. [54], and the remaining data from Figure 3 of Ref. [94].

The measured values of the axial length in the experiment were found to be systematically lower than the Thomas-Fermi prediction. This difference resulted from radial quantum pressure (zero point oscillation in the tight trapping potential), and the compressing effect of the thermal cloud (particles with energy $\epsilon \gg \hbar\omega_\perp$) [94]. The model used to calculate the axial length includes the above effects: i) the role of radial quantum pressure was taken into account by finding the optimal ground state energy (see details in [195]), while ii) the effect of the thermal cloud was taken into account within a Hartree-Fock-like approach [33, 196, 197]. In particular the effect deriving from the compression exerted by the thermal cloud onto the condensate is calculated via [198]:

$$L^2 = \frac{2g_{3\rm d}}{m\omega_z^2}\left\{ n_0(0) + \frac{2}{\lambda_{\rm dB}^3}[g_{3/2}(e^{-\beta g n_0(0)}) - g_{3/2}(1)]\right\}, \tag{5.2}$$

where $g_{3/2}(x) = \sum_{n=1}^{\infty} x^n/n^{3/2}$ and $n_0(0)$ denotes here the quasi-condensate peak density. The density distribution for the thermal component is calculated within a self-consistent Hartree-Fock model as [198] $n_{th}(\mathbf{r}) = \lambda_{\rm dB}^{-3}\, g_{3/2}(e^{-\beta(\mu - V_{\rm eff}(\mathbf{r}))})$, where $V_{\rm eff} = V_{\rm ext} + 2g_{3\rm d}(n_0 + n_{\rm th})$. We notice that if the thermal cloud did not play role in the determination of the half-length of the quasi-condensate, then Eq. (5.2) would simply reduce to the usual Thomas-Fermi radius $L^2 = 2\mu/m\omega_z^2$.

5.2 Methodology

In this section we describe the methodology followed in our SGPE numerical simulations to extract the coherence properties of quasi-1D Bose gases, such that we reproduce the experimental findings of Richard *et al.* [54]. In Ref. [54] measurements of the coherence length were taken for *seven* different systems, i.e. characterized by different temperatures and atom number, but same trap configuration and atomic species. These experimental data are reported in Figures 5.4 and 5.5 (hollow red triangles). Our aim is to reproduce each of these seven experimental measurements within our model and thus determine from a fully *ab initio* perspective the temperature dependence of the coherence length in the 'strong' phase fluctuation regime $6 < T/T_\phi < 28$. The experimental information available to us from this experiment was the quasi-condensate atom number and the values of the temperatures at equilibrium (as reported in Figure 3 of [54]), together with trap frequencies and atomic species properties. Since we did not have access to the total atom number in each experimental realization, we decided to match the experimental quasi-condensate atom number with our numerical quasi-condensate one, extracted via Eq. (3.35).

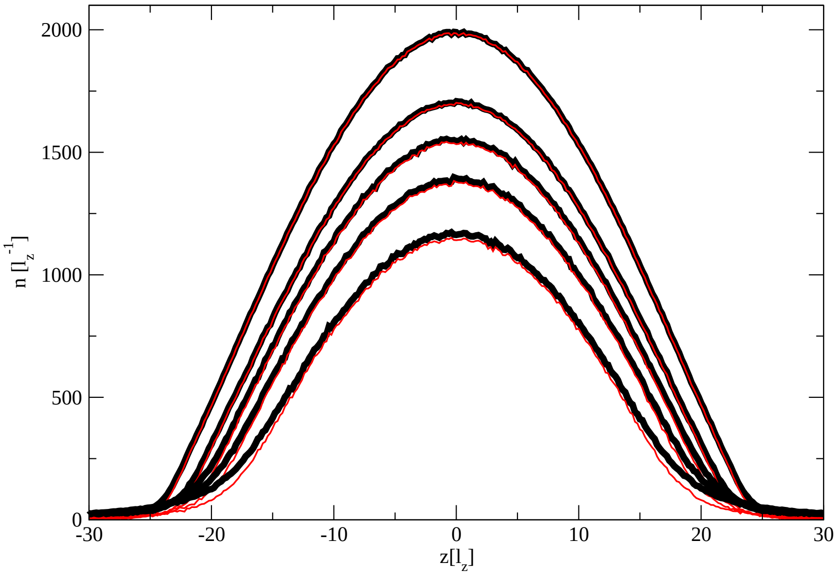

Figure 5.1: SGPE axial density profiles, $\langle|\psi|^2\rangle$ (solid black) with corresponding quasi-condensate density (solid red), for five temperatures cases: (from top to bottom) $T/T_\phi[n_{\rm qc}(0)] = 4.5, 6.9, 12.9, 16.6, 24.9$ ($T = 87.5, 122.5, 215, 260, 345\,n$K). The parameters used for the trap are $\omega_z = 2\pi\,\times\,5\,$Hz and $\omega_\perp = 2\pi\,\times\,760\,$Hz as in [54].

For this reason we find it convenient to consider only the quasi-one-dimensional SGPE (Eq. (3.28)) within the model described in Part II, without explicitly considering the contribution of the transverse thermal atoms given by Eq. (3.29) (which would of course be needed if comparing total atom number between simulations and experiment). This is because the quasi-condensate density in our numerical simulations is calculated via Equation (3.35), which does not require a solution to the equation for the transverse excited modes (Eq. (3.29)). Therefore, for every data point considered, we match the temperature with the experimental one, and set the chemical potential in our simulations to a suitable value such that the quasi-condensate number, extracted with Eq. (3.35), matches the values quoted in [54]. In each case we generate a large number of stochastic realizations (typically ~ 1000), which allows to obtain very smooth density profiles. Figure 5.1 shows SGPE averaged density profiles (solid black) for five temperature cases (from top to bottom $T/T_\phi[n_{\rm qc}(0)] = 4.5, 6.9, 12.9, 16.6, 24.9$), with corresponding quasi-condensate densities (solid red) extracted via Eq. (3.35). We notice that in each temperature case, the difference between the SGPE density distribution and the corresponding quasi-condensate profile is very small, even at the highest temperatures probed, even though this difference increases at higher temperature. This suggests that at such temperatures, almost the entire system is a quasi-condensate, i.e. the gas is practically fully density coherent. In order to access

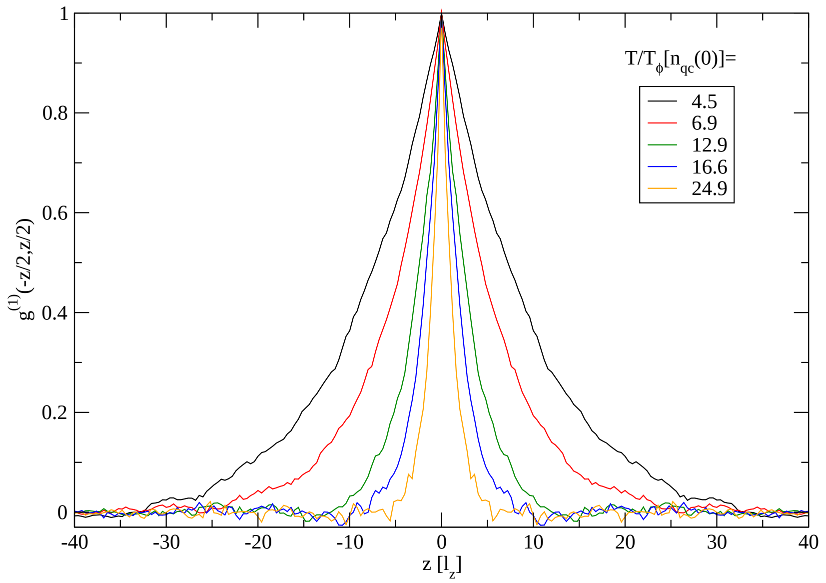

Figure 5.2: Symmetrical correlation functions normalized to the center, at $T/T_\phi[n_{\rm qc}(0)] = 4.5\,(\text{black}), 6.9\,(\text{red}), 12.9\,(\text{green}), 16.6\,(\text{blue}), 24.9\,(\text{yellow})$. Parameters from Ref. [54], as in Figure 5.1.

the information about phase coherence, we compute the first order symmetrical correlation function (normalized to the central peak density) for each individual realization of the noise: Figure 5.2 shows $g^{(1)}(-z/2, z/2)$ for the same temperature cases discussed above. We notice that these functions have an exponential-like behaviour, as also found in the experiment, and that at higher temperature they decay faster to zero since $T \gg T_\phi$.

The coherence length, L_c , is usually determined as the $1/e$ value of the correlation function, because of its exponential behaviour; however, this is not appropriate for $T \sim T_\phi$, where the correlation function tends to a Gaussian-like behaviour, as previously shown in Part II. In order to have a consistent measure throughout the entire regime of T/T_ϕ and to be able to compare directly to the experimental findings, we adopt the method used in the experiment: we compute the axial momentum distribution by taking the average (over the number of noise realizations) of the Fourier transforms of each individual spatial correlation function. This is denoted by $C^{(1)}$ and takes the form:

$$C^{(1)} = \langle F\left[\frac{\psi^*(-z/2)\psi(z/2)}{|\psi(0)|^2}\right]\rangle, \tag{5.3}$$

where $F[\cdots]$ denotes the Fourier transform.

Figure 5.3 shows a comparison between $C^{(1)}$ corresponding to the extreme temperature cases in the experimental data set, $T/T_\phi = 4.5$ (solid red) and $T/T_\phi = 24.9$ (solid orange). The profile associated with the highest temperature case is broader, compared to the lower temperature case where a much narrower peak occurs. A Lorentzian fit in both cases highlights that, as in the experiment, we also find in our simulations a Lorentzian like profile of the momentum distributions, characteristic of an exponential decay of the spatial correlation function.

Finally, we measure the half-width at half maximum (HWHM), Δk, of $C^{(1)}$, and the coherence length L_c is then determined by taking the inverse of Δk. We strictly follow this approach for the entire data set, and the results we obtain are compared to the experimental ones, and discussed in the following section.

5.3 Results

We compare the SGPE predictions to the results obtained in the experiment, by plotting the reduced coherence length L_c/L (where L denotes the half-length of the quasi-condensate) against the reduced temperature T/T_ϕ. We use our simulated data to find the value for $T_\phi[n_\mathrm{qc}(0)]$ (Eq. (5.1)), with the required inputs

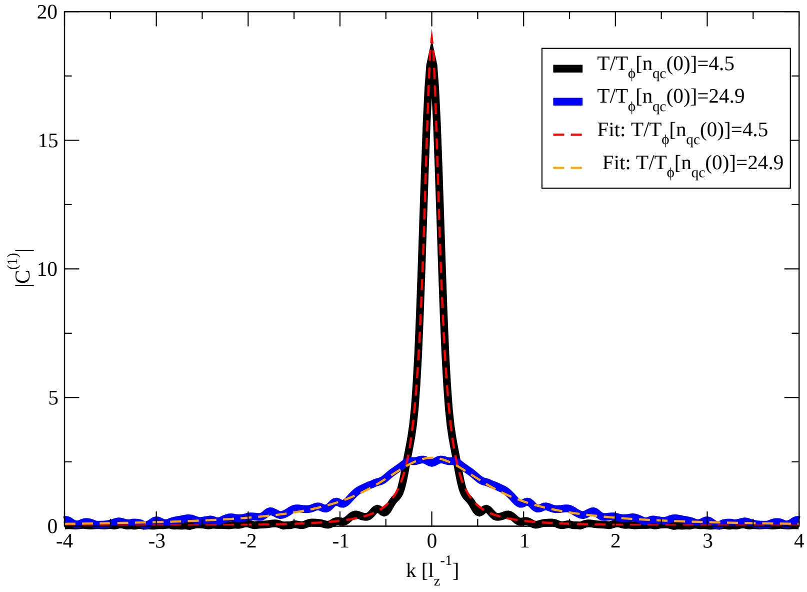

Figure 5.3: $|C^{(1)}|$ (Eq. (5.3)) corresponding to the extreme temperature cases analysed in [54]: $T/T_\phi[n_{\rm qc}(0)] = 4.5$ (solid black) and $T/T_\phi[n_{\rm qc}(0)] = 24.9$ (solid violet). Corresponding Lorentzian fits for $T/T_\phi[n_{\rm qc}(0)] = 4.5$ (dashed red) and $T/T_\phi[n_{\rm qc}(0)] = 24.9$ (dashed orange) are also shown.

being the quasi-condensate peak density and the spatial extent of the gas, each of which we obtain *ab initio*, as described in the previous section. Specifically, the half-length of the quasi-condensate in our simulations is given by the temperature dependent Thomas-Fermi radius $R_{\rm TF}(T)$, as defined in Section 3.7.2. The results are presented in Figure 5.4 which shows excellent agreement between SGPE theory (filled black triangles up) and experimental results (hollow red triangles) in this strong phase fluctuation regime.

An indicative error bar has been calculated for the highest temperature case. For the experimental point we have used a typical 10% uncertainty [54], whereas for the numerical point we have considered a 15% variation in the quasi-condensate atom number and 5% in temperature. We have implemented the above variations in a numerical simulation, and looked at the change in the coherence length $L_{\rm c}$, and in the inputs parameters to $T_\phi[n_{\rm qc}(0)]$, i.e. the quasi-condensate peak density, $n_{\rm qc}(0)$, and the Thomas-Fermi radius, $R_{\rm TF}(T)$. By assuming the errors in each parameter ($L_{\rm c}$, T, $n_{\rm qc}(0)$, $R_{\rm TF}(T)$) to be independent, the total error is then calculated

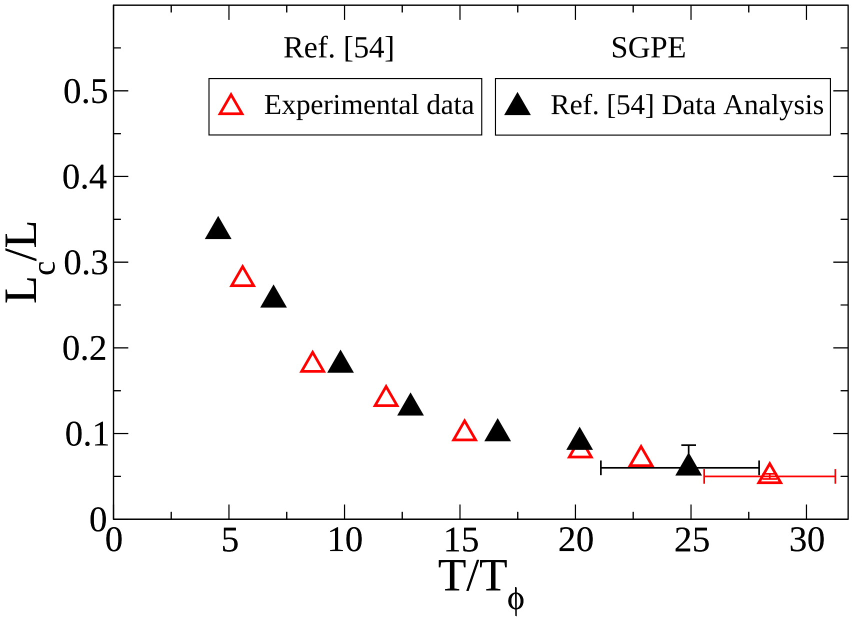

Figure 5.4: Coherence length L_c scaled to the half length of the quasi-condensate L vs. reduced temperature T/T_ϕ. Comparison of experimental data [54] spanning the range $T/T_\phi > 6$ (hollow red triangles) to the SGPE model (filled black triangles up). The horizontal experimental error bar is taken as 10% [54], based on typical experimental uncertainties, while the corresponding error in the simulated point arises from a typical 15% variation in the quasi-condensate atom number and 5% variation in temperature [54]; in both cases the vertical error bars fall within the symbol size. The definition used for the critical temperature T_ϕ is the same for both experimental data and theory and is given by $T_\phi[n_{\rm qc}(0)] = \hbar^2 n_{\rm qc}(0)/mk_B L$, with $n_{\rm qc}(0)$ being the peak quasi-condensate density. The spatial extent of the quasi-condensate in the SGPE model is obtained *ab initio* as the temperature dependent Thomas-Fermi radius $R_{\rm TF}(T)$ (see text).

by considering the individual errors in each parameter, as follows:

$$\begin{aligned} \frac{\delta T/T_\phi}{T/T_\phi} &= \sqrt{\left(\frac{\delta n_{\rm qc}(0)}{n_{\rm qc}(0)}\right)^2 + \left(\frac{\delta T}{T}\right)^2 + \left(\frac{\delta R_{\rm TF}}{R_{\rm TF}}\right)^2} \\ \frac{\delta L_c/L}{L_c/L} &= \sqrt{\left(\frac{\delta L_c}{L_c}\right)^2 + \left(\frac{\delta R_{\rm TF}}{R_{\rm TF}}\right)^2}. \end{aligned} \tag{5.4}$$

Since an increase of 15% in the quasi-condensate atom number does not produce the same effect as a decrease of 15%, the error bar calculated in this manner is not symmetrical. In the temperature range investigated, the coherence length is smaller than the quasi-condensate extent ($L_c/L < 1$), illustrating the fundamental role of phase fluctuations in such an elongated geometry.

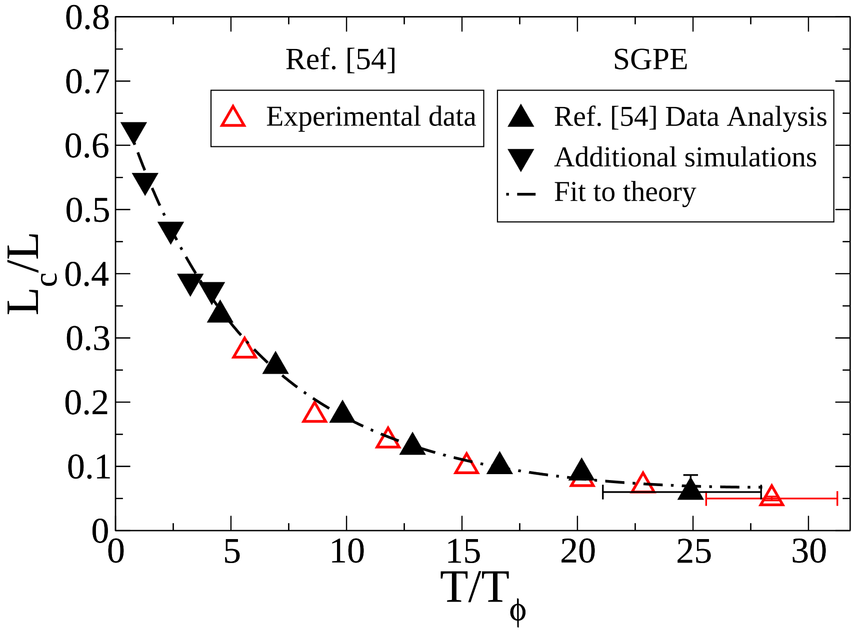

Figure 5.5: Coherence length L_c scaled to the half length of the quasi-condensate L vs. reduced temperature T/T_ϕ. Comparison of the SGPE model predictions (upward filled black triangles) to experimental data [54, 94] spanning the range $T/T_\phi > 6$ (hollow red triangles). Additional numerical results generated with the SGPE model for lower temperatures $T/T_\phi < 6$ are also shown (downward filled black triangles), together with the best fit of the SGPE results (dot-dashed black line).

For values of $T/T_\phi < 6$, we expect the coherence length to increase, since in the limit $T \lesssim T_\phi$ the phase fluctuations are reduced, to the point that the coherence extends over a size comparable to the length of the system. In order to verify this, we generate a further set of numerical points for $T/T_\phi < 6$; specifically, we produce 5 additional numerical results, obtained for values of the temperature which are systematically lower. This enables us to span the temperature regime down to values of $T/T_\phi = 0.8$. We then apply the same procedure used before to extract the relevant parameters (i.e. $L_c, R_{\rm TF}(T), T_\phi$); the results are shown in Figure 5.5 (filled black triangles down), together with the set of values shown in Figure 5.4. The new set of numerical results (filled black triangles down) indeed confirms that the reduced values of the coherence length L_c/L increase with decreasing temperature. Moreover these additional points (filled black triangles down) together with the numerical results from the previous analysis (filled black triangles up) lie on a unified curve; this is obtained by fitting the numerical results with a function of the form Ae^{-Bx-Cx^2}, and fitting parameters $A = 0.69$, $B = 0.169$, $C = 0.003$. We will discuss further about this unified graph, and the 'universal nature' of such a scaled diagram, in the next chapter, where we analyse the related experiment by Hugbart *et al.* [95], investigating the phase properties in the regime $0.8 < T/T_\phi < 8$.

5.4 Chapter summary

In this chapter we have compared our model (for details see Chapter 3) to the experiment of Richard *et al.* [54], which considered the regime of relatively strong phase fluctuations $T/T_\phi > 6$. We have found excellent agreement between SGPE numerical results and experiment, when comparing the temperature dependence of the coherence length in a weakly-interacting elongated Bose gas. In particular the coherence length in our simulations was extracted from the average of the Fourier transform of the first-order correlation function, and was then scaled to the half-length of the quasi-condensate, which is given in our model by the temperature dependent Thomas-Fermi radius. The scaled coherence length was then reported against the reduced temperature, given by the ratio of the absolute value of the temperature to the critical temperature T_ϕ, which sets the onset for phase fluctuations. Importantly, our analysis is totally *ab initio*, thus meaning it is based solely on using the experimental parameters (i.e. trap configuration, atom number, temperature) as inputs for the theory.

Finally we have undertaken further simulations to probe the regime $T/T_\phi < 6$: we have found that our results lie on a unified curve with an exponential-like behaviour, spanning the whole regime of T/T_ϕ. This was also done to set the stage for the task we undertake in the next chapter, where we compare our model to the experiment by Hugbart *et al.*, where the regime of relative weak phase fluctuations ($0.8 < T/T_\phi < 8$) was investigated.

Chapter 6

Phase coherence II : *Ab initio* modelling of experiment by Hugbart *et al*. [Eur. Phys. J. D 35, 155 (2005)]

In this chapter we compare our model to the experimental findings of Hugbart $et~al.$ [95]; this experiment investigated the coherence properties of quasi-one-dimensional Bose gases in the 'weak' phase fluctuation regime where $T \sim T_\phi$, namely here $0.8 < T/T_\phi < 8$. Phase fluctuations in this regime still play a fundamental role but they are reduced with respect to the experiment in [54] analysed in the previous chapter.

In Section 6.1 we describe the experiment of Ref. [95], in which an experimental technique based on interferometry (unlike the Bragg spectroscopy used in Richard *et al.* [54]), was implemented to investigate the phase coherence properties of the system. In Section 6.2 we show that by using the methodology described in the previous chapter to extract the coherence length, we reconcile the experimental findings from the two experiments in [54, 95]. However this procedure turns out to be inadequate to match the experimental data of Ref. [95]. Hence we attempt in Section 6.3 to more closely mimic the procedure followed in [95], finding optimum agreement with the experimental results. Nonetheless there still remains a small issue with the range of T/T_ϕ spanned in our numerics. To address this, we discuss in Section 6.4 two alternative approaches, which lead to an improved agreement with the experimental findings.

In order to compare and contrast the two experiments discussed in the preceeding and in this chapter, details of the experiment by Richard *et al.* [54] (analysed in the previous chapter), and the one by Hugbart $et~al.$ [95] (analysed in this chapter) are summarised in Table 6.1.

6.1 Description of the experiment

The Bragg spectroscopy method used in the previous experiment limited accurate investigations of the coherence properties of the gas to $T/T_\phi > 6$, as at lower temperatures the width of the momentum distribution of the gas was no longer easily resolved [94]. In the experiment described in [95], an alternative interferometry technique (see also Ref. [53]) was used to measure the spatial correlation function in the 'weak' phase fluctuation regime $0.8 < T/T_\phi < 8$.

In particular, after the condensate was released from the trap, two Bragg pulses were applied, playing the role of matter-wave beam splitters. The contrast of the resulting interference fringes was then extracted from the modulus of the Fourier transform of the interference pattern, and the coherence length obtained from the decrease of the contrast as a function of the distance between the two interfering condensates. While in the experiment of Ref. [54] (Chapter 5), it was necessary to measure the axial momentum distribution (by means of Bragg spectroscopy) to access the correlation function, this is instead given in the experiment of Ref. [95] by the contrast of the interference fringes as a function of the distance between the two interfering condensates. The experimental data (hollow red circles of Figure 6.1), show that, in the regime $T \simeq T_\phi$, the coherence extends over more than half of the system size.

In order to access such low values of T/T_ϕ, it was technically easier to use slightly *less* elongated traps than in [54]. In fact, two different trap configurations were used (first: $\omega_\perp = 2\pi \times 395$ Hz and $\omega_z = 2\pi \times 8.67$ Hz; second: $\omega_\perp = 2\pi \times 655$ Hz and $\omega_z = 2\pi \times 6.55$ Hz); the data obtained with the second trap were subdivided into two different blocks, characterised by two different values of the evaporation parameter, which proved necessary in order to vary T/T_ϕ, while keeping the condensed fraction fairly constant within each data block [199]. The *total* atom numbers measured in this experiment were found to lie in the range $0.8 \times 10^5 - 3 \times 10^5$ (corresponding quasi-condensate atom numbers: $0.5 \times 10^5 - 2.5 \times 10^5$), within a temperature region of $100 - 230$ nK.

Although it is theoretically anticipated (for a homogeneous gas [200]), that the coherence length, scaled to the experimental half-length of the system L, should yield a universal curve when plotted against the reduced temperature T/T_ϕ, it would not actually be appropriate to incorporate the data from [95] with the ones from [54] into a single graph; this is because the two experiments used different techniques to measure the coherence length and so their corresponding results should not be directly compared, a point that we discuss further in the next sections.

Table 6.1: Comparison between key points of the two experiments by Hugbart *et al.* [95] and Richard *et al.* [54].

	Experiment by Hugbart *et al.* [95] Chapter 6	Experiment by Richard *et al.* [54] Chapter 5
Parameters known from experiments:	$T, N_{\rm tot}, N_{\rm qc}, \omega_z, \omega_\perp$	$T, N_{\rm qc}, \omega_z, \omega_\perp$
Parameters calculated: *ab initio*	$L, L_{\rm c}, T_\phi[N_{\rm qc}]$	$L, L_{\rm c}, T_\phi[n_{\rm qc}(0)]$
Numerical Procedure:	Vary μ to match $N_{\rm tot}$ via Eqs. (3.28) and (3.29)	Vary μ to match $N_{\rm qc}$ via Eqs. (3.28) and (3.35)
Trap Configurations:	1) $\omega_z = 2\pi \times 8.67\,{\rm Hz}, \quad \omega_\perp = 2\pi \times 395\,{\rm Hz}$ 2) $\omega_z = 2\pi \times 6.55\,{\rm Hz}, \quad \omega_\perp = 2\pi \times 655\,{\rm Hz}$	$\omega_z = 2\pi \times 5\,{\rm Hz}, \quad \omega_\perp = 2\pi \times 760\,{\rm Hz}$
Number of data points:	22	7
Expression for T_ϕ:	$T_\phi[N_{\rm qc}] = 15\hbar^2 N_{\rm qc}/16 m k_B L^2$	$T_\phi[n_{\rm qc}(0)] = \hbar^2 n_{\rm qc}(0)/m k_B L$
Method to measure $L_{\rm c}$:	$C^{(1,{\rm mod})} = \langle \left\| F\left[\frac{\psi^*(-z/2)\psi(z/2)}{\|\psi(0)\|^2}\right]\right\| \rangle$	$C^{(1)} = \langle F\left[\frac{\psi^*(-z/2)\psi(z/2)}{\|\psi(0)\|^2}\right] \rangle$
Experimental Technique to extract $L_{\rm c}$:	Interferometric Method	Momentum spectroscopy
Temperature regime:	$0.8 < T/T_\phi < 8 \quad (90\,n{\rm K} \leq T \leq 350\,n{\rm K})$	$6 < T/T_\phi < 28 \quad (100\,n{\rm K} \leq T \leq 230\,n{\rm K})$
Atom number range:	$N_{\rm tot}:\ 0.8 \times 10^5 - 3 \times 10^5$	$N_{\rm qc}:\ 0.25 \times 10^5 - 0.65 \times 10^5$

The model used in [95] to predict the experimental findings follows the theory by Petrov *et al.* [32], which should be equivalent to the low temperature limit of the modified Popov theory [87]. It was found that the theoretical prediction for the coherence length was shifted with respect to the experimental one by about 25% for $T/T_{\phi} = 1$ [95]. This is clearly shown in Figure 6.1, where the theoretical prediction (solid red line) is found to lie above the experimental data points (hollow red circles).

6.2 Modelling of the experiment: Analysis via $C^{(1)}$

The procedure we adopt to model the experimental results of Ref. [95] differs slightly from the one used to reproduce the experiment of Ref. [54] in the previous chapter. This is so because for the experiment in [95], we have also access to the experimental data for the *total* atom number, and therefore we can closely follow the methodology described in Section 3.3, based on both Eq. (3.28) and Eq. (3.29) to account for the axial dynamics and the tranverse modes respectively, and solve Eq. (3.32). In particular, as the condition $\mu > \hbar\omega_{\perp}$ is fulfilled in Ref. [95] (unlike the experiments investigated in Chapter 4 for which $\mu < \hbar\omega_{\perp}$), we must also consider the effect of the mean-field potential experienced by the transverse thermal atoms (i.e. use Eq. (3.31), as explained in Section 3.3). We also remind the reader that the half-size of the quasi-condensate, L, is in our simulations the temperature dependent Thomas-Fermi radius, $R_{\mathrm{TF}}(T)$, calculated *ab initio*, as explained in Section 3.7.2.

In our simulations, rather than reproducing the experimental procedure, for which non-equilibrium expansion dynamics would need to be accounted for, we *initially* instead extract the corresponding *in situ* coherence length by adopting the same methodology described in Section 5.2, and applied to the experiment in [54]. This is done here in order to firstly explore whether our numerical results for the system of Ref. [95] also lie on the same 'universal' curve of Ref. [54] (dot-dashed black of Figure 5.5).

We indeed find that the new numerical points generated in this regime $T \sim \mathrm{few}\, T_{\phi}$ (filled black squares, Figure 6.1) lie on the same (dot-dashed black) curve provided by the fit in Figure 5.5, hence demonstrating the universal character of the coherence properties as numerical results obtained with different sets of trap configurations, temperatures and atom number yield the same behaviour. However, while our methodology led to a unified theoretical graph over both the 'weak' and 'strong' phase fluctuation regime, which also provides excellent

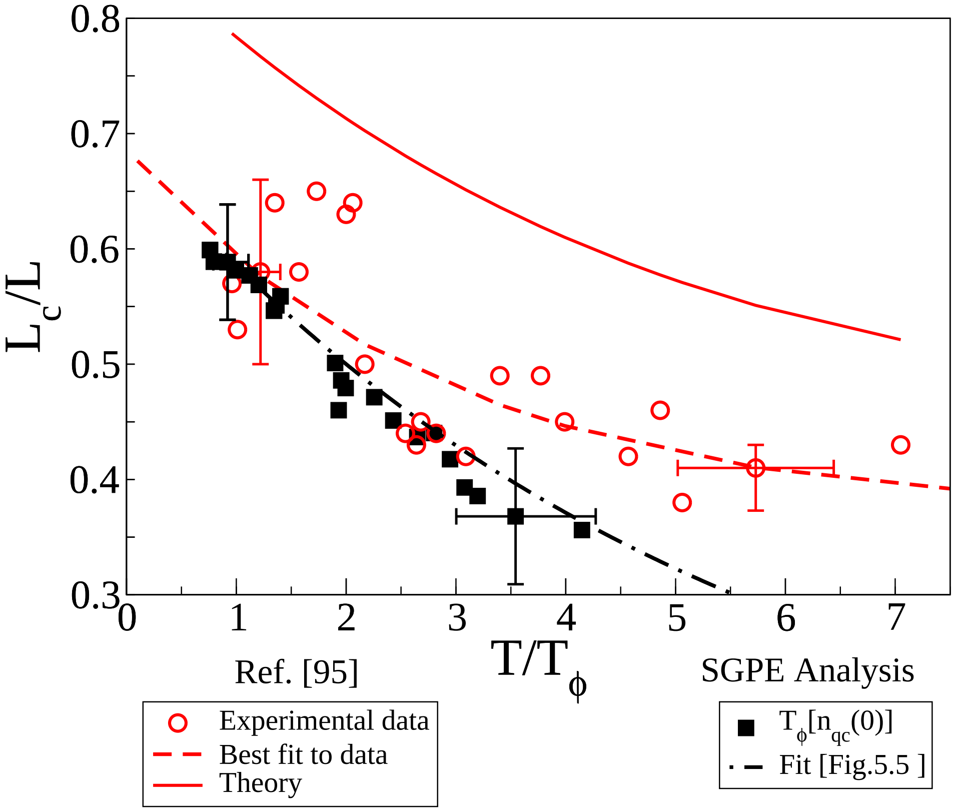

Figure 6.1: Scaled coherence length L_c/L vs. reduced temperature T/T_ϕ. Comparison of experimental data [95] (hollow red circles) to the SGPE model (filled black squares). The theory used in [95] to interpret the experimental data is also shown (solid red line), together with the reported experimental best fit (dashed red line). The fit from Figure 5.5 (dot-dashed black line) is also reported. Typical error bars are shown for corresponding data points in both experiment and SGPE model; in the latter case, they are based on a 20% variation on total atom number (note that the error bars to the point with $T/T_\phi \approx 1.2$ lies within the point size and are barely visible). The SGPE data are scaled to $T_\phi[n_{\rm qc}(0)]$ for consistency with the discussion of Figure 5.5.

agreement with the experiment [54] for $T > 6T_\phi$, the corresponding SGPE results for the experiment of Ref. [95] differ from the experimentally-reported ones. The reason for this discrepancy is twofold: firstly, in [95] it is an 'effective' correlation function that is evaluated, which leads to a different definition of the coherence length (Section 6.3); secondly, the theoretical values of T/T_ϕ do not span the same range as in the experiment (Section 6.3.2).

6.3 Effective correlation function

The main source of the observed discrepancy should be related to the experimental measurement of an 'effective' correlation function (see Eq. (9) in [95]), instead of the correlation $C^{(1)}$ measured in [54] and discussed thus far. In the experiment of Ref. [95], this effective correlation was introduced in order to eliminate the random phase caused by the shot to shot fluctuations of the global position of the contrast fringes; it was found that taking the absolute value of the Fourier transform of the fringe pattern before averaging achieved this aim (for a more detailed explanation see Section 4.2 in Ref.[95]), but modified the coherence length relative to that of $C^{(1)}$. For this reason, we should not expect the measurements from the two experiments to lie on the same curve, as they measure two different quantities.

In analogy to the method used in the experiment to extract the coherence length, we implement this feature by similarly taking the absolute value of the Fourier transform of $g^{(1)}$ from each individual run, before averaging over the different realizations of the noise; our effective correlation function, which we here call $C^{(1,\mathrm{mod})}$, takes the form:

$$C^{(1,\mathrm{mod})} = \langle \left| F\left[\frac{\psi^{*}(-z/2)\psi(z/2)}{|\psi(0)|^{2}} \right] \right| \rangle. \tag{6.1}$$

The effective correlation function is found to have similar behaviour to $C^{(1)}$, but it decays faster for values of momentum k near the half-width at half maximum (HWHM), thus resulting in larger values of the coherence length.

Figure 6.2 shows a comparison between $C^{(1)}$ (black) and $C^{(1,\mathrm{mod})}$ (red) for the case of $T/T_{\phi} = 2.2$. In the inset of Figure 6.2 we focus on the region around the HWHM, and notice that $C^{(1,\mathrm{mod})}$ indeed decays faster than $C^{(1)}$.

6.3.1 Results

We now discuss the effects of using $C^{(1,\mathrm{mod})}$ in order to extract the coherence length from the system. As already shown in Figure 6.2, the values of the coherence lengths are slightly higher if extracted with this methodology. This is shown in Figure 6.3, which compares the theoretical results to the experimental measurements using $C^{(1)}$ (black filled squares) and $C^{(1,\mathrm{mod})}$ (blue filled circles). Although we consciously do not exactly reproduce the experimental technique, the results obtained from the SGPE analysis of the 'effective' correlation function clearly show a very similar trend to the experimental findings over the probed regime; in particular, they tend to lie on the reported line of best fit of the experimental data (dashed-red line of Figure 6.1). We note that our calculation of $C^{(1,\mathrm{mod})}$ leads to a much improved agreement with the experimental data than the original theoretical analysis reported in [95] (solid red line, Figure 6.1), which

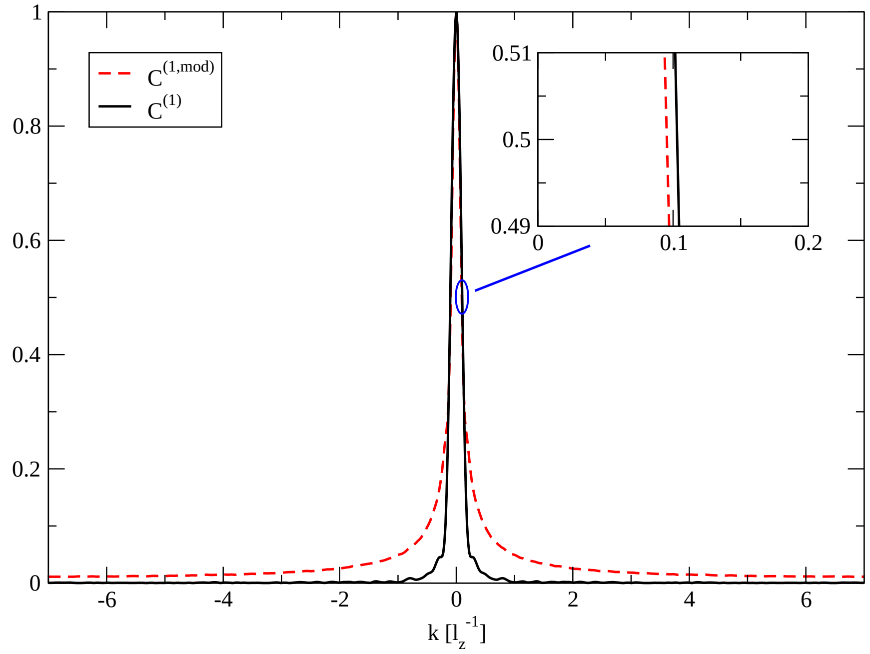

Figure 6.2: Comparison between $C^{(1)}$ (solid black) and $C^{(1,\text{mod})}$ (dashed red) at $T = 2.2T_\phi$. Inset: focus on the region around the half width at half maximum.

largely overestimates the amount of coherence in the system.

Although the experimental results and our simulated data (extracted via $C^{(1,\text{mod})}$) lie in the same region, the temperature regime spanned is still somewhat different: the experimental findings extend over slightly larger values of T/T_ϕ, as shown in Figure 6.3. This is motivated by the fact that we have used the definition for T_ϕ given in Ref. [54], which we have here labelled $T_\phi[n_{\text{qc}}(0)]$, in order to isolate the effect due solely to the extraction of the coherence length via $C^{(1,\text{mod})}$ instead of $C^{(1)}$; however in Ref. [95], the expression adopted for T_ϕ is different, and we address this issue in the next section with the intention to rule this out as the main source of the discrepancy.

6.3.2 Identification of T_ϕ

So far in our analysis we have always scaled our numerical results to $T_\phi[n_{\text{qc}}(0)]$, given by Eq. (5.1), which was correct when we compared to the experiment of Ref. [54].

However we note that the analysis of Ref. [95] was actually based on a *slightly*

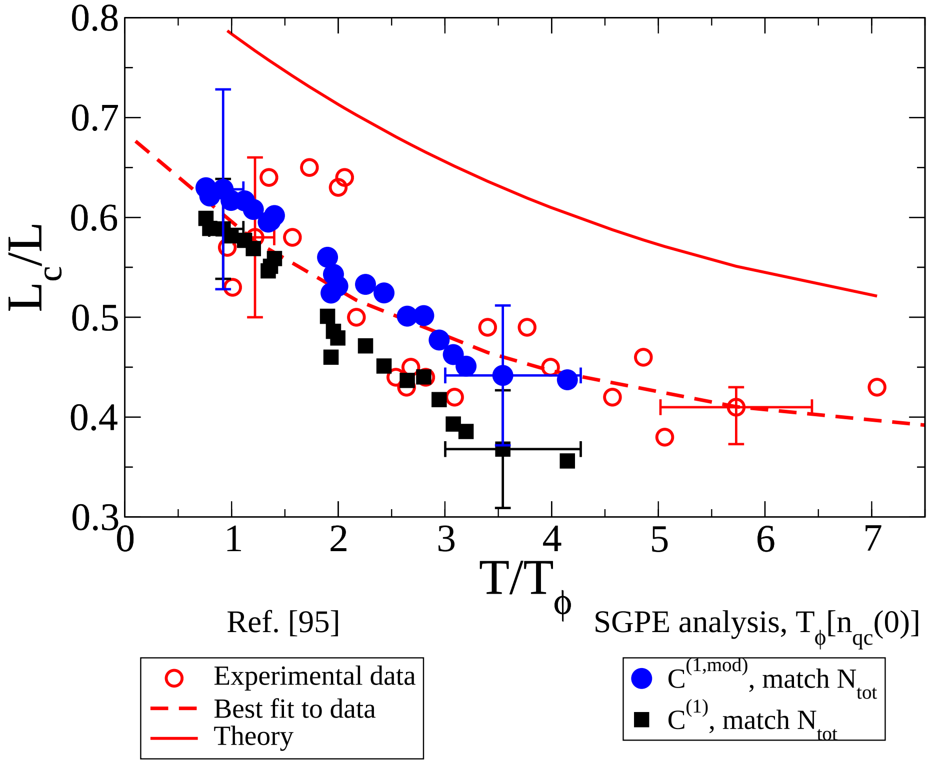

Figure 6.3: Scaled coherence length L_c/L vs. reduced temperature T/T_ϕ. Comparison of numerical SGPE data extracted via $C^{(1,\mathrm{mod})}$ (filled blue circles) and via $C^{(1)}$ (filled black squares) against experimental points of Ref. [95] (hollow red circles). The theory used in [95] is also shown (solid red line) together with the experimental best fit (dashed red line). SGPE data are scaled to $T_\phi[n_{\mathrm{qc}}(0)]$, and respective error bars account for 20% variation in total atom number and a further 5% variation in temperature.

modified definition for T_ϕ compared to that used in Ref. [54] (see Appendix B for details), thus making the comparison in Figures 6.1 and 6.3 not appropriate for the purpose of direct investigation of the experimental findings in Ref. [95]. Nonetheless we remark that this was done primarily to investigate whether our numerical results from the two different experiments lie on the same universal curve (Figure 6.1) and to isolate the effect due solely to the use of $C^{(1,\mathrm{mod})}$ instead of $C^{(1)}$ (Figure 6.3).

For a direct quantitative comparison to the experimental results, we should therefore scale our numerical results to the T_ϕ used in Ref. [95], which we here call $T_\phi[N_{\mathrm{qc}}]$:

$$T_\phi[N_{\mathrm{qc}}] = \frac{15\hbar^2 N_{\mathrm{qc}}}{16 m k_B L^2}. \tag{6.2}$$

There are two main features to underline with regard to the above expression. Firstly, $T_\phi[N_{\mathrm{qc}}]$ is defined in terms of the *number* of quasi-condensate atoms N_{qc}

(and not on the *peak quasi-condensate density*). This is in fact a simplified form of Eq. (5.1), valid for 3D condensates (i.e. condensates where the transverse density profiles can be well approximated by a Thomas-Fermi profile). A discussion about the relation between the two expressions for T_ϕ, and how it is possible to reconcile them is presented in Appendix B. Secondly, the half-size of the quasi-condensate L (appearing in Eq. (6.2)) has been approximated in Ref. [95](Figure 5) with the Thomas-Fermi expression $L = \sqrt{(2\mu_{\rm TF}/m\omega_z^2)}$, rather than the *actual* value measured in the experiments. The chemical potential $\mu_{\rm TF}$ is defined as

$$\mu_{\rm TF} = \frac{\hbar\overline{\omega}}{2}\left(\frac{15N_{\rm qc}a_{\rm s}}{\sqrt{\hbar/(m\overline{\omega})}}\right)^{2/5} \text{ and } \overline{\omega} = (\omega_z\,\omega_\perp^2)^{1/3}. \tag{6.3}$$

With that in mind, we have thus repeated our numerical analysis using as closely related a procedure as possible: in particular, to obtain T_ϕ in our simulations, we also used $L = \sqrt{(2\mu_{\rm TF}/m\omega_z^2)}$ in Eq. (6.2), with $N_{\rm qc}$, appearing in both Eqs. (6.2)–(6.3), obtained directly from our simulations via the equation to extract the quasi-condensate density (Eq. (3.35)). However, we point out that the half-size of the condensate L, to which the experimental coherence length $L_{\rm c}$ is scaled to, is indeed the one measured experimentally.

Our numerical results are shown in Figure 6.4, and reveal an improved agreement with the experimental data (with respect to Figure 6.3), as the temperature regime spanned is now closer to the experimental one.

Although the experimental results and our simulated points (extracted via $C^{(1,{\rm mod})}$) demonstrate very good agreement when accounting for their respective error bars, the experimental data still appear to systematically extend to slightly larger values of T/T_ϕ, as visible in Figure 6.4. This could be attributed either to a systematic shift in the experimental determination of T (e.g. arising in expansion imaging), which however increases with increasing T/T_ϕ ratio, or to the method by which the inputs to T_ϕ (e.g. $N_{\rm qc}$ and L) are extracted in the analysis. In the rest of the chapter we assume that this shift arises solely from the latter and attempt to further improve on the spanned range of T/T_ϕ.

6.4 Alternative approaches

6.4.1 T_ϕ extracted from the phase distribution

In this section we investigate an alternative method of reproducing the experimental results of Ref. [95] from an SGPE analysis. This method aims to improve

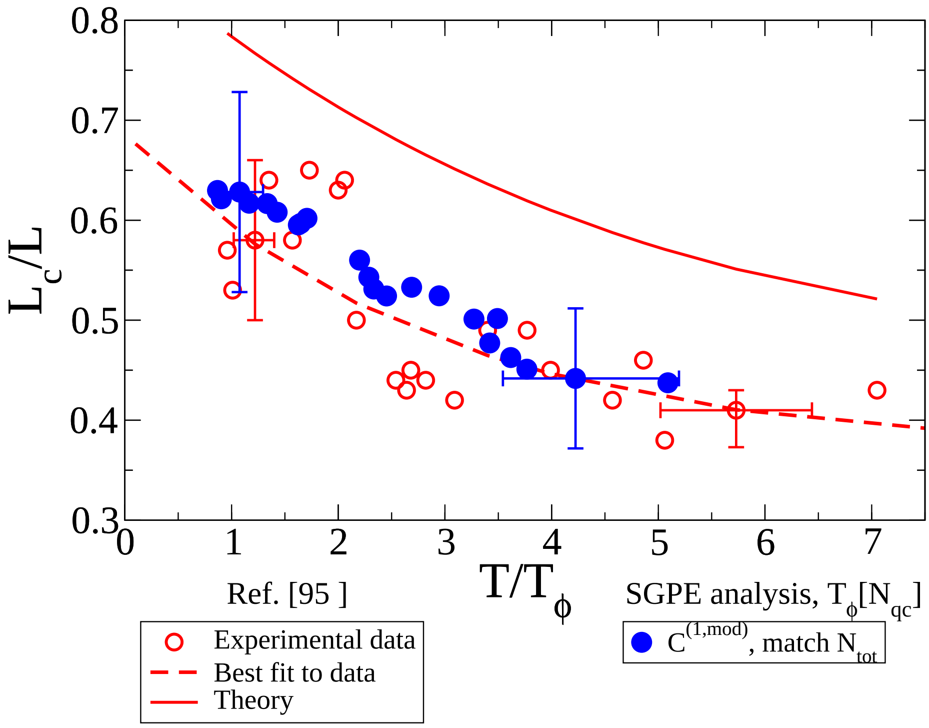

Figure 6.4: Scaled coherence length $L_{\rm c}/L$ vs. reduced temperature T/T_{ϕ}. Numerical SGPE findings extracted via $C^{(1,\rm mod)}$ (filled blue circles) against experimental data points of Ref. [95] (hollow red circles). The theory used in [95] is also shown (solid line) together with the experimental best fit (dashed red line). SGPE numerical points are scaled to $T_{\phi}[N_{\rm qc}]$, and respective error bars account for 20% variation in total atom number and a further 5% variation in temperature. SGPE results are obtained by matching the *total* number of atoms.

on the spanned regime of T/T_{ϕ} in our numerical simulations, but does not lead to any variation in the values of the reduced coherence length, $L_{\rm c}/L$. Our approach is motivated from footnote 47 of Ref. [95], which mentioned that T_{ϕ} could be obtained from the relation $L_{\phi}/L = T_{\phi}/T$ [32] with L_{ϕ} identified as the characteristic separation over which the phase fluctuates by 1 radian at the trap centre. This is directly related to the definition of T_{ϕ} given in Petrov *et al.* [32], where this is defined as the characteristic temperature at which $\delta_{\rm L}^2 \approx 1$, with $\delta_{\rm L}^2$ representing the phase fluctuations on a distance scale $|z - z'| \sim L$.

The parameters we need to extract to obtain the values for T/T_{ϕ}, according to the relation described above, are the half-size of the quasi-condensate L, which is still given by the temperature dependent Thomas-Fermi radius, and L_{ϕ}. To calculate the latter, we take here the approach of systematically analysing the phase distributions of the ensemble of stochastic fields ψ at several distances from

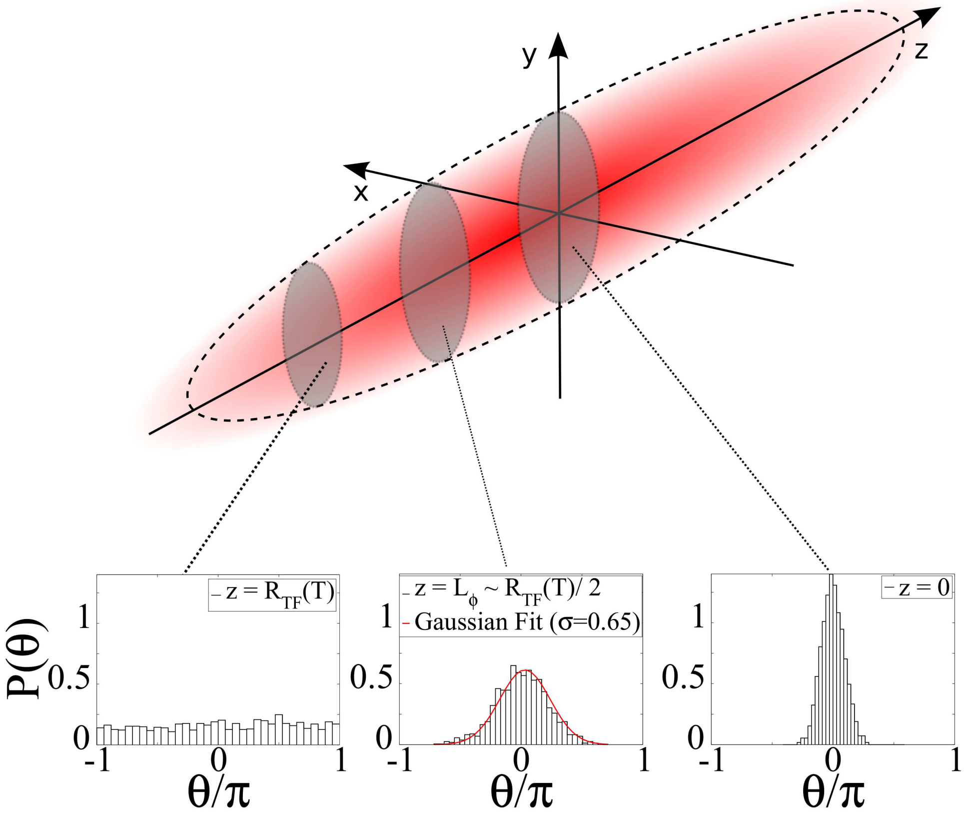

Figure 6.5: Distributions of the phase of $a_c^*\psi(z)/|a_c|$ (where a_c is the amplitude of the Penrose-Onsager mode), corresponding to the left data point with error bar in Figures 6.1 and 6.6, at different locations from the trap centre. Shown are the distributions at the condensate edge (left plot), at the point $z = L_\phi$ (central plot) where the distribution is fitted by a Gaussian (illustrated by the red solid curve) of standard deviation $\sigma = 0.65$ (which for the particular numerical point considered occurs at $z \simeq 0.5\,R_{\rm TF}(T)$) and at the trap centre $z = 0$ (right plot). The distributions are centered and normalised, and the phase θ is scaled to π.

the trap centre. Within the Thomas-Fermi radius, we find these distributions to be well fitted with Gaussian functions, whose standard deviation, σ, increases with increasing distance from the trap centre, due to the enhanced role of thermal fluctuations (see Figure 6.5 and related work in [92]).

In Figure 6.5 we report phase histograms of the stochastic field $\psi(z)$, locked to the phase of the Penrose-Onsager mode $\phi_{\rm PO}$ [167, 201], at three values of the distance from the trap centre. These phase distributions correspond to the left data point with error bar in Figures 6.1 and 6.6, for which $T = 2.2\,T_\phi[N_{\rm qc}]$.

To be more specific, we plot the phase, θ, of $a_c^*\psi(z)/|a_c|$:

$$\theta = \arctan\left(\frac{{\rm Im}[a_c^*\psi(z)/|a_c|]}{{\rm Re}[a_c^*\psi(z)/|a_c|}\right), \tag{6.4}$$

where a_c is the amplitude of the Penrose-Onsager mode, given by $a_c = \Delta z \sum_{z_i} \phi^*_{\rm PO}(z_i)\psi(z_i)$, and Δz is the grid spacing (see [167, 201] for further details and implementation). For each spatial point, z, there as many values of θ as number of stochastic realizations of ψ (i.e. 1200). In Figure 6.5 we show how these values are distributed at three different spatial points in the gas: $z = 0$ (right plot), $z \approx R_{\rm TF}/2$ (central plot), $z = R_{\rm TF}$ (left plot). We note that in the central region of the trap ($z = 0$), where the gas is more coherent, the phase θ takes on fewer values compared to the distribution at the edge of the trap ($z = R_{\rm TF}$), where θ is instead randomly distributed. This is shown by the plot of the histogram of the phase, that results in a narrow distribution at the center ($z = 0$), while a flat one at the edge ($z = R_{\rm TF}$). The broadness of the generated distributions is an indication of the amount of coherence at a specific spatial point in the system: we expect the distribution to become broader with increasing distance from the trap centre, and be almost flat at the edge, where the system becomes purely thermal (Figure 6.5).

In this analysis, L_ϕ can be identified as the distance from the centre where the standard deviation of the Gaussian fit to the phase distribution reaches a particular value. Our analysis indicates that when the standard deviation takes the value of $\sigma = 0.65$, then the corresponding value of L_ϕ leads to optimum agreement with the experimental findings regarding the spanned range of T/T_ϕ. For the specific data point considered in Figure 6.5, this occurs at $z \approx R_{\rm TF}/2$, so in this case we define $L_\phi = R_{\rm TF}/2$. It should be noted that the standard deviation, σ, in this approach plays the role of a *free* parameter, i.e. we choose the optimum value for it, which leads to best agreement with reported experimental data

The results of this approach are shown in Figure 6.6, where we show the simulated data scaled to the values of T/T_ϕ extracted as described above (blue stars) together with the experimental findings (hollow red circles). We also include here error bars for the previously considered indicative data points (as in Ref. [95]). In obtaining these we consider two sources of error: a variation in total atom number of 20% [202] and also a variation in the standard deviation σ of ± 0.05, to additionally indicate the sensitivity on this parameter. The individual error due to each of these contributions is shown by the solid and dashed portions of the error bars, respectively. Considering just the variation in atom number (solid portion of error bar), yields an error range which is very similar to the experimental range.

Overall, it is clear that the general trend in the theoretical values for T_ϕ is similar to the experimental values, suggesting that probing the phase distribution of the SGPE ensemble indeed captures, at least qualitatively, the temperature de-

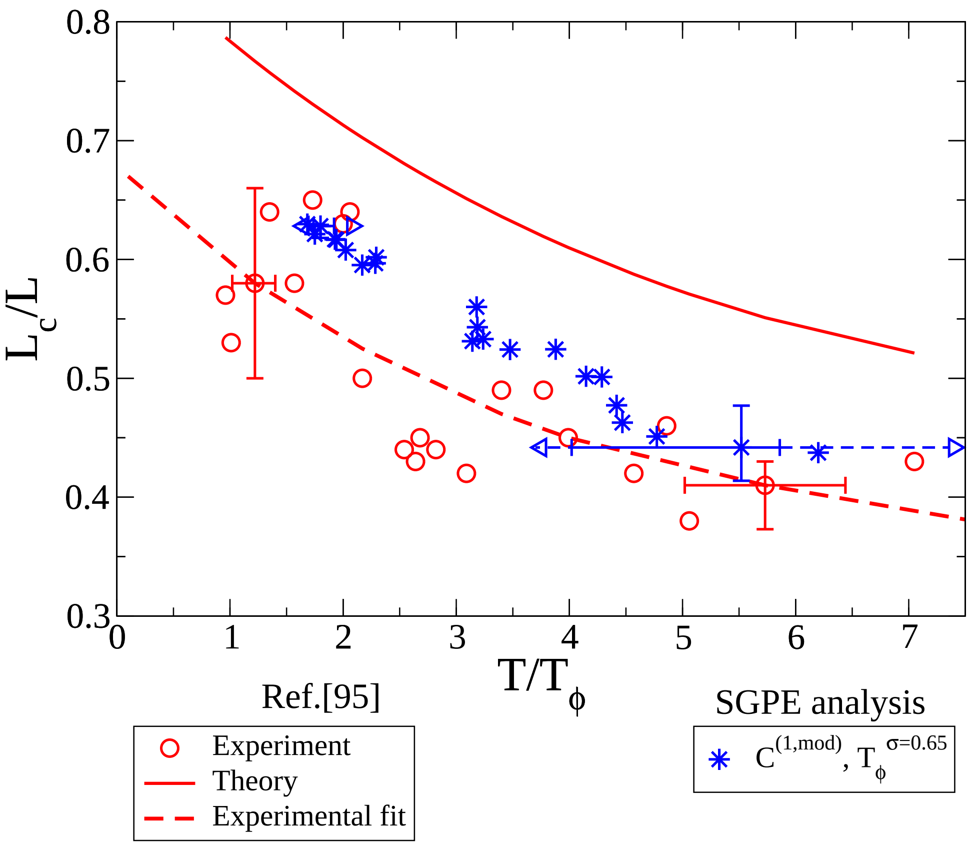

Figure 6.6: Scaled coherence length vs. reduced temperature. Experimental data [95] (hollow red circles) against SGPE numerical results extracted via $C^{(1,\mathrm{mod})}$ (blue stars) scaled to T_ϕ extracted from the phase distribution. The theory used in [95] is also shown (solid line) together with the best fit (dashed-red line). Error bars account for 20% variation on total atom number (solid line) and 8% variation on the standard deviation (dashed line).

pendent phase coherence observed in the experiment. Taking account of the error bounds suggests even quantitative agreement, since the experimental values of T/T_ϕ are within range of the theoretical values. We however stress further that this optimum agreement is the result of choosing an ad hoc value for the standard deviation (i.e.$\sigma = 0.65$), which is a free parameter in this approach.

6.4.2 Match quasi-condensate

The theoretical analysis discussed so far is based on matching the experimental total atom number, using both Eq. (3.28) and Eq. (3.29). However, the quasi-condensate atom number resulting from this approach and calculated as usual via Eq. (3.35), is systematically higher than the one extracted experimentally via bimodal fits.

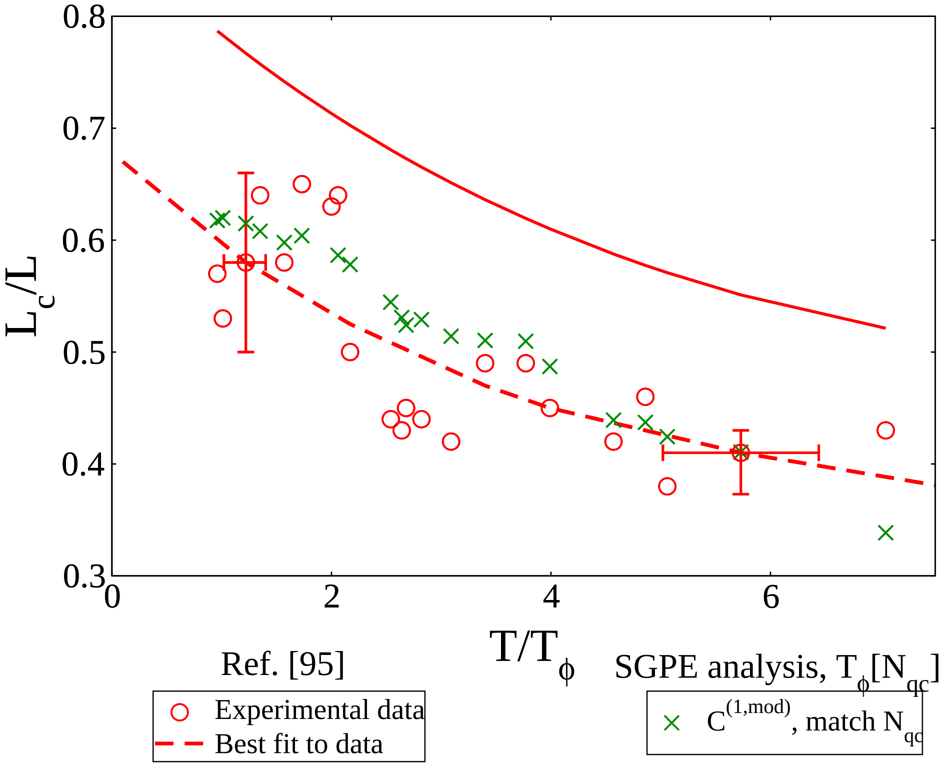

Figure 6.7: Scaled coherence length L_c/L vs. reduced temperature T/T_ϕ. Numerical SGPE data extracted via $C^{(1,\mathrm{mod})}$ (filled blue circles) against experimental points of Ref. [95] (hollow red circles). The theory used in [95] is also shown (solid red line) together with the experimental best fit (dashed red line). SGPE data are scaled to $T_\phi[N_{\mathrm{qc}}]$, and respective error bars account for 20% variation on total atom number. SGPE data shown here are obtained by matching the experimental *quasi-condensate* atom number.

For this reason we have performed a separate analysis, where we now match our numerically extracted *quasi-condensate* number to the corresponding experimentally extracted one. This is achieved by using only Eq. (3.28) (disregarding the contribution from the thermal atoms given by Eq. (3.29)), and extracting the quasi-condensate with Eq. (3.35). We remind that it was necessary to adopt such a method for the experiment in [54] discussed in Chapter 5, as in that case we had access only to the experimental quasi-condensate atom number.

The measurements of the coherence length are still performed via $C^{(1,\mathrm{mod})}$, and these are shown in Figure 6.7 (green crosses); we find very good overall agreement (except for the point with the highest T/T_ϕ), with the experimental findings (hollow red circles). We also notice that the regime of T/T_ϕ spanned by the SGPE numerical results matches the experimental one; this is what we would expect given that both the quasi-condensate number N_{qc} is the same between theory and experiment.

6.5 Chapter summary

In this chapter we have compared the SGPE theory to the findings of Hugbart *et al.*, Ref. [95] for the low temperature regime $T \lesssim \mathrm{few}\, T_\phi$, which is more challenging to probe in experiments. While the SGPE analysis gave a temperature dependence of the coherence length in quantitative agreement with the experimental trend (within error bars), undertaking a point-by-point analysis of the experimental data was found to span a slightly narrower range of T/T_ϕ than the experimentally-reported curve, indicating a systematic deviation. We argued that this discrepancy may arise as a result of the different identifications of T_ϕ between theory and experiment, possibly due to the different means of processing the 'raw' experimental data and stochastic numerical results, e.g. due to differences in extracting the quasi-condensate atom number which then feeds into the expression for T_ϕ.

We have partially examined this issue by using instead a phase sensitive means of extracting T_ϕ from characterisation of the ensemble phase distribution in SGPE simulations. In particular, motivated by footnote 47 of Ref. [95], we identified T_ϕ through the relation $T_\phi = T(L_\phi/R_{\mathrm{TF}}(T))$ where L_ϕ was chosen as the characteristic separation from the trap centre at which the phase distribution is fitted by a Gaussian with a particular value for the standard deviation. In our treatment however this value is a free parameter chosen here so as to match the experimental range of T/T_ϕ.

Chapter 7

Conclusions and future work

In this thesis we have demonstrated that the stochastic Gross-Pitaevskii equation (SGPE) is an excellent tool for *ab initio* modeling of equilibrium properties in weakly-interacting finite-temperature Bose gas experiments. The SGPE corresponds to a stochastic nonlinear Langevin equation which is essentially a dissipative Gross-Pitaevskii equation with an additional noise term. Unlike the Gross-Pitaevskii equation, where the wavefunction represents the condensate, in the SGPE the wavefunction can be thought of as the classical field associated with a set of highly populated low-lying modes in the gas (often referred to also as an 'order parameter'); these are in contact with the high-lying modes (i.e. thermal cloud), assumed to be at static equilibrium and to act as a particle reservoir (or 'heat bath'). The SGPE classical field therefore contains the condensate plus low-lying excitations on top of it; the damping term accounts for particle exchange between the two subsytems (i.e. low-lying modes and high-lying purely thermal cloud), while the noise term accounts instead for fluctuations due to such ongoing particle exchange; the latter is assumed to be Gaussian correlated. The damping term and the noise term, describe respectively, the coherent and incoherent scattering processes that occur between the low-lying modes, treated dynamically via the SGPE, and the high-lying modes, assumed to be close to equilibrium. Unlike the mean-field theories, reviewed at the start of Chapter 2, in which the existence of a well defined mean-field quantity is assumed at the start, the SGPE can describe spontaneous initiation, i.e. the growth of a condensate from a purely thermal cloud with a fixed chemical potential and temperature. The equilibrium state is reached in a dynamical manner: the growth is initiated by the noise term via spontaneous scattering, and then stimulated processes, due to bosonic enhancement, lead to the correct equilibrium configuration, ensured by the fluctuation-dissipation relation, which provides a precise relation between the dissipation and the fluctuations at equilibrium.

An interesting aspect of the SGPE is that is shares, in some sense, two features with the procedure adopted in the experiments. In a typical experiment, repeated tests are performed, with related shot-to-shot variations in the experimental realisations, over which the physical observables are finally averaged. In the same way, each stochastic run of the SGPE can be loosely associated to an independent experimental measurement, and the process of averaging over the several realisations of the noise finally leads to a physical observable that can be directly compared to the averaged experimental result. Furthermore, the atomic density distributions measured in the experiments, as well as the density profiles resulting from the solution of the SGPE, require additional analysis to identify the phase coherent ('pure' condensate) and density coherent (quasi-condensate) fraction from the total density. While in the experiments this is usually performed via bimodal fits (something which could also be imposed on the SGPE averaged results), we showed in Chapter 3 that knowledge of first- and second- order correlation functions are sufficient to extract these components from the total density profile.

7.1 Quasi-one-dimensional systems

The SGPE is particularly suitable for modelling weakly-interacting Bose gases in elongated geometries. In low-dimensional systems in fact, fluctuations play a major role, due to long-wavelength excitations in the harmonic trap, that tend to prevent the onset of off-diagonal long-range order in the gas. A mean-field model would not be adequate to describe the system, in this physical regime, due to the lack of a well-defined mean-field quantity. The 'order parameter' in the SGPE instead explicitly retains fluctuations around the mean-field, thus giving access to information on coherence, through calculations of correlation functions.

In order to best consider actual experimental data for quasi-1D systems, we have adopted an effective one-dimensional model which consists of a quasi-one-dimensional form of the SGPE, that further accounts for the transverse swelling of the gas due to repulsive interactions. The physical regime of the experimental data investigated in this thesis are in fact characterised by the conditions $\mu, k_{\rm B}T \lesssim \text{few}\, \hbar\omega_\perp$, where μ is the chemical potential, $k_{\rm B}T$ is the thermal energy, and $\hbar\omega_\perp$ is the tranvserse excitation energy. In addition to the quasi-1D SGPE, that describes the dynamics of the axial modes in the system, we also accounted in our model for the fact that the transverse excited modes are also populated:

- In the regime $\mu < \hbar\omega_\perp$, characteristic of the experiments analysed in Chapter 4, this is attained by treating each transverse mode as 1D independent *ideal* Bose gas at equilibrium.
- In the regime $\mu \sim \text{few}\,\hbar\omega_\perp$, characteristic of the experiments discussed in Chapters 5-6, we also accounted for the mean-field experienced by the transverse thermal atoms.

We now summarise the main results achieved in Part III of this thesis.

7.1.1 $\mu \lesssim \hbar\omega_\perp$ and $k_\mathrm{B}T \sim \text{few}\,\hbar\omega_\perp$

Density profiles

In Chapter 4 we compared our model to the experiments by Trebbia *et al.* [59] and van Amerongen *et al.* [60], in the groups of I. Bouchoule and N. J. van Druten respectively. These experiments studied a quasi-one-dimensional Bose gas realized on atom chips, at the crossover between the classical and quasi-condensate regime (with $\mu < 0$ or $\mu < \hbar\omega_\perp$ throughout all data considered for both experiments, see Fig. 1.1).

The work of Trebbia *et al.* [59] was the first experimental evidence of the breakdown of the Hartee-Fock (mean-field) approach in an elongated weakly-interacting Bose gas, as this approach cannot correctly predict the arising quasi-condensate due to its built-in inadequate handling of density fluctuations. The quasi-1D SGPE equation, supported by a static treatment of the transverse modes, was instead demonstrated to provide excellent agreement with the atomic density profiles at all temperatures, even at the critical crossover regime, where mean-field models are inadequate.

The work by van Amerongen *et al.* [60] provided the first comparison of the exact Yang-Yang thermodynamic solution to the one-dimensional Bose gas to experiments. The experimental *in situ* density profiles were found to be fully reconstructed by the modified Yang-Yang model (which also accounts for static transverse excited thermal modes). We probed the validity of our stochastic model against such results and found that our results accurately matched the experimental findings. This also allowed us to indirectly claim a favourable (practically exact) comparison between our model and the exact Yang-Yang thermodynamics.

Density fluctuations

In Chapter 4 we also showed that the quasi-1D SGPE model is an excellent tool for *ab initio* reproduction of density fluctuations in the work by Armijo *et al.* [61] (in the regime $\mu < \hbar\omega_\perp$). This was achieved by mimicking the experimental procedure as closely as possible, exploiting the analogy between a single numerical run in the SGPE and a single experimental realization (under the general understanding that results in both cases are then to be averaged over an ensemble of different 'runs'). The SGPE predictions were found to match pretty well the experimental results, and also improved on the theory reported in Armijo *et al.* [61], which had only actually been applied for the purely 1D equation of state. Moreover, the SGPE results provided a smooth crossover between the ideal Bose gas and the quasicondensate regimes, showing very good agreement with the mean-field results valid in the appropriate limits.

7.1.2 $\mu, k_\mathrm{B}T \sim \text{few}\, \hbar\omega_\perp$

Phase fluctuations

In Chapters 5 and 6 we have investigated the independent experiments by Richard *et al.* [54] and Hugbart *et al.* [95] which studied the phase properties of a weakly-interacting Bose gas in 3D elongated geometry, in the 'strong' and 'weak' phase fluctuating regime.

While in Richard *et al.* [54], an experimental technique based on Bragg spectroscopy was used to measure the axial momentum distribution of the gas, in the experiment by Hugbart *et al.* [95], they looked at the contrast of intereference fringes after the condensate had initially split. The use of two different experimental techniques led to a slight different definition for the coherence length, an issue that we had to take into account when we modelled the experimental results.

Our *ab initio* study of these two experiments aimed to investigate the reduced coherence length as a function of the temperature. The coherence length was extracted from the average of the Fourier transform of the correlation function in the experiment by Richard *et al.* [54]. We then used a different approach, in analogy to the procedure adopted in the experiment by Hugbart *et al.* [95], and accessed the information about coherence length by averaging over the absolute values of the correlation functions. The size of the quasi-condensate in our model is calculated *ab initio*, by extending, in a somewhat heuristic manner, the criterion adopted in the modified Popov theory, to the context of SGPE. We undertook a point by point analysis, and found our predictions to be in excellent agreement with the experiment by Richard *et al.* [54]. The prediction of our model were also in very good overall quantitative agreement with the experimental findings in Hugbart *et al.* [95]; however our numerical results were found to span a sligthly smaller regime in T/T_ϕ. This issue was further discussed and an alternative approach, based on examining the phase distributions in our stochastic treatment, was put forward and shown to further improve the agreement with the experimental regime of T/T_ϕ (but now at the expense of introducing a free parameter into the system).

7.2 Final comments

The detailed study of these 5 experiments within a completely *ab initio* model proposed in this thesis confirms the excellent predictive power of the SGPE, at least for equilibrium results for weakly-interacting elongated Bose gases in the 1D and quasi-1D regime. In addition to reproducing the experimental results within a completely new model, which also enables the dynamical study of such properties, we also:

- improved on the values of the chemical potentials in the experiment of Trebbia *et al.* [59], by using an improved model to extract these compared to that used in the original publication;
- showed (indirectly) the consistency of the model presented in this thesis (upon replacing the quasi-1D SGPE with the simpler 1D SGPE) to the modified 1D Yang-Yang model used to interprete the results in the experiment by van Amerongen *et al.* [60] and Armijo *et al.* [61];
- showed that we can fully recover the entire crossover between different mean-field results (ideal gas, quasi-condensate) in the context of density fluctuations in the experiment by Armijo *et al.* [61], done only partially in the original publication;
- demonstrated for the first time the temperature dependence of the scaled coherence length from fully *ab initio* considerations for the experiment of Richard *et al.* [54] conducted in the 'strong' phase fluctuation regime (previous successful analysis relied actually on partial experimental input into the corresponding zero-temperature theory);

- provided the first ever quantitatively correct analysis of the corresponding experiment by Hugbart *et al.* [95] in the 'weak' phase fluctuation regime (previously semi-phenomenological analysis had significantly overestimated the actual value of the coherence despite correctly reproducing the overall trend);
- demonstrated the full consistency of the results in the two latter experiments by carefully reanalysing them theoretically in an identical manner (as the experiments actually used slightly different techniques to extract the coherence length) and showing how they can coexist on a single universal curve (the latter point is best visualized in Figure 7.1).

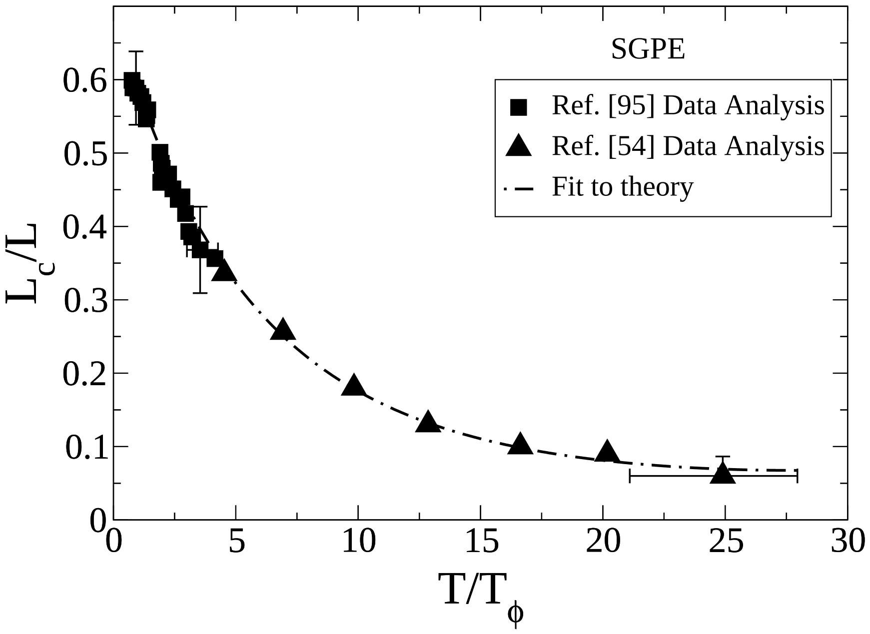

Figure 7.1: Scaled coherence length vs. reduced temperature for the experiments by Richard *et al.* [54] (triangles) and Hugbart *et al.* [95] (squares) when reanalysed in an *ab initio* manner by the quasi-1D SGPE based on an identical analysis corresponding to the one used in Richard *et al.* [54], namely extracting the coherence length via $C^{(1)}$ (Eq. (5.3)), and using the expression $T_\phi[n_{\rm qc}(0)]$ of Eq. (5.1). Shown is also the theoretical fit from Figure 5.5.

7.3 Future work

7.3.1 System of coupled equations

The *ab initio* investigation of five experiments discussed in Part III, is based on the self-consistent model explained in Section 3.3. This model consists of an equation (i.e. quasi-1D SGPE) that solves the dynamics of the axial modes of the system, whereas the transverse excited modes are treated statically, as independent Bose gases. While in the regime $\mu < \hbar\omega_\perp$ we treat the transverse excited modes as ideal Bose gases, in the regime where $\mu > \hbar\omega_\perp$ (occurring in the experiments by Richard *et al.* [54] and Hugbart *et al.* [95]), we have also accounted for the effect of the mean-field potential experienced by the transverse thermal atoms. However, given that the contribution from the density of transverse thermal atoms is relative low (compared to the axial density), we do not include the mean-field contribution due to these atoms within the non-linearity in the SGPE.

Such a contribution has already been explicitly included in the context of two-dimensional SGPE in the work of Cockburn *et al.* [164], where it was found to have a negligible effect. Although we do not anticipate a noticeable discrepancy, we aim to investigate the effect arising by solving the two equations of the model presented here in a coupled manner, whereby one also includes the contribution of the density due to the thermal atoms, into the non-linearity of the SGPE. This should amount to perform the following replacement in the quasi-1D SGPE:

$$\hbar\omega_\perp\big[\sqrt{1+4|\psi|^2 a_\mathrm{s}}-1\big] \to \hbar\omega_\perp\big[\sqrt{1+4(|\psi|^2+n_\perp)a_\mathrm{s}}-1\big] \tag{7.1}$$

The quasi-1D SGPE, upon making this replacement, would then be coupled to the equation for the transverse excited modes, which we report here:

$$n_\perp(z;\mu,T) = \frac{1}{\lambda_\mathrm{dB}}\sum_{j=1}^{\infty}(j+1)g_{1/2}(e^{\mu-V(z)-j\hbar\omega_\perp-2g_{1d}(|\psi|^2+n_\perp)/k_BT}) \tag{7.2}$$

While we do not expect the equilibrium properties calculated in this work to be affected by such replacement, we believe this could provide further consistency to the model.

7.3.2 Temperature dependent Thomas-Fermi radius

One of the novel features of the model introduced in this thesis is the possibility to calculate a parameter referred to as the temperature-dependent Thomas-Fermi radius, $R_{\mathrm{TF}}(T)$, which roughly speaking gives the size of the quasi-condensate

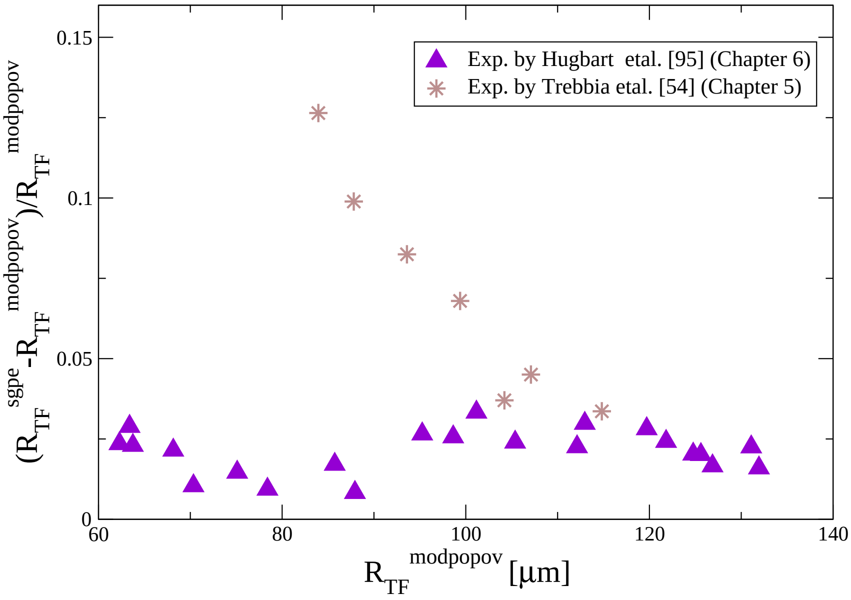

Figure 7.2: Relative difference between the values of the temperature dependent Thomas-Fermi radius calculated within SGPE, $R_{\mathrm{TF}}^{\mathrm{sgpe}}(T)$, and those obtained via modified Popov theory $R_{\mathrm{TF}}^{\mathrm{modpopov}}(T)$ for the same set of parameters, taken from the experiment of Richard *et al.* [54] (brown stars) and Hugbart *et al.* [95] (violet triangles).

at finite temperature. This was achieved by extending, in a somewhat heuristical manner, the criterion to establish the size of the quasi-condensate within the modified Popov theory, to the SGPE case (see Section 3.7.2 for details). This relies on the agreement between the density profiles calculated via the SGPE and the modifed Popov method, that has been demonstrated in Refs. [90, 167].

Figure 7.2 shows the relative difference between the values of $R_{\mathrm{TF}}(T)$ calculated within SGPE and those obtained via modified Popov theory for the same set of parameters. The values of $R_{\mathrm{TF}}(T)$, obtained via the SGPE method, show good agreement with those extracted via the modified Popov theory, up to a ~ 10 percentage error for most of the data considered (see Fig. 7.2). However this is true for the data of the experiments by Richard *et al.* [54] (brown stars, Fig. 7.2) and Hugbart *et al.* [95] (violet triangles, Fig. 7.2), in which specific values for temperatures, atom number and trap geometry have been used. It would be interesting however to further probe this agreement, by performing a systematic check, in order to investigate the regime of validity of this criterion within the SGPE theory. Furthermore, an *a priori* derivation of such a criterion within the SGPE theory is also the aim of our future work.

7.3.3 Investigating the limits of validity of the quasi-1D SGPE

Experiments with very elongated geometries (i.e. the system is transversely in the ground state), and appropriately engineered densities and temperatures to be in the weakly-interacting regime, may be well described by the 1D Stochastic Gross-Pitaevskii equation (SGPE) [116, 117, 139], since transverse thermal modes remain sparsely occupied for μ, $k_B T \ll \hbar\omega_\perp$ (although recent experiments suggest that quasi-1D effects play a role even for quite low densities [91]). The method applied here provides a novel means to self-consistently model experiments which fall within the intermediate regime, where $\mu, k_B T \lesssim \text{few}\ \hbar\omega_\perp$. In particular, the role of the quasi-1D non-linearity introduced in the SGPE was motivated by the condition that μ is not much smaller than $\hbar\omega_\perp$, and consequently it is necessary to use a model able to capture the effect of swelling of the system over the transverse direction, which is due to the increasing interactions in the centre of the cloud. This equation was then applied in this work in a regime where μ never takes values larger than $7\hbar\omega_\perp$ (see Figure 1.1). However we also wish to probe the quasi-1D SGPE model in systems where μ becomes bigger than $7\hbar\omega_\perp$, in order to investigate the regime where this model eventually breaks down.

However we anticipate that the regime of validity is however limited by the assumption that the transverse profile is a Gaussian distribution with width equivalent to $\sigma^2 = l_\perp^2\sqrt{1 + 4a_\mathrm{s}N|f|^2}$. This suggests that when the system enter the Thomas-Fermi regime transversally, this assumption is no longer correct, and one has to resort to a full three-dimensional model.

7.4 Dynamical study

The work undertaken throughout this thesis is based on modelling *equilibrium* properties measured in quasi-one-dimensional Bose gas experiments. This allowed to establish that the SGPE is an excellent model for reproducing experimentally measured observables, such as density profiles, density and phase fluctuations.

Once this model has been tested at equilibrium, it is desirable to probe it for studying dynamics that perturb the system about equilibrium. One of the first interesting test is to study the expansion dynamics over the axial direction: essentially once the system has relaxed to equilibrium, one removes the potential along the axial direction, leading the system to expand along the axial direction. It is interesting to notice that, for the typical trap configuration of the experiments modelled in this thesis, the axial potential is quite shallow, thus implying that the cloud hardly expands axially beyond its initial length. An experimental technique, referred to as *condensate focusing*, is used as an expedient to solve this problem; this consists in applying a short strong axial harmonic potential which practically induces the atoms to expand over the axial direction. Such a technique has been already implemented within the SPGPE formalism in [193], and we also aim to realise this within the SGPE model too.

However, in order to study expansion dynamics, it would also be necessary to amend the static treatment of the transverse excited modes, by adopting a kinetic approach to describe the dynamics of the high-lying modes (with energy $k_{\mathrm{B}}T > \hbar\omega_{\perp}$).

Prethermalization in 1D Bose gas

In Chapter 6 we have described and used a method, which is based on the analysis of phase histograms in our stochastic treatment, to partially resolve an issue related to the spanned range of the values of T/T_{ϕ}, when modelling the experiment of Hugbart *et al.* [95]. In particular, the phase histograms calculated with this method contain informations about the coherence properties of the system. Motivated by the experiment of Gring *et al.* [203], in which a one-dimensional condensate was initially coherently split and its relaxation dynamics studied by means of matter-wave interferometry, we believe that the possibility to compute phase histograms in our model could be adopted when studying such physical systems. In particular, by investigating the contrast of the fringes formed after the two copies of the initial condensate overlap, one could gain information on the state of the system. In [203] it was found that the gas relaxed to a steady state which did not correspond to the thermal equilibrium.

Appendix A

Quantum-Boltzmann equation

The evolution of the high-lying modes (i.e thermal cloud) in the system is described by the following Quantum-Boltzmann equation [116]:

$$\frac{\partial N}{\partial t} + (\boldsymbol{\nabla}_{\boldsymbol{p}}\, \epsilon) \cdot (\boldsymbol{\nabla}_{\boldsymbol{r}}\, N) - (\boldsymbol{\nabla}_{\boldsymbol{r}}\, \epsilon) \cdot (\boldsymbol{\nabla}_{\boldsymbol{p}}\, N) = C_{12}[N] + C_{22}[N], \tag{A.1}$$

where $N = N(\mathbf{p}, \mathbf{r}, t)$ denote the thermal population in each mode.

The collisional integrals are given by:

$$\begin{aligned} C_{12}[N] = \frac{4\pi}{\hbar} g_{3d}^2 |\psi|^2 \int \frac{d\mathbf{p}_2}{(2\pi\hbar)^3} \int \frac{d\mathbf{p}_3}{(2\pi\hbar)^3} \int \frac{d\mathbf{p}_4}{(2\pi\hbar)^3} \\ \times (2\pi\hbar)^3 \delta(\mathbf{p}_2 - \mathbf{p}_3 - \mathbf{p}_4) \times \delta(\boldsymbol{\epsilon_c} + \boldsymbol{\epsilon}_2 - \boldsymbol{\epsilon}_3 - \boldsymbol{\epsilon}_4) \\ \times (2\pi\hbar)^3 [\delta(\mathbf{p} - \mathbf{p}_2) - \delta(\mathbf{p} - \mathbf{p}_3) - \delta(\mathbf{p} - \mathbf{p}_4)] \\ \times [(N_2 + 1) N_3 N_4 - N_2 (N_3 + 1)(N_4 + 1)] \end{aligned} \tag{A.2}$$

and

$$\begin{aligned} C_{22}[N] = \frac{4\pi}{\hbar} g_{3d}^2 \int \frac{d\mathbf{p}_2}{(2\pi\hbar)^3} \int \frac{d\mathbf{p}_3}{(2\pi\hbar)^3} \int \frac{d\mathbf{p}_4}{(2\pi\hbar)^3} \\ \times (2\pi\hbar)^3 \delta(\mathbf{p} + \mathbf{p}_2 - \mathbf{p}_3 - \mathbf{p}_4) \times \delta(\boldsymbol{\epsilon} + \boldsymbol{\epsilon}_2 - \boldsymbol{\epsilon}_3 - \boldsymbol{\epsilon}_4) \\ \times [(N + 1)(N_2 + 1) N_3 N_4 - N N_2 (N_3 + 1)(N_4 + 1)]. \end{aligned} \tag{A.3}$$

The term C_{12} describes the exchange of atoms between the low-lying modes and the high-energy part (i.e. thermal cloud). In particular C_{12} accounts for collisional processes describing the transfer of a thermal atom into the low-lying modes of the system ($(N_2+1)N_3N_4$) and its inverse process, involving the scattering of an atom from the low-energy part into the thermal cloud ($N_2(N_3+1)(N_4+$

$1)$). The term C_{22} accounts instead for collisional processes between two thermal atoms, which lead to a redistribution of the thermal population in the thermal modes. The presence of the delta functions ensures the momentum and energy conservation, hence the collisional processes are elastic.

The above collisional terms have a very similar, but distinct form, to those used in the Zaremba-Nikuni-Griffin approach discussed in Section 2.3.1. However we point out that a crucial difference between the two approaches is that while in the ZNG approach the wavefunction ϕ is associated to the condensate only, here the field ψ describes a set of highly populated low-lying modes.

Appendix B

Comparison of expressions for T_ϕ

In the experiment by Richard *et al.* of Ref. [54] the expression used for T_ϕ is:

$$T_\phi[n_{\rm qc}(0)] = \frac{\hbar^2 n_{\rm qc}(0)}{m k_B L}, \tag{B.1}$$

where $n_{\rm qc}(0)$ is the quasicondensate peak density and L the half-size of the quasicondensate. This corresponds to the most general expression, and only requires the Local Density Approximation to hold, as demonstrated in [101].

However numerous different, practically equivalent, definitions of T_ϕ have been put forward in the literature (e.g. [31, 32]). In particular the experiment by Hugbart *et al.* [95] uses an alternative definition of T_ϕ, based on the *number* of quasicondensate[1] atoms $N_{\rm qc}$ (and not on the *peak quasicondensate density*). In [95], the expression used is

$$T_\phi[N_{\rm qc}] = \frac{15\hbar^2 N_{\rm qc}}{16 m k_B L^2}. \tag{B.2}$$

The expression for $T_\phi[N_{\rm qc}]$ is derived by assuming a 3D density profile in harmonic trap at $T = 0$ (i.e. Thomas-Fermi approximation).

The two above expressions are identical in the region where Eq. (B.2) is supposed to be used [204]. To demonstrate this, we consider the density profile of a 3D Bose gas confined in an elongated cylindrical harmonic trap, at T=0 (within the Thomas-Fermi approximation) [32]:

$$n(r, z) = \frac{\mu}{g_{\rm 3D}}\left(1 - \frac{z^2}{L^2} - \frac{r^2}{R^2}\right). \tag{B.3}$$

Here z and r are the axial and radial coordinate, while $L = \sqrt{(2\mu/m\omega_z^2)}$ and

---

[1] We should clarify that here we use the term 'quasicondensate' to refer to the 'condensate' component described in [95].

$R = \sqrt{(2\mu/m\omega_r^2)}$ represent the half-size of the condensate in the axial and radial direction respectively. By integrating transversally over the radial coordinate and evaluating the density profile at $z = 0$, we obtain:

$$n_{\rm qc}(z)|_{z=0} = \int_0^R d^2r\, n(r,z) = \frac{\mu\pi R^2}{2g_{\rm 3D}}. \tag{B.4}$$

By replacing the above result (B.4) in the formula for the number of condensed atoms $N_{\rm qc} = 8\pi\mu R^2 L/15 g_{\rm 3D}$ [32, 127], we obtain an expression which relates the central peak density $n_{\rm qc}(0)$, the axial half-length L and the number of condensed atoms N_0, given by:

$$n_{\rm qc}(0) = \frac{15}{16}\frac{N_{\rm qc}}{L}. \tag{B.5}$$

The above relation shows that in the $T = 0$ limit, under the Thomas-Fermi approximation, the two definitions for T_ϕ are equivalent.

This similarity is explicitly demonstrated in Figure B.1, where scaling our numerical results extracted via $C^{(1)}$, to $T/T_\phi[n_{\rm qc}(0)]$ (filled black squares) or $T/T_\phi[N_{\rm qc}]$ (filled brown squares) leads to very little difference in our theoretical results. However we note there is no exact agreement between the numerical results obtained by using the two definitions of T_ϕ, because of deviations from the Thomas-Fermi approximation, in particular at relatively high T/T_ϕ [204].

Note that the consistency of these two different definitions in the regime of the experiment of Hugbart *et al.* [95] rules out the possibility that the difference in values of T/T_ϕ in Section 6.3.1 are due to this.

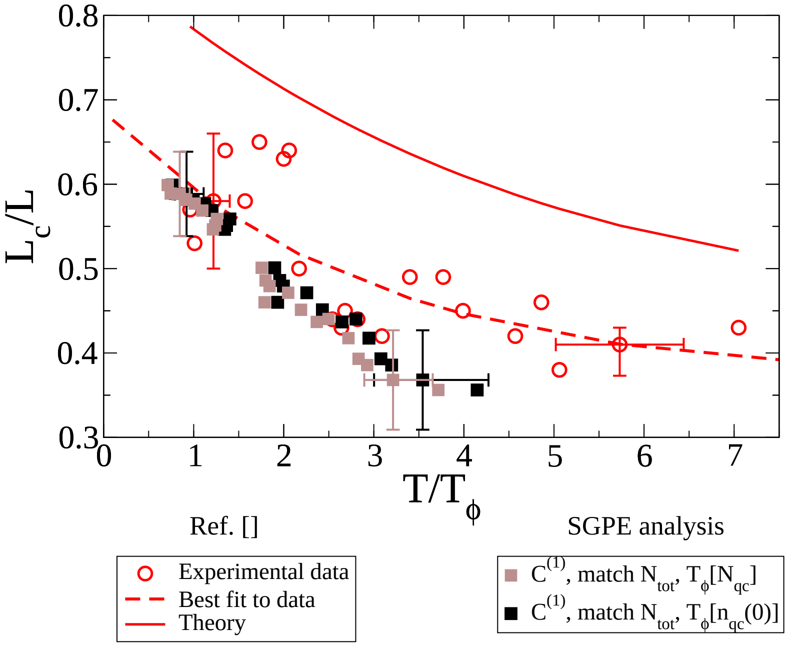

Figure B.1: Scaled coherence length L_c/L vs. reduced temperature T/T_ϕ. Comparison between SGPE numerical results extracted via $C^{(1)}$, scaled to $T/T_\phi[n_{qc}(0)]$ (filled black squares) and $T/T_\phi[N_{qc}]$ (filled brown squares). The experimental data points of [95] (red circles), the theory to interpret the experimental data in [95] (solid red line) and the reported experimental best fit (dashed red line) are also shown.

Bibliography

[1] S. N. Bose, Z. Phys. **26**, 178 (1924).

[2] A. Einstein, Sitzber. Kgl. Preuss. Akad. Wiss. **23**, 3 (1925).

[3] E. A. Cornell and C. E. Wieman, Rev. Mod. Phys. **74**, 875 (2002).

[4] F. London, Nature **141**, 643 (1938).

[5] P. Kapitza, Nature **141**, 74 (1938).

[6] J. F. Allen and A. D. Misener, Nature **141**, 75 (1938).

[7] C. E. Hecht, Physica **25**, 1159 (1959).

[8] W. C. Stwalley and L. H. Nosanow, Phys. Rev. Lett. **36**, 910 (1976).

[9] I. F. Silvera and J. T. M. Walraven, Phys. Rev. Lett. **44**, 164 (1980).

[10] M. Anderson, J. Ensher, M. Matthews, C. Wieman, and E. Cornell, Science **269**, 198 (1995).

[11] K. B. Davis, M.-O., Mewes, M. R. Andrews, N. J. van Druten, D. S. Durfee, D. M. Kurn, and W. Ketterle, Phys. Rev. Lett. **75**, 3969 (1995).

[12] C. C. Bradley, C. A. Sackett, J. J. Tollett, and R. G. Hulet, Phys. Rev. Lett. **75**, 1687 (1995).

[13] C. C. Bradley, C. A. Sackett, J. J. Tollett, and R. G. Hulet, Phys. Rev. Lett. **79**, 1170 (1997).

[14] D. G. Fried, T. C. Killian, L. Willmann, D. Landhuis, S. C. Moss, D. Kleppner, and T. J. Greytak, Phys. Rev. Lett. **81**, 3811 (1998).

[15] S. L. Cornish, N. R. Claussen, J. L. Roberts, E. A. Cornell, and C. E. Wieman, Phys. Rev. Lett. **85**, 1795 (2000).

[16] G. Modugno, G. Ferrari, G. Roati, R. J. Brecha, A. Simoni, and M. Inguscio, Science **294**, 1320 (2001).

[17] A. Robert, O. Sirjean, A. Browaeys, J. Poupard, S. Nowak, D. Boiron, C. I. Westbrook, and A. Aspect, Science **292**, 461 (2001).

[18] Y. Takasu, K. Maki, K. Komori, T. Takano, K. Honda, M. Kumakura, T. Yabuzaki, and Y. Takahashi, Phys. Rev. Lett. **91**, 040404 (2003).

[19] T. Weber, J. Herbig, M. Mark, H.-C. Nägerl, and R. Grimm, Science **299**, 232 (2003).

[20] A. Griesmaier, J. Werner, S. Hensler, J. Stuhler, and T. Pfau, Phys. Rev. Lett. **94**, 160401 (2005).

[21] S. Stellmer, M. K. Tey, B. Huang, R. Grimm, and F. Schreck, Phys. Rev. Lett. **103**, 200401 (2009).

[22] Y. N. M. de Escobar, P. G. Mickelson, M. Yan, B. J. DeSalvo, S. B. Nagel, and T. C. Killian, Phys. Rev. Lett. **103**, 200402 (2009).

[23] S. Stellmer, M. K. Tey, R. Grimm, and F. Schreck, Phys. Rev. A **82**, 041602 (2010).

[24] P. G. Mickelson, Y. N. Martinez de Escobar, M. Yan, B. J. DeSalvo, and T. C. Killian, Phys. Rev. A **81**, 051601 (2010).

[25] S. Kraft, F. Vogt, O. Appel, F. Riehle, and U. Sterr, Phys. Rev. Lett. **103**, 130401 (2009).

[26] M. Lu, N. Q. Burdick, S. H. Youn, and B. L. Lev, Phys. Rev. Lett. **107**, 190401 (2011).

[27] N. D. Mermin and H. Wagner, Phys. Rev. Lett. **17**, 1133 (1966).

[28] P. C. Hohenberg, Phys. Rev. **158**, 383 (1967).

[29] W. Mullin, Journal of Low Temperature Physics **106**, 615 (1997).

[30] T.-L. Ho and M. Ma, Journal of Low Temperature Physics **115**, 61 (1999).

[31] D. S. Petrov, G. V. Shlyapnikov, and J. T. M. Walraven, Phys. Rev. Lett. **85**, 3745 (2000).

[32] D. S. Petrov, G. V. Shlyapnikov, and J. T. M. Walraven, Phys. Rev. Lett. **87**, 050404 (2001).

[33] F. Dalfovo, S. Giorgini, L. P. Pitaevskii, and S. Stringari, Rev. Mod. Phys. **71**, 463 (1999).

[34] M. R. Andrews, C. G. Townsend, H.-J. Miesner, D. S. Durfee, D. M. Kurn, and W. Ketterle, Science **275**, 637 (1997).

[35] E. W. Hagley, L. Deng, M. Kozuma, M. Trippenbach, Y. B. Band, M. Edwards, M. Doery, P. S. Julienne, K. Helmerson, S. L. Rolston, et al., Phys. Rev. Lett. **83**, 3112 (1999).

[36] J. Stenger, S. Inouye, A. P. Chikkatur, D. M. Stamper-Kurn, D. E. Pritchard, and W. Ketterle, Phys. Rev. Lett. **82**, 4569 (1999).

[37] I. Bloch, T. W. Hansch, and T. Esslinger, Nature (London) **403**, 166 (2000).

[38] A. Görlitz, J. M. Vogels, A. E. Leanhardt, C. Raman, T. L. Gustavson, J. R. Abo-Shaeer, A. P. Chikkatur, S. Gupta, S. Inouye, T. Rosenband, et al., Phys. Rev. Lett. **87**, 130402 (2001).

[39] D. Rychtarik, B. Engeser, H.-C. Nägerl, and R. Grimm, Phys. Rev. Lett. **92**, 173003 (2004).

[40] S. Stock, Z. Hadzibabic, B. Battelier, M. Cheneau, and J. Dalibard, Phys. Rev. Lett. **95**, 190403 (2005).

[41] N. L. Smith, W. H. Heathcote, G. Hechenblaikner, E. Nugent, and C. J. Foot, Journal of Physics B Atomic Molecular Physics **38**, 223 (2005).

[42] Z. Hadzibabic, P. Krüger, M. Cheneau, B. Battelier, and J. Dalibard, Nature **441**, 1118 (2006).

[43] V. Schweikhard, S. Tung, and E. A. Cornell, Phys. Rev. Lett. **99**, 030401 (2007).

[44] P. Krüger, Z. Hadzibabic, and J. Dalibard, Phys. Rev. Lett. **99**, 040402 (2007).

[45] Z. Hadzibabic, P. Krüger, M. Cheneau, S. P. Rath, and J. Dalibard, New Journal of Physics **10**, 045006 (2008).

[46] P. Cladé, C. Ryu, A. Ramanathan, K. Helmerson, and W. D. Phillips, Phys. Rev. Lett. **102**, 170401 (2009).

[47] S. P. Rath, T. Yefsah, K. J. Günter, M. Cheneau, R. Desbuquois, M. Holzmann, W. Krauth, and J. Dalibard, Phys. Rev. A **82**, 013609 (2010).

[48] S. Tung, G. Lamporesi, D. Lobser, L. Xia, and E. A. Cornell, Phys. Rev. Lett. **105**, 230408 (2010).

[49] C.-L. Hung, X. Zhang, N. Gemelke, and C. Chin, Nature **470**, 236 (2011).

[50] F. Schreck, L. Khaykovich, K. L. Corwin, G. Ferrari, T. Bourdel, J. Cubizolles, and C. Salomon, Phys. Rev. Lett. **87**, 080403 (2001).

[51] S. Dettmer, D. Hellweg, P. Ryytty, J. J. Arlt, W. Ertmer, K. Sengstock, D. S. Petrov, G. V. Shlyapnikov, H. Kreutzmann, L. Santos, et al., Phys. Rev. Lett. **87**, 160406 (2001).

[52] I. Shvarchuck, C. Buggle, D. S. Petrov, K. Dieckmann, M. Zielonkowski, M. Kemmann, T. G. Tiecke, W. von Klitzing, G. V. Shlyapnikov, and J. T. M. Walraven, Phys. Rev. Lett. **89**, 270404 (2002).

[53] D. Hellweg, L. Cacciapuoti, M. Kottke, T. Schulte, K. Sengstock, W. Ertmer, and J. J. Arlt, Phys. Rev. Lett. **91**, 010406 (2003).

[54] S. Richard, F. Gerbier, J. H. Thywissen, M. Hugbart, P. Bouyer, and A. Aspect, Phys. Rev. Lett. **91**, 010405 (2003).

[55] H. Moritz, T. Stöferle, M. Köhl, and T. Esslinger, Phys. Rev. Lett. **91**, 250402 (2003).

[56] B. Paredes, A. Widera, V. Murg, O. Mandel, S. Fölling, I. Cirac, G. V. Shlyapnikov, T. W. Hänsch, and I. Bloch, Nature **429**, 277 (2004).

[57] T. Kinoshita, T. Wenger, and D. S. Weiss, Science **305**, 1125 (2004).

[58] L. Cacciapuoti, D. Hellweg, M. Kottke, T. Schulte, W. Ertmer, J. J. Arlt, K. Sengstock, L. Santos, and M. Lewenstein, Phys. Rev. A **68**, 053612 (2003).

[59] J.-B. Trebbia, J. Esteve, C. I. Westbrook, and I. Bouchoule, Phys. Rev. Lett. **97**, 250403 (2006).

[60] A. H. van Amerongen, J. J. P. van Es, P. Wicke, K. V. Kheruntsyan, and N. J. van Druten, Phys. Rev. Lett. **100**, 090402 (2008).

[61] J. Armijo, T. Jacqmin, K. V. Kheruntsyan, and I. Bouchoule, Phys. Rev. Lett. **105**, 230402 (2010).

[62] J. Armijo, T. Jacqmin, K. Kheruntsyan, and I. Bouchoule, Phys. Rev. A **83**, 021605 (2011).

[63] J. Estève, J.-B. Trebbia, T. Schumm, A. Aspect, C. I. Westbrook, and I. Bouchoule, Phys. Rev. Lett. **96**, 130403 (2006).

[64] F. Gerbier, J. H. Thywissen, S. Richard, M. Hugbart, P. Bouyer, and A. Aspect, Phys. Rev. A **67**, 051602 (2003).

[65] S. Manz, R. Bücker, T. Betz, C. Koller, S. Hofferberth, I. E. Mazets, A. Imambekov, E. Demler, A. Perrin, J. Schmiedmayer, et al., Phys. Rev. A **81**, 031610 (2010).

[66] T. L. Gustavson, P. Bouyer, and M. A. Kasevich, Phys. Rev. Lett. **78**, 2046 (1997).

[67] E. A. Hinds, C. J. Vale, and M. G. Boshier, Phys. Rev. Lett. **86**, 1462 (2001).

[68] T. Schumm, S. Hofferberth, L. M. Andersson, S. Wildermuth, S. Groth, I. Bar-Joseph, J. Schmiedmayer, and P. Krüger, Nature Physics **1**, 57 (2005).

[69] S. Hofferberth, I. Lesanovsky, B. Fischer, J. Verdu, and J. Schmiedmayer, Nature Physics **2**, 710 (2006).

[70] J. B. Fixler, G. T. Foster, J. M. McGuirk, and M. A. Kasevich, Science **315**, 74 (2007).

[71] G.-B. Jo, Y. Shin, S. Will, T. A. Pasquini, M. Saba, W. Ketterle, D. E. Pritchard, M. Vengalattore, and M. Prentiss, Phys. Rev. Lett. **98**, 030407 (2007).

[72] S. Hofferberth, I. Lesanovsky, B. Fischer, T. Schumm, and J. Schmiedmayer, Nature **449**, 324 (2007).

[73] C. Gross, T. Zibold, E. Nicklas, J. Estève, and M. K. Oberthaler, Nature **464**, 1165 (2010).

[74] F. Baumgärtner, R. J. Sewell, S. Eriksson, I. Llorente-Garcia, J. Dingjan, J. P. Cotter, and E. A. Hinds, Phys. Rev. Lett. **105**, 243003 (2010).

[75] E. A. Hinds and I. G. Hughes, Journal of Physics D Applied Physics **32**, 119 (1999).

[76] H. Ott, J. Fortagh, G. Schlotterbeck, A. Grossmann, and C. Zimmermann, Phys. Rev. Lett. **87**, 230401 (2001).

[77] W. Hänsel, J. Reichel, P. Hommelhoff, and T. W. Hänsch, Phys. Rev. A **64**, 063607 (2001).

[78] R. Folman, P. Krüger, J. Schmiedmayer, J. Denschlag, and C. Henkel, Advances in Atomic and Molecular Physics **48**, 263 (2002), `0805.2613`.

[79] J. Fortágh and C. Zimmermann, Rev. Mod. Phys. **79**, 235 (2007).

[80] J. Reichel and V. E. Vuletic, *Atom Chips* (WILEY-VCH Verlag GmbH & Co. KGaA, Weinheim, 2011).

[81] M. Girardeau, Journal of Mathematical Physics **1**, 516 (1960).

[82] J. N. Fuchs, X. Leyronas, and R. Combescot, Phys. Rev. A **68**, 043610 (2003).

[83] E. H. Lieb and W. Liniger, Phys. Rev. **130**, 1605 (1963).

[84] M. Olshanii, Phys. Rev. Lett. **81**, 938 (1998).

[85] D. S. Petrov, D. M. Gangardt, and G. V. Shlyapnikov, J. Phys. IV France **116**, 5 (2004).

[86] U. Al Khawaja, N. P. Proukakis, J. O. Andersen, M. W. J. Romans, and H. T. C. Stoof, Phys. Rev. A **68**, 043603 (2003).

[87] V. N. Popov, *Functional Integrals in Quantum Field Theory and Statistical Physics* (Reidel, Dordrecht, 1983).

[88] N. P. Proukakis, Phys. Rev. A **73**, 023605 (2006).

[89] W. Ketterle and N. J. van Druten, Phys. Rev. A **54**, 656 (1996).

[90] U. Al Khawaja, J. O. Andersen, N. P. Proukakis, and H. T. C. Stoof, Phys. Rev. A **66**, 013615 (2002).

[91] P. Krüger, S. Hofferberth, I. E. Mazets, I. Lesanovsky, and J. Schmiedmayer, Phys. Rev. Lett. **105**, 265302 (2010).

[92] T. Betz, S. Manz, R. Bücker, T. Berrada, C. Koller, G. Kazakov, I. E. Mazets, H.-P. Stimming, A. Perrin, T. Schumm, et al., Phys. Rev. Lett. **106**, 020407 (2011).

[93] D. Hellweg, S. Dettmer, P. Ryytty, J. Arlt, W. Ertmer, K. Sengstock, D. Petrov, G. Shlyapnikov, H. Kreutzmann, L. Santos, et al., Applied Physics B: Lasers and Optics **73**, 781 (2001).

[94] P. Bouyer, J. H. Thywissen, F. Gerbier, M. Hugbart, S. Richard, and A. Retter, J. Aspect, J. Phys. IV France **116**, 219 (2004).

[95] M. Hugbart, J. A. Retter, F. Gerbier, A. F. Varón, S. Richard, J. H. Thywissen, D. Clément, P. Bouyer, and A. Aspect, European Physical Journal D **35**, 155 (2005).

[96] V. N. Popov, Theoretical and Mathematical Physics **11**, 565 (1972).

[97] J. O. Andersen, U. Al Khawaja, and H. T. C. Stoof, Phys. Rev. Lett. **88**, 070407 (2002).

[98] D. L. Luxat and A. Griffin, Phys. Rev. A **67**, 043603 (2003).

[99] C. Mora and Y. Castin, Phys. Rev. A **67**, 053615 (2003).

[100] N. M. Bogoliubov, C. Malyshev, R. K. Bullough, and J. Timonen, Phys. Rev. A **69**, 023619 (2004).

[101] F. Gerbier, Europhys. Lett. **66**, 771 (2004).

[102] D. Kadio, M. Gajda, and K. Rzążewski, Phys. Rev. A **72**, 013607 (2005).

[103] M. Greiner, I. Bloch, O. Mandel, T. W. Hänsch, and T. Esslinger, Phys. Rev. Lett. **87**, 160405 (2001).

[104] F. Zambelli, L. Pitaevskii, D. M. Stamper-Kurn, and S. Stringari, Phys. Rev. A **61**, 063608 (2000).

[105] Y. Shin, M. Saba, T. A. Pasquini, W. Ketterle, D. E. Pritchard, and A. E. Leanhardt, Phys. Rev. Lett. **92**, 050405 (2004).

[106] Y.-J. Wang, D. Z. Anderson, V. M. Bright, E. A. Cornell, Q. Diot, T. Kishimoto, M. Prentiss, R. A. Saravanan, S. R. Segal, and S. Wu, Phys. Rev. Lett. **94**, 090405 (2005).

[107] I. Bloch, T. W. Hänsch, and T. Esslinger, Phys. Rev. Lett. **82**, 3008 (1999).

[108] F. Gerbier, P. Bouyer, and A. Aspect, Phys. Rev. Lett. **86**, 4729 (2001).

[109] T. Lahaye, J. M. Vogels, K. J. Günter, Z. Wang, J. Dalibard, and D. Guéry-Odelin, Phys. Rev. Lett. **93**, 093003 (2004).

[110] W. Guerin, J.-F. Riou, J. P. Gaebler, V. Josse, P. Bouyer, and A. Aspect, Phys. Rev. Lett. **97**, 200402 (2006).

[111] E. Zaremba, T. Nikuni, and A. Griffin, J. Low Temp. Phys. **116**, 277 (1999).

[112] C. W. Gardiner, Phys. Rev. A **56**, 1414 (1997).

[113] Y. Castin and R. Dum, Phys. Rev. A **57**, 3008 (1998).

[114] S. A. Gardiner and S. A. Morgan, Phys. Rev. A **75**, 043621 (2007).

[115] P. B. Blakie, A. S. Bradley, M. J. Davis, R. J. Ballagh, and C. W. Gardiner, Adv. Phys. **57**, 363 (2008).

[116] H. T. C. Stoof, J. Low Temp. Phys. **114**, 11 (1999).

[117] H. T. C. Stoof and M. J. Bijlsma, J. Low Temp. Phys. **124**, 431 (2001).

[118] S. P. Cockburn, D. Gallucci, and N. P. Proukakis, Phys. Rev. A **84**, 023613 (2011).

[119] D. Gallucci, S. P. Cockburn, and N. P. Proukakis, Phys. Rev. A **86**, 013627 (2012).

[120] N. P. Proukakis and B. Jackson, J. Phys. B **41**, 203002 (2008).

[121] D. J. Griffiths, *Introduction to quantum mechanics* (Prentice Hall, 1994).

[122] A. L. Fetter and J. D. Walecka, *Quantum theory of many-particle systems* (New York: McGraw Hill, 1971).

[123] A. Griffin, T. Nikuni, and E. Zaremba, *Bose-Condensed Gases at Finite Temperatures* (Cambridge University Press, Cambridge, 2009).

[124] A. L. Fetter, Annals of Physics **70**, 67 (1972).

[125] N. N. Bogoliubov, J. Phys. USSR **11**, 23 (1947).

[126] L. P. Pitaevskii and S. Stringari, *Bose-Einstein Condensation*, vol. 116 of *International Series of Monographs on Physics* (Oxford University Press, Oxford New York, 2003).

[127] C. J. Pethick and H. Smith, *Bose-Einstein Condensation in Dilute Gases* (Cambridge University Press, Cambridge, 2002).

[128] U. Al Khawaja, J. O. Andersen, N. P. Proukakis, and H. T. C. Stoof, Phys. Rev. A **66**, 059902 (2002).

[129] T. R. Kirkpatrick and J. R. Dorfman, Phys. Rev. A **28**, 2576 (1983).

[130] T. R. Kirkpatrick and J. R. Dorfman, Journal of Low Temperature Physics **58**, 301 (1985).

[131] T. R. Kirkpatrick and J. R. Dorfman, Journal of Low Temperature Physics **58**, 399 (1985).

[132] U. Eckern, J. Low Temp. Phys. **54**, 333 (1984).

[133] E. M. Lifshitz and L. P. Pitaevskii, *Physical Kinetics* (Butterworth-Heinemann Ltd., 1981).

[134] M. Girardeau and R. Arnowitt, Phys. Rev. **113**, 755 (1959).

[135] O. Penrose and L. Onsager, Phys. Rev. **104**, 576 (1956).

[136] M. Brewczyk, M. Gajda, and K. Rzazewski, J. Phys. B **40**, R1 (2007).

[137] M. J. Davis, T. M. Wright, P. B. Blakie, A. S. Bradley, R. J. Ballagh, and C. W. Gardiner, arXiv:1206.5470v2 (2012).

[138] C. W. Gardiner, J. R. Anglin, and T. I. A. Fudge, J. Phys. B **35**, 1555 (2002).

[139] C. W. Gardiner and M. J. Davis, J. Phys. B **36**, 4731 (2003).

[140] C. W. Gardiner and P. Zoller, Phys. Rev. A **55**, 2902 (1997).

[141] C. W. Gardiner and P. Zoller, Phys. Rev. A **58**, 536 (1998).

[142] C. W. Gardiner and P. Zoller, Phys. Rev. A **61**, 033601 (2000).

[143] M. J. Davis, S. A. Morgan, and K. Burnett, Phys. Rev. Lett. **87**, 160402 (2001).

[144] M. J. Davis, S. A. Morgan, and K. Burnett, Phys. Rev. A **66**, 053618 (2002).

[145] C. W. Gardinder and P. Zoller, *Quantum noise* (Springer, Berlin, 1999).

[146] M. J. Steel, M. K. Olsen, L. I. Plimak, P. D. Drummond, S. M. Tan, M. J. Collett, D. F. Walls, and R. Graham, Phys. Rev. A **58**, 4824 (1998).

[147] S. J. Rooney, P. Blakie, and A. S. Bradley (2012), `arXiv:1210.0952`.

[148] A. S. Bradley, C. W. Gardiner, and M. J. Davis, Phys. Rev. A **77**, 033616 (2008).

[149] M. C. Garrett, T. M. Wright, and M. J. Davis, arXiv:1209.3297v1 (2012).

[150] C. N. Weiler, T. W. Neely, D. R. Scherer, A. S. Bradley, M. J. Davis, and B. P. Anderson, Nature **455**, 948 (2008).

[151] H. T. C. Stoof, in *Dynamics: Models and Kinetic Methods for Non-equilibrium Many Body Systems*, edited by J. Karkheck (Kluwer, Dordrecht, 2000), vol. 317 of *NATO ASI Proceedings*, pp. 491–502, `arXiv:cond-mat/9812424`.

[152] R. A. Duine and H. T. C. Stoof, Phys. Rev. A **65**, 013603 (2001).

[153] D. M. Stamper-Kurn, H.-J. Miesner, A. P. Chikkatur, S. Inouye, J. Stenger, and W. Ketterle, Phys. Rev. Lett. **81**, 2194 (1998).

[154] R. A. Duine, B. W. A. Leurs, and H. T. C. Stoof, Phys. Rev. A **69**, 053623 (2004).

[155] N. P. Proukakis, Las. Phys. **13**, 527 (2003).

[156] N. P. Proukakis, Phys. Rev. A **74**, 053617 (2006).

[157] N. P. Proukakis, J. Schmiedmayer, and H. T. C. Stoof, Phys. Rev. A **73**, 053603 (2006).

[158] W. H. Zurek, Phys. Rev. Lett. **102**, 105702 (2009).

[159] B. Damski and W. H. Zurek, Phys. Rev. Lett. **104**, 160404 (2010).

[160] S. P. Cockburn, H. E. Nistazakis, T. P. Horikis, P. G. Kevrekidis, N. P. Proukakis, and D. J. Frantzeskakis, Phys. Rev. Lett. **104**, 174101 (2010).

[161] H. T. C. Stoof, Phys. Rev. Lett. **78**, 768 (1997).

[162] L. V. Keldysh, Zh. Eksp. Teor. Fiz. **47**, 1515 (1964).

[163] L. V. Keldysh, Sov. Phys.-JETP **20**, 1018 (1965).

[164] S. P. Cockburn and N. P. Proukakis, Phys. Rev. A **86**, 033610 (2012).

[165] S. P. Cockburn, *Bose gases in and out of equilibrium within the Stochastic Gross-Pitaevskii equation*, Ph.D. Thesis (Newcastle University, 2005).

[166] A. A. Penckwitt, R. J. Ballagh, and C. W. Gardiner, Phys. Rev. Lett. **89**, 260402 (2002).

[167] S. P. Cockburn, A. Negretti, N. P. Proukakis, and C. Henkel, Phys. Rev. A **83**, 043619 (2011).

[168] M. Bijlsma and H. T. C. Stoof, Phys. Rev. A **55**, 498 (1997).

[169] A. M. Mateo and V. Delgado, Phys. Rev. A **77**, 013617 (2008).

[170] A. M. Mateo and V. Delgado, Annals of Physics **324**, 709 (2009).

[171] L. Salasnich, A. Parola, and L. Reatto, Phys. Rev. A **65**, 043614 (2002).

[172] A. Muñoz Mateo and V. Delgado, Phys. Rev. A **75**, 063610 (2007).

[173] D. J. Frantzeskakis, Journal of Physics A Mathematical General **43**, 213001 (2010).

[174] M. Naraschewski and D. M. Stamper-Kurn, Phys. Rev. A **58**, 2423 (1998).

[175] M. J. Davis, P. B. Blakie, A. H. van Amerongen, N. J. van Druten, and K. V. Kheruntsyan, Phys. Rev. A **85**, 031604 (2012).

[176] S. Giorgini, L. P. Pitaevskii, and S. Stringari, Phys. Rev. A **54**, R4633 (1996).

[177] E. Andersson, T. Calarco, R. Folman, M. Andersson, B. Hessmo, and J. Schmiedmayer, Phys. Rev. Lett. **88**, 100401 (2002).

[178] G.-B. Jo, J.-H. Choi, C. A. Christensen, T. A. Pasquini, Y.-R. Lee, W. Ketterle, and D. E. Pritchard, Phys. Rev. Lett. **98**, 180401 (2007).

[179] J. Reichel and V. Vuletic, eds., *Atom Chips* (Wiley-VCH, Weinheim, Germany, 2011).

[180] R. J. Glauber, Phys. Rev. **130**, 2529 (1963).

[181] H. T. C. Stoof, D. B. M. Dickerscheid, and K. Gubbels, *Ultracold Quantum Fields*, Theoretical and Mathematical Physics (Springer, 2009).

[182] C. Cohen-Tannoudji and C. Robilliard, Comptes Rendus de l'Academie des Sciences Series IV Physics **2**, 445 (2001).

[183] L. Mandel and E. Wolf, *Optical coherence and quantum optics* (Cambridge University Press, Cambridge, 1995).

[184] R. Dodd, C. Clark, M. Edwards, and K. Burnett, Opt. Express **1**, 284 (1997).

[185] N. Prokof'ev, O. Ruebenacker, and B. Svistunov, Phys. Rev. Lett. **87**, 270402 (2001).

[186] S. P. Cockburn and N. P. Proukakis, Las. Phys. **19**, 558 (2009).

[187] R. N. Bisset, M. J. Davis, T. P. Simula, and P. B. Blakie, Phys. Rev. A **79**, 033626 (2009).

[188] P. B. Blakie and M. J. Davis, Phys. Rev. A **72**, 063608 (2005).

[189] M. Naraschewski and R. J. Glauber, Phys. Rev. A **59**, 4595 (1999).

[190] N. Prokof'ev and B. Svistunov, Phys. Rev. A **66**, 043608 (2002).

[191] R. N. Bisset and P. B. Blakie, Phys. Rev. A **80**, 035602 (2009).

[192] C. N. Yang and C. P. Yang, Journal of Mathematical Physics **10**, 1115 (1969).

[193] M. J. Davis, P. B. Blakie, A. H. van Amerongen, N. J. van Druten, and K. V. Kheruntsyan, Phys. Rev. A **85**, 031604 (2012).

[194] L. D. Landau and E. M. Lifshitz, *Statistical Physics, Part 1.*, vol. Vol. 5 (3rd ed.) (Butterworth-Heinemann, 1980).

[195] A. L. Zubarev and Y. E. Kim, Phys. Rev. A **65**, 035601 (2002).

[196] V. V. Goldman, I. F. Silvera, and A. J. Leggett, Phys. Rev. B **24**, 2870 (1981).

[197] S. Giorgini, L. P. Pitaevskii, and S. Stringari, J. Low Temp. Phys. **109**, 309 (1997).

[198] F. Gerbier, J. H. Thywissen, S. Richard, M. Hugbart, P. Bouyer, and A. Aspect, Phys. Rev. A **70**, 013607 (2004).

[199] Jocelyn Retter (Private Communication).

[200] M. A. Cazalilla, Journal of Physics B Atomic, Molecular and Optical Physics **37**, 48 (2004).

[201] T. M. Wright, N. P. Proukakis, and M. J. Davis, Phys. Rev. A **84**, 023608 (2011).

[202] M. Hugbart-Fouché, *Étude des propriétés de cohérence d'un condensat de Bose-Einstein à l'équilibre et hors équilibre*, Ph.D. Thesis (Université Paris XI, 2010).

[203] M. Gring, M. Kuhnert, T. Langen, T. Kitagawa, B. Rauer, M. Schreitl, I. Mazets, D. A. Smith, E. Demler, and J. Schmiedmayer, Science **337**, 1318 (2012).

[204] Fabrice Gerbier (Private Communication).